UNIVERSIDAD
DE GRANADA

FACULTAD DE CIENCIAS
Departamento de Química Inorgánica

PROGRAMA DE DOCTORADO EN QUÍMICA

TESIS DOCTORAL

SÍNTESIS, CARACTERÍSTICAS SUPERFICIALES Y APLICACIONES ELECTROQUÍMICAS DE ESFERAS Y MONOLITOS DE CARBONO Y CARBONES ACTIVADOS. EFECTO DE LOS PRECURSORES DE CARBONO Y DEL CONTENIDO EN N

MARÍA HELENA GARCIA ROSERO

Granada, Mayo 2017

Editor: Universidad de Granada. Tesis Doctorales
Autora: María Helena García Rosero
ISBN: 978-84-9163-339-6
URI: http://hdl.handle.net/10481/47569

Síntesis, características superficiales y aplicaciones electroquímicas de esferas y monolitos de carbono y carbones activados. Efecto de los precursores de carbono y del contenido en N

MARÍA HELENA GARCIA ROSERO

Memoria presentada para optar al grado de Doctor
por la Universidad de Granada

Fdo.: María Helena Garcia Rosero
Licenciada en Química

Los Directores de la Tesis

Prof. Dr. Carlos Moreno Castilla	**Prof. Dr. Francisco Carrasco Marín**
Catedrático del Departamento de	Catedrático del Departamento de
Química Inorgánica	Química Inorgánica
Universidad de Granada	Universidad de Granada

Tesis presentada para aspirar al grado de Doctor en Química por

MARÍA HELENA GARCIA ROSERO

Realizada bajo la dirección de los Catedráticos de Química Inorgánica Prof. Dr. Carlos Moreno Castilla y Prof. Dr. Francisco Carrasco Marín, en la Facultad de Ciencias de la Universidad de Granada y juzgada por el siguiente Tribunal:

PRESIDENTE:

Profa. Dra. María Victoria López Ramón

VOCALES:

Prof. Dr. Francisco José Maldonado Hódar
Prof. Dr. Miguel Ángel Álvarez Merino
Prof. Dr. Sergio Morales Torres

SECRETARIO:

Profa. Dra. María Isidora Bautista Toledo

Carlos Moreno Castilla y Francisco Carrasco Marín como directores de la presente Tesis Doctoral y la doctoranda María Helena García Rosero

GARANTIZAN QUE

el trabajo ha sido realizado por el doctorando respetando los derechos de otros autores a ser citados cuando se han utilizado sus resultados o publicaciones.

Y para que conste a los efectos oportunos, en el cumplimiento de la legislación vigente, firmamos el presente certificado en Granada a 24 de mayo del 2017.

Fdo.: Carlos Moreno Castilla Catedrático de Química Inorgánica de la Universidad de Granada	Fdo.: Francisco Carrasco Marín Catedrático de Química Inorgánica de la Universidad de Granada

Fdo.: Doctoranda María Helena García Rosero
Licenciada en Química

AGRADECIMIENTOS

Deseo expresar mis agradecimientos a todas aquellas personas que de una u otra forma han contribuido a la realización de este trabajo, en especial a:
Dios, quien ha sido mi sustento, apoyo y guía durante toda la vida y quien me dio la fuerza para llegar a este momento.

Los Doctores Carlos Moreno Castilla y Francisco Carrasco Marín, directores del presente trabajo por su acompañamiento y guía durante cada etapa de este proceso.

Los profesores miembros del Grupo de Investigación en Materiales de Carbón de la Universidad de Granada y mis compañeros quienes me ayudaron a hacer más grato mi estancia en Granada.

El personal del Centro de Instrumentación Científica de la Universidad de Granada, por su colaboración en la realización de los ensayos de caracterización del presente trabajo, en especial a Alicia Sánchez Segura, Maria del Mar Abad Ortega, Isabel Sánchez Segura, Javier Cifuentes Melchor y José Ruíz Ortiz.

Los miembros del Departamento de Inorgánica de la Universidad de Granada, en especial a Antonio de la Torre Carrasco y María del Carmen Ferrer Ruíz.

La Doctora Ana Paula Carvalho del grupo de investigación en Adsorción y Materiales Adsorbentes de la Universidad de Lisboa, quien me recibió para realizar la estancia de investigación que me permite optar con este trabajo al Doctorado Internacional.

Rossana, Valentine y Johanna, por su amistad y todos los momentos vividos durante mi paso por Lisboa.

Mis padres, Stella y Guillermo, por su apoyo y motivación constante, al igual que a mis hermanos, Diana y Fernando, mi abuelo León y demás familia, quienes me han animado constantemente a seguir adelante.

A mi esposo por su comprensión, colaboración y amor incondicional. Gracias por recordarme que juntos todo es posible.

Y por último deseo agradecer al Departamento Administrativo de Ciencia, Tecnología e Información de la República de Colombia (COLCIENCIAS) por el apoyo económico brindado para la realización de mis estudios a través de la “Convocatoria nacional para estudios de Doctorado en el exterior, año 2011”.

Este Trabajo de Investigación ha sido realizado gracias a: COLCIENCIAS por la concesión de una beca de la Convocatoria nacional para estudios de Doctorado en el exterior, año 2011*; La doctoranda y los directores también agradecen la financiación recibida por parte de distintas entidades: Junta de Andalucía, grupo de investigación RNM-172 y el proyecto “Transformado de desechos del olivar en materiales avanzados para la conversión electro-catalítica de* CO_2 *en hidrocarburos” P12-RNM-2892; y el proyecto “Reducción de emisiones de* CO_2 *y tecnologías de almacenamiento de energías renovables empleando materiales avanzados de carbón” Ministerio de Economía y Competitividad, Fondos FEDER, CTQ2013-44789-R*

COLCIENCIAS
Ciencia, Tecnología e Innovación
GOBIERNO DE ESPAÑA
MINISTERIO DE ECONOMÍA Y COMPETITIVIDAD
JUNTA DE ANDALUCIA

A mi familia, en especial a mi esposo.

CONTENIDO

PREFACIO

En la presente Tesis Doctoral se han preparado esferas y monolitos (aerogeles) de carbono y carbones activados. Las esferas de carbono se obtuvieron mediante la polimerización de resorcinol, pirocatecol y 3-hidroxipiridina con formaldehido mediante una reacción de polimerización por emulsión. Las esferas de carbono también se prepararon mediante el uso de moldes sólidos de sílice que se recubrieron con residuos líquidos procedentes de la industria del aceite de oliva como precursores de C. Los monolitos de C (aerogeles) se obtuvieron por carbonización de geles orgánicos preparados mediante reacciones de policondensación de resorcinol y formaldehido catalizada por carbonatos alcalinos (Na y K). Los carbones activados se sintetizaron a partir de huesos de *Melia Azedarach* y *Schinus Molle* mediante activación con KOH de los huesos originales, o previamente carbonizados o tratados hidrotermalmente a diferentes temperaturas. Los materiales sintetizados se caracterizaron para conocer su morfología, química superficial y textura, empleándose como electrodos de condensadores electroquímicos o supercondensadores para el almacenamiento de energía eléctrica.

Esta Tesis Doctoral se enmarca dentro de los proyectos de investigación que se han desarrollado en el Grupo de Investigación en Materiales de Carbón de la Universidad de Granada. “Transformado de desechos del olivar en materiales avanzados para la conversión electro-catalítica de CO_2 en hidrocarburos” proyecto de Excelencia de la Junta de Andalucía, P12.RNM2892 y “Reducción de emisiones de CO_2 y tecnologías de almacenamiento de energías renovables empleando materiales avanzados de carbón” financiado por el Ministerio de Economía y Competitividad, Fondos FEDER, CTQ2013-44789.R.

El trabajo desarrollado durante la realización de esta Tesis Doctoral se ha organizado en los siguientes Capítulos:

Capitulo I. Introducción y Objetivos.

Capítulo II. Materiales y métodos experimentales

Capítulo III. Síntesis y caracterización de esferas sólidas de polímero y de carbono obtenidas mediante reacciones de polimerización por emulsión de diferentes compuestos fenólicos con formaldehído.

Las esferas poliméricas se prepararon mediante una reacción de polimerización por emulsión de resorcinol, pirocatecol o 3-hidroxipiridina con formaldehído en medio básico. Las esferas de carbono se obtuvieron por carbonización de las esferas poliméricas a 900 ºC. Algunas muestras seleccionadas se activaron con KOH o mediante ciclos de adsorción-desorción de oxígeno. El resorcinol y pirocatecol difieren en su reactividad durante la reacción de policondensación con formaldehído. El uso de 3-hidroxipiridina permitió la introducción de funcionalidades de N en las esferas de carbono obtenidas. Se han estudiado los efectos de los monómeros empleados en la síntesis de las esferas poliméricas, sustitución del resorcinol por el pirocatecol en la reacción de polimerización, la introducción de grupos funcionales de N y el uso de diferentes métodos de activación de las esferas de carbono sobre su diámetro, su física y química superficial y su comportamiento como electrodos de condensadores electroquímicos de doble capa. El tamaño, la superficie, el volumen de microporos, el volumen total de poro y la anchura de microporos de las esferas de C oscilaron entre 159 y 856 nm, 7 y 1156 m^2 g^{-1}, 0,06 y 0,46 cm^3 g^{-1}, 0,15 y 0,58 cm^3 g^{-1}, y 0,50 y 1,23 nm, respectivamente. La muestra físicamente activada mostró la mayor capacidad a 1 A g^{-1}, 200 F g-1 o 17,3 μF cm^{-2}. La capacidad fue mayor en muestras dopadas con N que en la muestra no dopada.

Capítulo IV. Esferas de carbono huecas y sólidas obtenidas a partir del residuo del almacenamiento de aceitunas empleando moldes sólidos.

Se prepararon esferas sólidas y huecas de carbono a partir de residuos líquidos procedentes del almacenamiento de aceituna utilizando esferas de sílice con núcleo sólido y corteza mesoporosa y de sílice micro-mesoporosa como moldes. Se obtuvieron dos tipos de esferas huecas con un diámetro externo de 385 y 678 nm y un espesor de pared de 23 y 100 nm, respectivamente. Las esferas de C sólidas tenían un diámetro de 9 μm. El área superficial, el volumen de microporos, la anchura de los microporos, el volumen total de poros y la anchura media de los CSs oscilaron entre 646-806 m^2 g^{-1}, 0,21-0,27 cm^3 g^{-1}, 1,3-1,6 nm, 0,47-1,81 cm^3 g^{-1}, y de 3,1 a 3,7 nm, respectivamente. La capacidad electroquímica en H_2SO_4 1 M varió entre 2,5 y 17,5 μF cm^{-2}.

Capítulo V. Comportamiento de aerogeles de carbono (monolitos) con diferente textura porosa como electrodos de supercondensadores usando electrolitos ácidos y básicos.

El objetivo de este trabajo es investigar el comportamiento de diversos aerogeles de carbono (monolitos) como electrodos de supercondensadores en electrolitos ácidos y básicos a altas densidades de corriente y correlacionar su eficiencia con su textura porosa. Para ello se seleccionaron tres aerogeles de carbono microporosos con diferentes texturas de poro. Su eficiencia en el almacenamiento de energía eléctrica se estudió en una celda de dos electrodos mediante espectroscopía de impedancia electroquímica y carga-descarga galvanostática. Los resultados obtenidos mostraron que la capacidad gravimétrica aumentó al aumentar la anchura media de los microporos y que la resistencia eléctrica fue mayor en los electrolitos básicos que en los electrolitos ácidos. El aerogel de carbono con mayor volumen de macroporos presentó mayor resistencia eléctrica en ambos electrolitos. Por el contrario, la muestra con mayor volumen de microporos, con anchura media de 1,15 nm y mayor volumen de mesoporos, con tamaño medio de 5,8-8,8 nm, presentó la mayor capacidad volumétrica a una densidad de corriente de 1 A g^{-1} en H_2SO_4 (109 F cm^{-3}) y en KOH (120 F cm^{-3}). Además presentó una retención de capacidad de aproximadamente 75% a 14 A g^{-1}en H_2SO_4 y a 20 A g^{-1} en KOH siendo estas capacidades volumétricas mayores que las requeridas para la utilización en sistemas de pequeño volumen. Esta muestra presentó el mejor comportamiento en electrolitos ácidos a mayores densidades de corriente, con una densidad de energía de 3 Wh kg^{-1} a una densidad de potencia de 10 kW kg^{-1}.

Capítulo VI. Carbones activados preparados a partir de huesos de *Melia Azedarach* para su uso como electrodos de supercondensadores

Los carbones activados obtenidos a partir de biomasa son materiales muy prometedores para fabricar electrodos para supercondensadores debido a su abundancia, amplia distribución geográfica y a su bajo coste de producción. En este capítulo se ha estudiado el uso potencial de huesos de *Melia Azedarach* (MA) como materia prima para preparar carbones activados. El contenido de cenizas de los huesos de MA es considerablemente más bajo (0.7% de cenizas) que en otros residuos lignocelulósicos. Se prepararon tres series de carbones activados mediante activación química con KOH de huesos de MA (serie MA), huesos MA carbonizados (serie CMA) y huesos MA tratados hidrotermalmente (serie HMA). Se determinó la morfología, la composición, el área superficial, la porosidad y la química superficial de los carbones activados. La caracterización electroquímica se llevó a cabo empleando celdas de tres y dos electrodos, 3EC y 2EC, respectivamente, utilizando H_2SO_4 1M como electrolito. Se obtuvieron carbones activados con áreas superficiales de hasta 2000 m^2 g^{-1} y con capacidades determinadas por carga-descarga galvanostática en 2EC entre 232 y 240 F g^{-1} a 1 A g^{-1}. La mayor densidad de energía obtenida fue de 27,4 Wh kg^{-1} a una densidad de potencia de 110 W kg^{-1}. La espectroscopia de impedancia electroquímica (EIS) en 2EC puso de manifiesto un aumento en la resistencia en serie equivalente (ESR) y resistencia a la transferencia de carga (RCT) al aumentar el contenido en cenizas. La estabilidad de los electrodos ante los ciclos de carga descarga estudiada mediante pruebas a voltaje constante mostraron que los carbones activados presentan un excelente comportamiento.

Capítulo VII. Características superficiales de los carbones activados obtenidos por activación directa con KOH de hueso de *Schinus Molle* y de sus derivados hidrotermales.

Los carbones activados en este trabajo se prepararon mediante la activación con KOH de huesos de *Schinus Molle* (SM), serie SM, y de huesos previamente tratados hidrotermalmente, serie HSM. El tratamiento hidrotermal se llevó a cabo mediante carbonización hidrotermal (HTC) de los huesos entre 100 y 200 ºC. Se estudió la química superficial, porosidad, área superficial y capacidad de almacenamiento de energía eléctrica de los carbones activados en celdas de dos electrodos. El objetivo fue conocer las variaciones en las características superficiales de los carbones activados introducidas por los dos métodos de preparación y por la relación másica KOH/precursor. Los carbones activados de la serie HSM tenían menores cenizas y mayores contenidos de N que los de la SM. Todos los carbones activados, excepto los más activados de la serie HSM, mostraron microporos estrechos o constricciones de microporos en sus entradas. El área superficial más alta y el volumen de mesoporos obtenidos fueron *ca*. 1500 $m^2 g^{-1}$, y 0,29 $cm^3 g^{-1}$, respectivamente. Los resultados de la caracterización físico-química de los carbones activados indicaron que los huesos de SM eran más reactivos a la activación con KOH después de su HTC. La mayor capacidad gravimétrica a 0,5 A g^{-1} varió entre 227-235 F g^{-1}, similar a otros carbones activados obtenidos a partir de diferentes materiales lignocelulósicos obteniéndose con carbones activados de la serie HSM.

Capítulo VIII. Conclusiones generales

CAPÍTULO I

INTRODUCCIÓN Y OBJETIVOS

1. INTRODUCCIÓN

Actualmente los sistemas de mayor interés para el almacenamiento de energía eléctrica son las baterías recargables y los supercondensadores (SCs). Estos sistemas se utilizan principalmente en aplicaciones portátiles móviles como ordenadores, tabletas y teléfonos móviles, en automoción y en el almacenamiento y suavizado de energías renovables intermitentes.

En la Figura 1 se presenta el diagrama de Ragone [1], en el cual se compara la energía específica con la potencia específica de diversos sistemas de almacenamiento de energía. En esta figura se observa como los supercondensadores cubren el espacio de necesidades energéticas existente entre los condensadores convencionales (electrolíticos o película metálica) y las baterías. Los condensadores electroquímicos funcionan mediante procesos no farádicos, por lo que idealmente el material del electrodo no presenta mayores cambios durante el proceso de almacenamiento de energía el cual es mucho más rápido que el realizado por las baterías, razón por la cual a pesar de poseer generalmente densidades de energía más bajas que las de las baterías estos presentan mayores densidades de potencia. Los supercondensadores pueden utilizarse en sistemas que requieran energía durante tiempos comprendidos entre 10^{-2} s $\leq t \leq 10^{2}$ s.

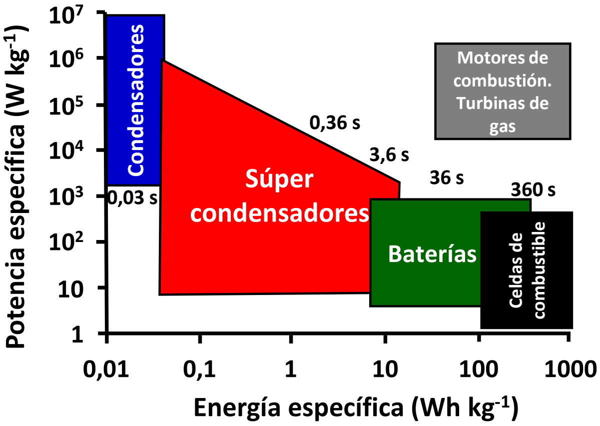

Figura 1. Diagrama de Ragone para los principales dispositivos empleados para el almacenamiento de energía.

En la Tabla 1 se comparan las características más importantes entre condensadores electrolíticos, supercondensadores y baterías [2]. En comparación con las baterías recargables, los SCs tienen una densidad de 1 a 500 veces menor, una potencia de 1 a 3 órdenes de magnitud superior y alta reversibilidad de carga/descarga. Adicionalmente, los supercondensadores no tienen partes movibles, son dispositivos seguros, no requieren enfriamiento ni otras instalaciones o servicios auxiliares, no necesitan mantenimiento, son ampliamente modulares respecto al voltaje y capacidad, se pueden producir a bajo costo y son muy poco contaminantes [3,4]. Las baterías almacenan energía mediante reacciones químicas capaces de generar carga mientras que los supercondensadores almacenan energía electroquímica directamente como carga.

Tabla 1. Características de los dispositivos para almacenamiento de energía eléctrica

Característica	Condensador electrolítico	Supercondensador	Batería
Energía específica (Wh/kg)	< 0,1	1 – 10 h	10-100
Potencia específica (Wh/kg)	>> 10000	500 – 10000	<1000
Tiempo de descarga (s)	10^{-6} a 10^{-3}	10^{-2} s ≤ t ≤ 10^{2} s	0,3 – 3 h
Tiempo de carga (s)	10^{-6} a 10^{-3}	10^{-2} s ≤ t ≤ 10^{2} s	1 – 5 h
Eficiencia carga/descarga (%)	~100	85-98	75 – 85
Ciclos de vida	Infinito	>500000	~1000
Determinante máximo potencial	Espesor y resistencia dieléctrico	Potencial de estabilidad entre electrodo y electrolito	Termodinámica de las reacciones de fase
Determinante carga almacenada	Área electrodo y dieléctrico	Microestructura del electrodo y composición del electrolito	Masa activa y termodinámica

1.1. Supercondensadores

El primer condensador electroquímico fue patentado en 1957 por General Electric Company, quienes diseñaron un dispositivo basado en el modelo de almacenamiento de energía eléctrica en la doble capa, propuesto inicialmente por Helmholtz, este condensador compuesto por electrodos de carbón poroso usaba el mecanismo de almacenamiento de energía en la doble capa para cargarse; a partir de entonces se han diseñado una serie de dispositivos para el almacenamiento de energía entre los que merece la pena destacar los recogidos en la Tabla 2 [2].

Tabla 2. Condensadores comercialmente disponibles, voltaje de operación y capacidad de almacenamiento de energía.

Fabricante	Nombre comercial	Capacidad(F)	Voltaje(V)	Electrodo/electrolito
AsahiGlass	EDLC	500–2000	3.14/42	Carbon/non-aqueous
AVX	Bestcap	0.022–0.56	3.5–12	Carbon/polymer/aqueous
Cap-XX	Supercapacitor	0.09–2.8	2.25–4.5	Carbon/non-aqueous
Cooper	PowerStor	0.47–50	2.3–5	Aerogel/non-aqueous
ELNA	Dynacap	0.333–100	2.5–6.3	Carbon/non-aqueous
Epcos	Ultracapacitor	5–5000	2.3,2.5	Carbon/non-aqueous
Evans	Capattery	0.01–1.5	5.5,11	Carbon/aqueous
Maxwell	Boostcap/Power Cache	1.8–2600	2.5	Carbon/non-aqueous
NEC	Supercapacitor	0.01–6.5	3.5–12	Carbon/aqueous Carbon/organic
NipponChemi-Con	DLCAP	300–3000	2.3,2.5	Carbon/non-aqueous
Ness	NessCap	3–5000	2.3,2.7	Carbon/organic
Matsushita/Panasonic	Goldcapacitor	0.1–2500	2.3–5.5	Carbon/organic
Tavrima/ECOND	Supercapacitor	0.13–160	14–300	Carbon/aqueous

Los supercondensadores son una nueva generación de condensadores similares a los dispositivos de almacenamiento químico de energía, baterías, que pueden almacenar una carga eléctrica moderada, entre 10 a 1000 veces superior a los condensadores convencionales, pero manteniendo prácticamente la misma densidades de potencia. Los supercondensadores también poseen alta capacidad de almacenamiento de energía y altas densidades de potencia (10-10^6 W kg^{-1}), tiempo de respuesta más bajos (0,3 - 3 s) y estabilidad en cada ciclo carga y descarga sin afectar su rendimiento [3,5].

Los supercondensadores se fundamentan en procesos electroquímicos, estos dispositivos están constituidos por un electrolito, dos electrodos (ánodo y cátodo) y un separador poroso que impide el contacto electrónico entre los materiales conductores [6]. El electrolito debe tener una elevada conductividad iónica y una baja conductividad eléctrica de manera que los electrones son obligados a circular por el exterior del dispositivo, proporcionando así la energía deseada. En el caso de los electrodos las conductividades iónica y electrónica deben ser elevadas.

Las principales limitaciones de los supercondensadores son la baja densidad de energía, mayor velocidad de auto-descarga y costes de fabricación más elevados que las baterías. Hoy día se están llevando a cabo grandes esfuerzos para aumentar la densidad de energía mediante la preparación de electrodos con materiales de mayor capacidad específica, materiales con una porosidad que se adapte al tamaño de los iones del electrolito y electrolitos líquidos con un mayor rango de voltaje de trabajo [6].

La introducción de nuevos materiales con propiedades electro-activas y área superficial elevada tales como carbón, polímeros conductores y óxidos metálicos han facilitado el desarrollo de electrodos con una mayor capacidad por unidad de área y mayor eficiencia [1,3,7].

En los supercondensadores la carga eléctrica se almacena debido a la acumulación de iones en la superficie interna de ambos electrodos (ánodo-cátodo), los iones sin solvatar del electrolito se ajustan al poro formando una doble capa eléctrica en combinación con los electrones en el material conductor (Figura 2) [8,9]. La energía almacenada en el condensador se da por un exceso y una deficiencia de electrones durante la carga que es reversible durante la descarga. Idealmente no hay transferencia de electrones en la interfase del electrodo, y el almacenamiento de carga eléctrica es electrostática. La capacidad de almacenamiento de energía en la doble capa se conoce como capacidad de la doble capa eléctrica y la capacidad debido a la presencia de reacciones de oxidación-reducción se conoce como pseudocapacidad [3].

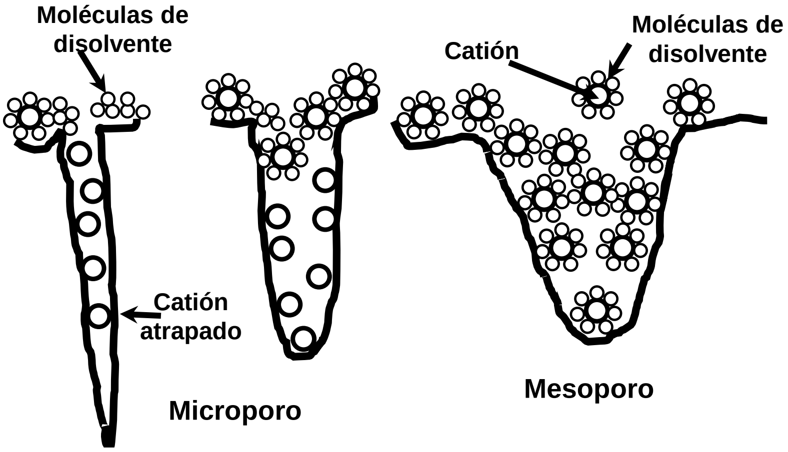

Figura 2. Esquema de adsorción de los iones del electrolito en la superficie de poros con diferentes tamaños.

La clasificación mayoritariamente aceptada para los supercondensadores de acuerdo con diversos autores [5,10,11] es:

i) *Por la forma de almacenamiento de energía:* doble capa electroquímica, pseudocondensadores o híbridos.

ii) *Por el material de los electrodos:* carbón, óxidos de metales de transición o polímeros conductores.

iii) *Por la naturaleza del electrolito:* acuoso, orgánico o líquido iónico.

iv) *Por la simetría de los electrodos:* simétricos (SSCs) si los dos electrodos están construidos del mismo material y asimétricos (ASCs) si los materiales de los dos electrodos son diferentes.

En los condensadores de doble capa electroquímica (EDLCs) el almacenamiento de carga se da por efectos electrostáticos. La corriente generada durante este proceso se debe esencialmente a la acumulación de cargas cuando se aplica una diferencia de voltaje. La carga se acumula en la superficie del electrodo siguiendo la atracción natural de las cargas opuestas. Este proceso es altamente reversible y no hay transferencia de cargas por reacciones químicas o asociadas con procesos farádicos. La ausencia de transformaciones de fase y limitaciones cinéticas ayudan a prolongar el tiempo de vida del condensador [12].

El concepto de doble capa fue desarrollado a partir de los estudios realizados por Helmholtz (1879), Gouy (1910), Chapman (1913) y posteriormente ajustado por Stern y Geary (1924) [13,14,15]. La doble capa se establece cuando un conductor eléctrico está en contacto con un conductor iónico (Figura 3). En una disolución electrolítica, los iones se comportan dependiendo del lugar donde se encuentren en la disolución y de acuerdo a su propia naturaleza. Los iones que se encuentran en el seno de la disolución están rodeados por moléculas polares del disolvente (iones solvatados) y se encuentran rodeados por otros iones también solvatados es decir se hallan en un equilibrio dinámico de cargas. A medida en que los iones se encuentran más cerca de la interfase (electrodo), los iones solvatados son atraídos por la superficie del sólido, por una carga igual pero de signo opuesto y difunden hacia el interior. En la interfase electrodo/electrolito se forma una doble capa electroquímica en la cual se almacena la energía [16].

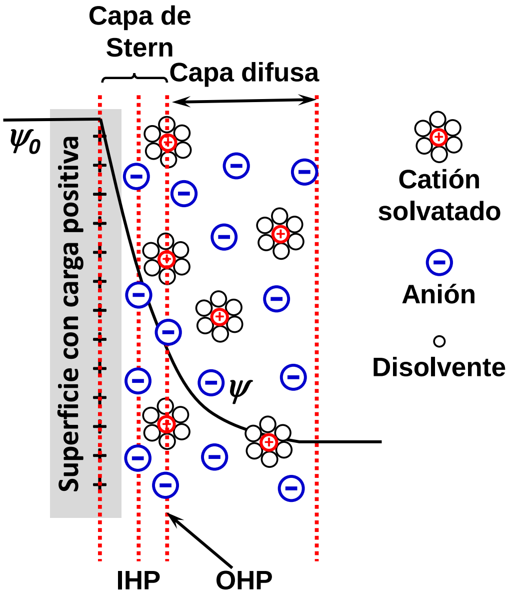

Figura 3. Modelo de Stern para la doble capa eléctrica

La capacidad de la doble capa eléctrica se correlaciona con las propiedades superficiales y porosas de los electrodos (superficie, volumen y distribución del tamaño de poros), y con la concentración de iones en disolución y el tamaño de los mismos. La atracción electrostática de los iones se da principalmente en los microporos, sin embargo la presencia de mesoporos es necesaria para un transporte eficiente de los iones. La principal ventaja de los EDCLs es la habilidad de propagar la carga dinámica, lo que permite una liberación rápida de la energía. La doble capa en la interfase se puede formar rápidamente lo que se traduce en altas tasas de potencia, propiedad inherente de un EDLC en comparación con una batería convencional donde se requiere el transporte de masa a través de distancias más largas [4].

El comportamiento de un condensador de doble capa eléctrica durante la carga y la descarga se representa mediante el esquema de la Figura 4. En el diseño de EDCLs los principales objetivos son optimizar la estructura porosa para adaptarla a los iones del electrolito, aumentar el área superficial, disminuir la distancia entre los electrodos y aumentar la ventana de potencial [5,17,18].

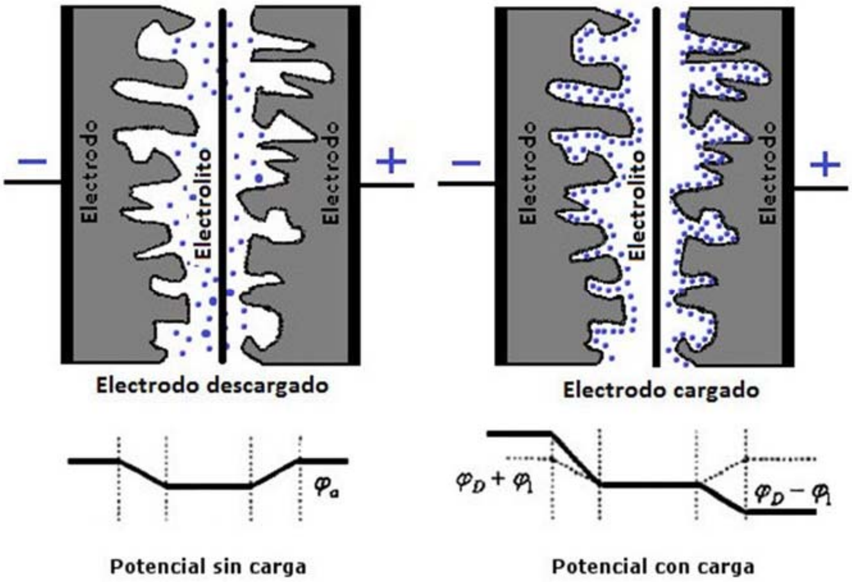

Figura 4. Esquema de carga y descarga de un supercondensador de doble capa.

A pesar de la necesidad de electrodos con un área superficial alta, para obtener una elevada energía almacenada en un dispositivo razonablemente pequeño, existen otros aspectos químico-físicos de la superficie que son críticos para el rendimiento del electrodo. La capacidad interfacial de la doble capa (μF cm^{-2}) depende en primer lugar de la distribución de tamaños de poros y de la mojabilidad de la superficie, parámetros que determinan la accesibilidad al sistema poroso de un electrolito dado, y en segundo lugar de las características estructurales de la fase sólida [19]. La conductividad de los electrodos de carbón depende del tratamiento térmico, microestructura, hibridación y contenido en heteroátomos que modifican las propiedades electrónicas y el comportamiento electroquímico [13,20,21].

Los materiales de carbón más utilizados para EDLC son los carbones activados debido a que están disponibles comercialmente, son económicos y pueden producirse con un área superficial y una microporosidad alta. Sin embargo, estas dos últimas no son suficientes para un buen desempeño electroquímico, debido a que es necesario que los microporos estén bien interconectados mediante una proporción adecuada de mesoporos [22,23].

La carga en los pseudocondensadores o supercondensadores redox se almacena por medio de la formación de la doble capa eléctrica a partir de rápidas reacciones farádicas en las que se da una transferencia de carga en la interfase entre el electrodo y el electrolito. Este almacenamiento de carga se da por medio de diferentes procesos tales como electro-adsorción, reacciones de óxido-reducción y procesos de intercalación en un rango amplio de potencial. La capacidad se asocia con un proceso de transferencia de carga originada por el material activo [11,22].

En los materiales de carbón la capacidad puede verse incrementada por efectos pseudocapacitivos [24] debido a la presencia de grupos superficiales oxígeno y/o nitrógeno que permiten obtener una capacidad adicional a la capacidad de la doble capa mediante las reacciones farádicas. El incremento de la capacidad se debe principalmente a mecanismos de óxido-reducción y son más significativos que los aportes de la doble capa. La pseudocapacidad originada por grupos funcionales de nitrógeno se da por la presencia de funcionalidades tipo piridina, pirrol, piridona y nitrógeno cuaternario que interactúan con los iones del electrolito y son especies activas [25]. La introducción de grupos quinona, debido a la presencia de grupos funcionales oxígeno, promueve fenómenos pseudofarádicos que pueden influir positivamente en la capacidad del supercondensador.

La deposición de partículas de un óxido de metal de transición es uno de los métodos más prometedores debido a que la capacidad específica se puede mejorar entre 10 a 100 veces dependiendo de la naturaleza del óxido y de carácter netamente pseudocapacitivo. Los óxidos de metales de transición, tienen un área superficial moderada (~100 m^2/g), alta conductividad electrónica (>10 S/cm), fácil procesamiento mediante mecanismos de electroadsorción y/o reacciones redox dominantes. El óxido de rutenio hidratado, RuOx(OH), se ha estudiado extensamente como material de electrodo para supercondensadores debido a su alta capacidad (720 F/g) en electrolito acuoso [26,27]. Las capacidades específicas obtenidas mediante RuO_2 son muy altas, pero el precio de este material ha limitado sus aplicaciones y le han dado preferencia a otros materiales como óxido de manganeso hidratado (α-$MnO_2.nH_2O$) [28]. Algunos de los materiales que se han estudiado como electrodos de supercondensadores son: NiO, $Ni(OH)_2$, MnO_2, Co_2O_3, IrO_2, FeO, TiO_2, SnO_2, V_2O_5, MoO y In_2O_3, de los cuales ninguno se ha usado comercialmente y todavía siguen los trabajos a escala de laboratorio [26].

Otros materiales con propiedades pseudocapacitivas son los polímeros conductores eléctricos (ECPs), conocidos como metales sintéticos debido a su alto grado de dopado y rápido cambio electroquímico. Estos materiales se caracterizan por tener alta conductividad eléctrica, fácil procesado y ser más económicos que los óxidos metálicos. Los procesos de carga y descarga son generalmente rápidos, el almacenamiento de carga está dominado por mecanismos pseudocapacitivos y se caracterizan por altas capacidades específicas (400 F/g). A diferencia de los carbones activados la carga almacenada se acumula en todo el volumen del electrodo. Durante la oxidación (dopado) los iones son transferidos a la cadena principal del polímero y cuando ocurre la reducción (desdopado) los iones son devueltos a la solución. La oxidación de la cadena provoca la apertura de la red polimérica para la penetración de los contra-iones solvatados o su cierre al ser expulsados durante la reducción. Estos cambios de volumen hacen que la estructura se contraiga o se hinche, conduciendo a la degradación mecánica del electrodo, baja estabilidad y disminución de la eficiencia electroquímica durante los ciclos de carga y descarga. Los ECPs más comunes son polianilina (PANI), polipirrol (PPy), poli-tiofenos (PEDOT) [28,29].

En los supercondensadores híbridos los mecanismos de almacenamiento de carga que se llevan a cabo en el ánodo y en el cátodo son diferentes. Los efectos electrostáticos y farádicos se combinan para obtener capacidades de almacenamiento y densidades de energía mayores respecto a los EDCLs, manteniendo la misma densidad de potencia, y sin sacrificar la estabilidad cíclica y accesibilidad que ha limitado a los pseudocondensadores. El mecanismo de operación de los condensadores híbridos se fundamenta en las propiedades intrínsecas de los materiales de los dos electrodos. Algunos supercondensadores híbridos están conformados por un electrodo de doble capa de carbono y otro tipo batería, de tal forma que se aprovecha la alta densidad de energía de las baterías y la alta densidad de potencia de los ECs.

Los electrolitos líquidos empleados en la fabricación de supercondensadores idealmente deben tener una alta conductividad iónica y baja conductividad electrónica (~10 mS cm^{-1}). Adicionalmente, los electrolitos deben tener una baja viscosidad, permanecer líquidos en el intervalo de temperatura de trabajo y ser muy estables durante los ciclos de carga y descarga. El potencial de descomposición del electrolito condiciona el voltaje de trabajo. Así, cuanto mayor sea el intervalo de potencial de trabajo mayor será la capacidad de carga y la densidad energética.

En las soluciones electrolíticas el tamaño del catión y el anión del electrolito y el tipo de disolvente son importantes para lograr una adsorción efectiva de los iones sobre la superficie del electrodo y la formación de la doble capa. La selección del tipo de electrolito depende de la distribución de la porosidad del material de carbón para facilitar la entrada y salida del ion [11,29]. Los electrolitos se clasifican como acuosos, orgánicos y líquidos iónicos. Los electrolitos acuosos requieren que los electrodos posean un tamaño de poro mínimo de 0,5 nm, tienen bajas tensiones de ruptura y baja conductividad electrónica (~1 S/cm para H_2SO_4 1 M). Aunque la ventana termodinámica del agua es 1,23 V, en la práctica el voltaje de operación máximo varía entre 0,7 y 1 V, debido a factores experimentales que son difíciles de controlar y reducen significativamente la energía disponible [24]. La densidad de energía que se puede conseguir con los electrolitos acuosos está alrededor de 3,5 Wh/kg.

Los electrolitos acuosos son los más interesantes desde el punto de vista industrial debido a su bajo costo, manipulación a presión atmosférica, largo tiempo de vida y baja resistencia interna. Los más empleados son ácido sulfúrico, sulfatos e hidróxidos de sodio y potasio.

Los electrolitos orgánicos más usados son sales de amonio cuaternario tales como tetraetilamonio tetraflouroborato ($TEABF_4$), tetraetilamonio trifluorometilsulfonato (TEATFS) o tetraetilamonio metilsulfonato ($TEAMeSO_3$) con propilencarbonato o acetonitrilo como disolventes [24,30,31]. En un medio aprótico el tamaño de los iones solvatados es mayor que en un medio acuoso por lo que los poros más estrechos no son accesibles para los iones y no contribuyen a la capacidad de la doble capa [22].

Este tipo de electrolitos se caracterizan por tener una conductividad electrónica muy baja (~0,05 S/cm) y una resistencia específica más alta que el medio acuoso, lo cual disminuye la potencia máxima. Este efecto se puede compensar con un incremento de la ventana de potencial. Así, Los electrolitos orgánicos permiten un potencial de operación hasta 2,3–2,7 V, superior a los electrolitos acuosos. Un aumento de potencial significa un aumento en la densidad de energía y una disminución del número de celdas requeridas para un banco de potencia. En el caso de los electrolitos orgánicos se han reportado densidades de energía de hasta 18 Wh/kg.

Sin embargo, los electrolitos apróticos tienen un alto coste debido a que necesitan unas condiciones específicas de producción (hay que evitar el contacto con el aire y la humedad), son muy viscosos lo que dificulta su manipulación, inestables en presencia de los electrodos de carbón y contaminantes [1,24].

Los líquidos iónicos (ILs) son sales orgánicas en estado líquido a temperatura ambiente, sintetizados mediante la combinación de un catión orgánico con una amplia variedad de aniones poliatómicos, muy asimétricos y voluminosos, unidos por fuerzas atractivas más débiles que las sales iónicas convencionales. Las propiedades de los ILs dependen principalmente del tipo de catión y el anión, así como de la longitud del grupo alquilo [32]. Se trata de una nueva clase de electrolitos propuestos como una opción muy prometedora para obtener un alto potencial en un ambiente favorable para su aplicación en dispositivos EES [33]. Estos se caracterizan porque son no volátiles, no inflamables, fáciles de manipular, de baja conductividad iónica y conductividad electrónica relativamente alta, de bajo coste de producción y muy alta viscosidad [34,35]. Aunque la característica más atractiva es su estabilidad a elevados valores de potencial (3–3,5 V).

1.2. Parámetros característicos de los supercondensadores

La carga almacenada, Q, en un condensador es directamente proporcional a la capacidad equivalente y a la diferencia de potencial, ΔV, como indica la ecuación (1).

$$Q = C \times \Delta V \tag{1}$$

donde Q es la carga en Culombios, V el voltaje en Voltios y la capacidad C en Faradios. Un condensador electroquímico opera bajo el mismo principio de los condensadores electrostáticos convencionales. La capacidad de un condensador viene determinada por la ecuación (2).

$$C = \frac{Q}{V} = \frac{S\varepsilon}{d} \tag{2}$$

donde ε es la permitividad o constante dieléctrica del electrolito, S el área superficial de la interfase electrodo/electrolito y d es el grosor del dieléctrico. Sin embargo, cuando se aplica un voltaje entre los dos electrodos de un SC, Figura 4, se forma una doble capa sobre cada electrodo. Por tanto, el mecanismo completo se comporta como dos condensadores conectados en serie y su capacidad, C_t, viene dada por la ecuación (3) [23].

$$\frac{1}{C_t} = \frac{1}{C_1} + \frac{1}{C_2} \tag{3}$$

donde C_1 y C_2 son los valores de la capacidad de la doble capa eléctrica en cada electrodo. Si el condensador está compuesto por dos electrodos de diferente capacidad, el componente con menor capacidad es el que contribuye más al valor de la capacidad total debido a la proporcionalidad inversa. La capacidad depende esencialmente del material del electrodo.

La capacidad de cada electrodo de un condensador de doble capa se puede calcular mediante la ecuación (2) pero ahora d es el grosor de la doble capa eléctrica. Este grosor depende de la concentración del electrolito y del tamaño de sus iones, y está entre 0,5 y 1 nm para los electrolitos concentrados. Si este valor de d se introduce en la ecuación (2) se puede tener una idea de la gran ventaja de los SCs sobre los condensadores convencionales. Debido a la distancia extremadamente corta entre cargas en la interfase la capacidad alcanza los 10–20 $\mu F/cm^2$. Adicionalmente, al aumentar la superficie de los electrodos mediante el uso de materiales porosos se pueden obtener altas capacidades específicas.

A veces puede surgir además otro tipo de capacidad debida a la transferencia de carga farádica y no debida a cargas electrostática y que se denomina pseudocapacidad para distinguirla de la capacidad debida a la doble capa eléctrica. Esta pseudocapacidad tiene su origen en las rápidas reacciones redox que pueden ocurrir entre el electrodo y el electrolito, como ya se ha explicado anteriormente.

La energía específica almacenada en un SC, E (kWh/kg), es proporcional a la capacidad y al cuadrado del voltaje según la ecuación (4) [36]. El voltaje de carga depende principalmente del potencial de estabilidad del electrolito, por lo que este es uno de los factores que limita la densidad de energía.

$$E = \frac{1}{2} C V^2 \tag{4}$$

La potencia específica de un SC, P (W/kg), indica la rapidez con que la energía específica almacenada puede extraerse del sistema para ser utilizada, y se define mediante la ecuación (5).

$$P = \frac{E}{\Delta t} \tag{5}$$

donde $\triangle t$ es el tiempo de descarga. La resistencia en serie equivalente (*ESR*) de un SC es igual a la suma de las resistencias de todos los materiales que componen el dispositivo entre los contactos externos (material del electrodo, negro de carbón conductor, aglomerante, separador y electrolito). Con objeto de aumentar la potencia, es necesario minimizar dicha resistencia.

Conocida la resistencia y la capacidad se puede obtener la constante de tiempo, τ (s), según la ecuación (6). Esta constante de tiempo indica la rapidez con la que puede cargarse o descargarse un condensador.

$$\tau = ESR \times C \tag{6}$$

Si el comportamiento del electrodo es capacitivo, es decir, el sistema almacena energía electrostáticamente y no existen reacciones redox, el circuito equivalente consiste en un condensador y una resistencia en serie (Figura 5) [24].

Figura 5. Circuito equivalente RC en serie

La movilidad de los iones depende del tamaño y volumen de los poros y de la tortuosidad de la matriz carbonosa, por lo que un circuito equivalente está compuesto por las resistencias distribuidas a través de todo el material [22]. Los poros con tamaños diferentes tienen diferentes constantes de tiempo. Adicionalmente, se debe tener en cuenta la resistencia entre las partículas y el electrolito y la resistencia de contacto interparticular. Estas consideraciones pueden ser representadas por un circuito equivalente RCC, en el cual están involucrados una serie de resistencias y capacidades debidas a los poros de diferente tamaño (Figura 6). Este modelo se ajusta más para aplicaciones reales de almacenamiento de energía [37,38].

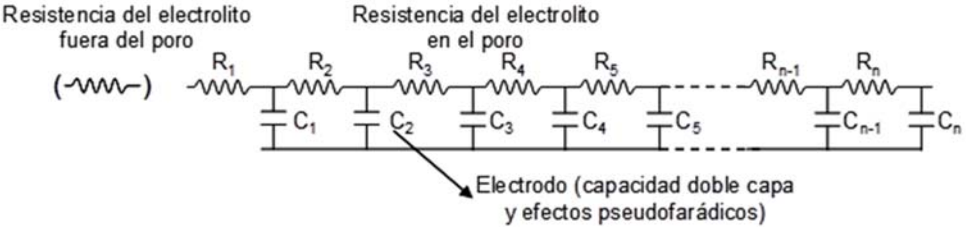

Figura 6. Modelo de circuito equivalente de un material poroso

La capacidad de un condensador varía durante cada carga y descarga, aunque idealmente un condensador debe almacenar siempre la misma carga. Sin embargo, en la práctica estos dispositivos experimentan una auto-descarga en el estado de carga que es causada por fugas de corriente, por el deterioro de los electrodos o por mecanismos de transferencia de carga a través del medio dieléctrico. Este comportamiento no ideal debe ser mínimo para mejorar la eficiencia de carga-descarga y la fiabilidad de los dispositivos comerciales [39].

La auto-descarga a través de una resistencia R, está dada por el cambio de potencial en función del tiempo según la ecuación (7) [40].

$$V(t) = V_0 \exp\left(-\frac{t}{RC}\right) \qquad (7)$$

En la actualidad se emplean diversas técnicas experimentales para determinar el rendimiento electroquímico de un material, siendo los más usuales la voltametría cíclica, espectroscopía galvanostática de carga/descarga y la espectroscopía de impedancia electroquímica, técnicas que se describirán más adelante.

1.3. Materiales de carbón como electrodos

Los materiales de carbón generalmente usados como electrodos de supercondensadores son geles de carbono, carbones activados, carbones mesoporosos ordenados, nanotubos y materiales de carbón compuestos.

Todos estos materiales son muy versátiles en cuanto a sus propiedades tales como área superficial, porosidad y química superficial. Además suelen presentar alta conductividad eléctrica y algunos de ellos pueden prepararse con distintas formas como monolitos, esferas y láminas. Los materiales de carbón usados en la presente Tesis Doctoral han sido monolitos (aerogeles) y esferas de carbono y carbones activados, los cuales se describirán en los siguientes subapartados.

1.4. Monolitos (aerogeles) de carbono

Los geles de carbono son un grupo de materiales avanzados introducidos por Pekala en 1989 [41,42] que se obtienen por carbonización de geles orgánicos. Estos geles orgánicos se preparan mediante una polimerización sol-gel de ciertos monómeros orgánicos como veremos más adelante. La síntesis sol-gel se aplicó originalmente a la preparación de sólidos inorgánicos y la química-física del proceso se ha detallado en varios trabajos y libros [43,44,45,46,47]. La ventaja de la síntesis sol-gel es que se obtienen materiales de alta pureza, homogeneidad y porosidad controlada.

Los geles de carbono se pueden obtener en forma de monolitos, esferas, cuentas, polvos, y láminas y poseen una micro y mesoporosidad bien desarrollada y una superficie específica elevada, propiedades que pueden diseñarse al controlar los ingredientes usados y los diferentes pasos del proceso de obtención. Por estas características los geles de carbono se utilizan en distintas aplicaciones como adsorbentes [48,49,50], soportes de catalizadores [51,52,53,54,55], aislantes térmicos y/o acústicos [56,57,58,59], para el refuerzo de fibras [60,61,62], y como electrodos en celdas de combustibles [63,64] y supercondensadores [65,66,67,68].

Los geles de carbono están formados por un retículo tridimensional de nanopartículas primarias interconectadas entre sí. Los microporos se desarrollan en las partículas primarias y los meso y macroporos se forman en los espacios entre las partículas primarias inicialmente ocupados por el disolvente. Por tanto, se puede controlar independientemente la concentración de micro y mesoporos, lo que es una ventaja de los geles de carbono como materiales porosos.

En la preparación de los geles de carbono se pueden distinguir tres etapas importantes. La primera es la preparación de la mezcla del sol, su gelificación y subsiguiente curado. La segunda etapa es el secado del gel orgánico húmedo y la tercera es la carbonización del gel seco y a veces la activación del producto carbonizado. Un esquema del proceso se representa en la Figura 7.

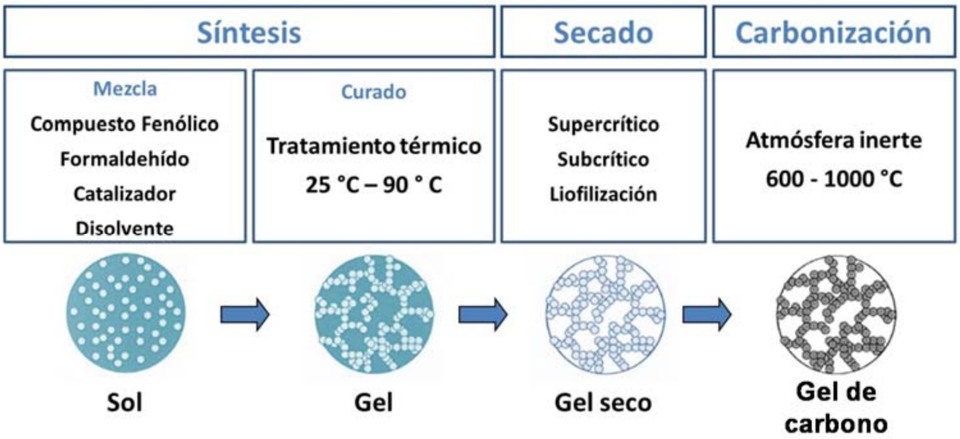

Figura 7. Esquema de preparación de geles de carbono

En la preparación de los geles orgánicos se han utilizado varios precursores como resorcinol (R)-formaldehído (F) [42,69], melamina-formaldehído [70,71], furfural-fenol [72,73,74], fenol-formaldehído [75], etc., usando diferentes disolventes (agua, metanol, etanol y otros disolventes orgánicos) y catalizadores básicos (carbonatos e hidróxidos) o ácidos (orgánicos e inorgánicos). La reacción de R con F es la que más se ha estudiado. La Figura 8 muestra un esquema del mecanismo de reacción propuesto para la polimerización de mezclas RF [76,77,78]. El mecanismo comienza con la formación de los aniones R^- debido a la presencia del catalizador. Los aniones R^- son más activos que las moléculas R y continúa con la reacción de adición de las moléculas F a las posiciones libres del anillo aromático (posiciones 2, 4 y 6) formando derivados hidroximetil-R. En seguida comienzan las reacciones de policondensación de los grupos hidroxílicos, por lo que el subproducto es agua. En esta segunda etapa de reacción se forman estructuras poliaromáticas en las que los anillos aromáticos están enlazados entre sí mediante puentes metilen $\left(-CH_2-\right)$ y metilenéter $\left(-CH_2-O-CH_2-\right)$.

Los productos de condensación forman “clusters” de macromoléculas debido a la agrupación de partículas primarias coloidales que se comienzan a formar dando lugar a una estructura entrelazada [78]. La disolución final pierde fluidez y se forma el gel.

El pH inicial de la disolución es una variable muy importante en la preparación de los geles orgánicos porque controla la cinética de polimerización, el entrecruzamiento y, por tanto, la morfología, el tamaño de partícula y la porosidad de los geles finales [79].

El pH de la disolución depende principalmente del tipo de catalizador y tipo de disolvente utilizado. A bajos pHs se promueven las reacciones de condensación, obteniéndose un alto entrecruzamiento y una estructura muy fuerte, mientras que a altos pHs se obtiene geles con elevado volumen de poros y área superficial. A pHs muy altos se dificulta la polimerización-condensación y se puede causar un colapso de la nanoestructura, dando lugar a geles de carbono sin un desarrollo poroso [80]. Los valores de pH utilizados para la síntesis de geles de carbono están entre 5.4 y 7.6.

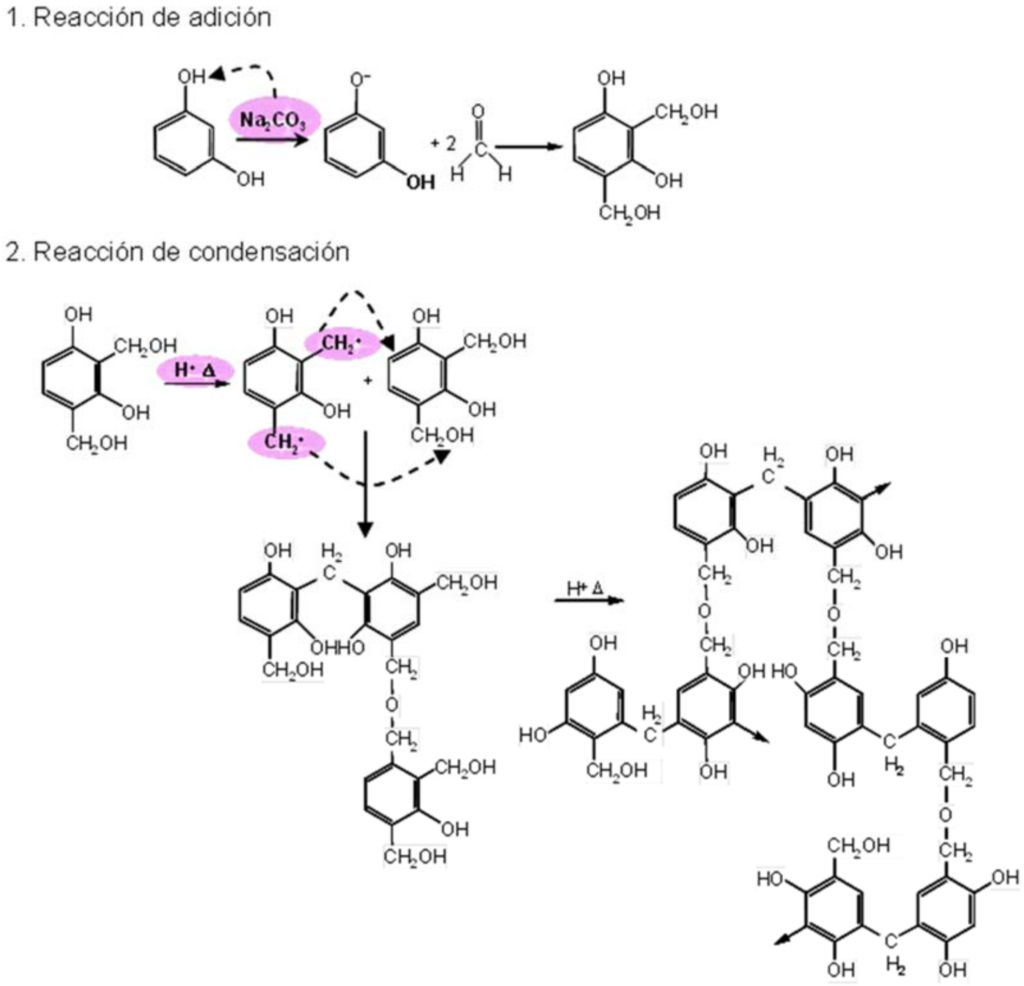

Figura 8. Esquema del mecanismo de la reacción de polimerización de mezclas RF

La polimerización de mezclas R-F permite la formación de un gel transparente que a medida que avanza la reacción va cambiando de color hasta tornarse de colores oscuros. El color, la transparencia y la dureza del gel orgánico obtenido dependen de las relaciones molares R/C, R/W y R/F [81,82]. En los artículos publicados por Al-Muhtaseb [76,83] se hace una extensa revisión bibliográfica sobre la influencia de las condiciones de síntesis en las propiedades finales de los geles de carbono.

La concentración del catalizador es la variable que permite controlar el número y el tamaño de los "clusters" generados durante la polimerización R-F. La variación de la relación molar resorcinol/catalizador (R/C) influye sobre la densidad [82], el área superficial y las propiedades mecánicas de los geles resultantes (Figura 9). Cuando la relación R/C es baja (R/C<50) se forma un gel con partículas poliméricas pequeñas que están interconectadas entre sí, obteniendo un gel con aspecto fibroso y densidad elevada. En el caso de relaciones R/C altas (R/C>200) se forma un gel con partículas coloidales de mayor tamaño que están conectadas por cuellos estrechos con aspecto de collar de perlas [82,84,85]. Los valores de R/C más utilizados en la preparación de los geles de carbono varían entre 50-300, aunque en algunos casos se han preparado con valores superiores (800-1500). La relación molar R/F = 1/2 es la más empleada, ya que se obtienen mejores características texturales [42]. Las relaciones R/F = 1/1 y 1/3 permiten entrecruzamientos de baja densidad e inducen a un efecto de dilución, respectivamente.

La gelificación es la transición gradual de un líquido viscoso a un sólido viscoelástico y antes de que se produzca la formación del gel es cuando se le da la forma que tendrá finalmente el gel de carbono. Así, si se quiere obtener en forma de monolito la disolución coloidal se vierte en moldes de la forma deseada donde se procede a la formación del gel y al curado del mismo.

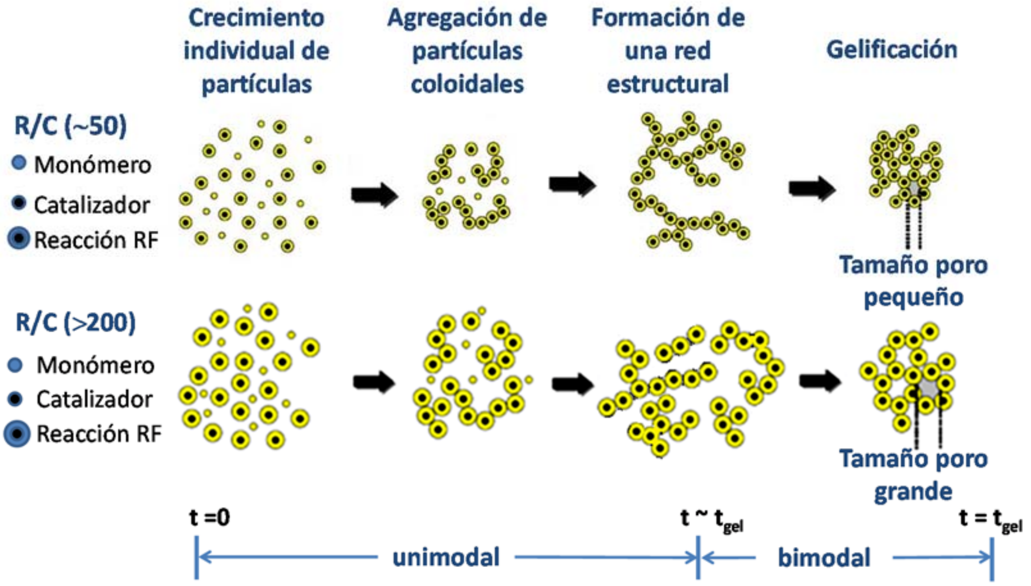

Figura 9. Influencia de la concentración del catalizador en la polimerización RF

La segunda etapa en la preparación de los geles de carbono consiste en el secado del gel orgánico una vez obtenido. Mediante el secado se elimina el disolvente utilizado como medio de reacción, lo que deja un espacio vacío entre las partículas primarias dando lugar al desarrollo del retículo meso- y macroporoso. Los cambios en la textura porosa del gel orgánico están asociados a procesos de encogimiento y depende esencialmente del método de secado utilizado. Por tal motivo, este es un paso muy importante en la síntesis de los geles de carbono, ya que controla la meso y macroporosidad del producto final y, por tanto, su densidad [86]. Así, las condiciones de secado del gel orgánico deben seleccionarse cuidadosamente con el fin de evitar el colapso de la textura meso y macroporosa [87,88].

El secado del gel orgánico húmedo está controlado por la permeabilidad y la presión capilar y se puede realizar bajo condiciones subcríticas, supercríticas o mediante liofilización (congelación-sublimación), lo que da lugar a xerogeles, aerogeles y criogeles, respectivamente [69,76,88,89,90].

En el secado subcrítico los geles se secan por simple evaporación del disolvente a presión por debajo de la crítica, a presión atmosférica o vacío, y temperaturas entre 100 y 150 ºC. Este tipo de secado puede conducir a un colapso de la textura porosa, debido a los cambios en tensión superficial del disolvente durante la formación de la interfase líquido-vapor. El colapso conduce a una contracción del gel seco dando lugar a un polímero denso [51]. En algunos casos se realiza un cambio de disolvente antes del secado con objeto de reducir las fuerzas capilares responsables del colapso de la textura porosa. Así, a veces el agua es intercambiada con un disolvente de menor tensión superficial como acetona o ciclohexano. El secado subcrítico a veces puede dar lugar a xerogeles porosos cuando la estructura del gel orgánico húmedo es lo suficientemente fuerte como para aguantar las altas presiones capilares [79,86]. Este método de secado es el más simple, rápido y económico, y puede ser adecuado en algunos casos.

El secado con microondas es una técnica que se ha empleado recientemente. Las microondas son ondas electromagnéticas con un intervalo de frecuencia de 0,3 a 300 GHz y longitudes de onda de 1 cm a 1 m [91]. Las microondas se generan por medio de un magnetrón, el cual es básicamente un tubo alimentado por un circuito electrónico capaz de transformar la energía eléctrica de frecuencia industrial en energía electromagnética. El uso de las microondas en materiales constituidos por moléculas polares como el agua, permite que la radiación electromagnética penetre los cuerpos, generando un calentamiento casi instantáneo de las piezas según sea su tamaño sin importar su morfología. Las microondas inducen un calentamiento interno efectivo con lo que se pueda ahorrar tiempo y energía. Kang y col. [92] y Calvo y col. [93] utilizaron la técnica de calentamiento por microondas no solo para el secado de geles de carbono sino también en pasos intermedios de síntesis como gelación y curado, obteniendo xerogeles con características similares a los obtenidos por secados convencionales.

El secado supercrítico es el mejor método para eliminar el disolvente y preservar la textura porosa de los geles húmedos. En este caso el disolvente del gel húmedo, generalmente agua, se intercambia primero con otro disolvente orgánico como metanol, etanol o acetona. Posteriormente el disolvente intercambiado se intercambia de nuevo con CO_2 líquido (T_c = 31 ºC y P_c = 7,4 MPa), el cual se transforma en un fluido supercrítico a 40 ºC y 9 MPa, con tensión superficial nula, pudiendo eliminarse del interior de la textura porosa del gel sin que ésta colapse. La técnica de secado con fluidos supercríticos es el método más indicado para obtener carbones con características mesoporosas. Las áreas superficiales y volúmenes de poros de los materiales obtenidos son, generalmente, más altos respecto a los secados en condiciones subcríticas [51]. Sin embargo, este método de secado es más complicado y caro que el secado subcrítico.

En el secado por liofilización, el disolvente inicialmente se congela y después se elimina por sublimación, evitando la interfase líquido-vapor. Esta técnica es efectiva para preparar carbones con una estructura porosa controlada. La eliminación del disolvente de los poros se da por sublimación a vacío, donde las fuerzas capilares no ejercen presión sobre la estructura porosa [94,95]. Sin embargo, cuando el disolvente es agua su expansión durante la congelación conduce a una rotura del gel dando lugar a macroporos. Por tal motivo, en algunas ocasiones es necesario utilizar un disolvente distinto al agua para evitar deteriorar la textura porosa formada.

La tercera etapa en la preparación de los geles de carbono es la carbonización o pirólisis de los geles orgánicos secos. Este proceso se lleva a cabo calentando a una temperatura entre 600 y 1500 ºC en presencia de un flujo de gas inerte (N_2, Ar, He). Durante este proceso el gel orgánico pierde hidrógeno y los grupos funcionales que contienen oxígeno enriqueciéndose en carbono, dando lugar a un residuo carbonoso con una estructura muy rica en carbono.

A bajas temperaturas de carbonización el volumen de macroporos disminuye y el de mesoporos aumenta debido al encogimiento del material, mientras que el volumen de microporos y el área superficial incrementan como consecuencia de la evolución de gases durante la carbonización [43,79]. A altas temperaturas de carbonización todos estos parámetros tienden a disminuir y a muy altas temperaturas de carbonización (≥ 2000 ºC) ocurre una grafitización parcial de diferentes zonas del gel de carbono [96].

Finalmente, el gel de carbono obtenido se puede activar mediante procesos físicos o químicos de igual forma que los carbones activados. Estas formas de activación se verán en el apartado de los carbones activados. La activación del gel de carbono tiene como finalidad incrementar el área superficial, el volumen y el tamaño de los poros creados durante la carbonización.

1.5. Esferas de carbono

Los materiales inorgánicos de carbono pueden sintetizarse con gran variedad de formas a escala coloidal (por debajo de 1 μm) y micro (entre 1 y 100 μm). Las esferas de carbono han atraído un gran interés recientemente debido a sus aplicaciones, fundamentalmente en el campo del almacenamiento y conversión de la energía, así como en catálisis, adsorción, uso como moldes y en la liberación controlada de fármacos [97].

La forma esférica de las partículas se obtiene durante su síntesis y está determinada por consideraciones de minimización de la energía potencial de las mismas. Las esferas de carbono se clasifican de acuerdo a su tamaño, la orientación de las capas de C en su interior (concéntrica, radial o al azar), la morfología (sólida, hueca o corteza-núcleo) y a su método de preparación.

Las esferas de carbono se pueden sintetizar usando una gran variedad de precursores de C y métodos. Las técnicas usadas son: deposición química en fase vapor (CVD), descarga con arco, ablación laser, procesos térmicos del plasma, descomposición térmica o quemado de hidrocarburos en fase gaseosa, procesos a alta presión y temperatura y por carbonización de esferas de polímeros obtenidas mediante reacciones de polimerización a bajas temperaturas (< 250 ºC).

El método de carbonización de esferas poliméricas obtenidas a temperaturas menores de 250 ºC es uno de los más usados en la bibliografía, llevándose a cabo mediante diferentes procesos los cuales se han clasificado recientemente [97] de acuerdo con el mecanismo de formación de las esferas. Esta clasificación incluye los siguientes procesos: polimerización por emulsión y sus derivadas emulsión sembrada y emulsión inversa, polimerización por precipitación y su derivada polimerización por dispersión, polimerización por suspensión, uso de moldes sólidos, pulverización y secado y tratamiento hidrotermal de carbohidratos y biomasa en general. De todos estos procedimientos experimentales los que se han seguido en esta tesis son los de polimerización por emulsión y mediante uso de moldes sólidos.

En la polimerización por emulsión los monómeros, el iniciador de la polimerización, el medio dispersante y el estabilizador del coloide constituyen inicialmente un sistema no homogéneo que da como resultado partículas de dimensiones coloidales que contienen el polímero formado [98]. A veces se usan surfactantes en la polimerización por emulsión, lo que a menudo implica la solubilización de los monómeros y oligómeros en micelas antes de que las partículas se formen y crezcan.

Los surfactantes pueden también incrementar la solubilidad de algunos polímeros en disolución acuosa. Los copolímeros bloque no iónicos son una familia importante de surfactantes que se usan ampliamente en procesos de emulsificación. Estos poseen excelentes propiedades interfaciales, son de bajo coste, no tóxicos y biodegradables [99]. Uno de los más usados es el copolímero tribloque, óxido de polietileno-óxido de polipropileno-óxido de polietileno, conocido por su nombre comercial Pluronic.

Los monómeros generalmente usados en este método de polimerización por dispersión son compuestos fenólicos reactivos como resorcinol, pirocatecol, floroglucinol, etc., los cuales se polimerizan en presencia de formaldehído mediante un proceso sol-gel similar al explicado en el apartado anterior para la obtención de geles de carbono. Una vez obtenidas las esferas poliméricas estas son carbonizadas a alta temperatura y, a veces, activadas siguiendo los mismos métodos empleados en la preparación de los carbones activados. La activación incrementa la porosidad y área superficial de las esferas de carbono.

El uso de moldes sólidos para la obtención de carbones porosos ha atraído bastante atención desde que Ryoo fue el primero que sintetizó carbones mesoporosos usando como molde sílice MCM-48 [100]. La aplicación de este método a la preparación de esferas de carbono implica los siguientes pasos. Preparación de los moldes, que serían partículas esféricas inorgánicas u orgánicas; infiltración o recubrimiento de los moldes con el precursor de carbono y posterior polimerización del mismo;

carbonización del material compuesto polímero-molde y eliminación del molde [97].

Este método de obtención de esferas de carbono puede ser costoso y tedioso, especialmente cuando el molde se debe preparar y posteriormente eliminar. Sin embargo, tiene la ventaja de producir esferas de carbono con diferentes morfología: sólidas, huecas (a veces llamadas cápsulas) y corteza-núcleo. Los moldes más frecuentemente usados son, sílice, sílice mesoporosa, aluminosilicatos y en menor extensión polímeros orgánicos como poliestireno. Los precursores de carbono son muy variados: resorcinol-formaldehído, melamina-formaldehído, resinas fenólicas, pirrol, alcohol furfurílico, etc.

Muchas de las aplicaciones de las esferas de carbono son las mismas que las de los carbones activados y otros carbones porosos. Sin embargo, tienen la ventaja frente a estos materiales de poseer baja relación superficie externa/volumen, alta densidad de empaquetamiento y alto transporte de masas, facilidad de síntesis y de dopaje con otros elementos y facilidad de ajustar su tamaño y morfología.

1.6. Carbones activados

Los carbones activados [101] están formados mayoritariamente por Csp^2, existiendo en ellos unidades estructurales básicas a nivel nanométrico o micrométrico con un cierto ordenamiento grafítico y que se encuentran unidas entre sí, de una forma desordenada, por carbono amorfo con hibridación sp^2 y sp^3.

Los carbones activados son sólidos esencialmente microporosos, aunque en la mayoría de los casos también contienen meso y macroporos, presentando una distribución polimodal de poros. Los microporos son los más abundantes y es donde se desarrolla la mayor parte del área superficial de estos materiales.

Figura 10. Representación esquemática de la porosidad de un carbón activado. A: macroporos, B: mesoporos, C: microporos y D: poros cerrados

La estructura porosa de un carbón activado se representa esquemáticamente en la Figura 10, ésta se dice que es arborescente porque para llegar a los microporos hay que pasar por los macro (tronco del árbol) y mesoporos (ramas), que constituyen así arterias de transporte para las moléculas o iones del adsorbato hacia los microporos que es donde se producen los fenómenos de adsorción. Una característica de los microporos de los materiales carbonosos en general es que estos tienen forma de rendija, ya que las paredes de los mismos están formadas por láminas grafénicas.

La materia prima usada en la preparación de los carbones activados debe tener un alto contenido en C, bajo contenido en materia inorgánica, debe ser abundante y barata y fácil de activar. En la práctica estas materias primas son de origen vegetal y fósil, como son los residuos agrícolas (madera, huesos y cáscaras de frutas, etc.) y carbones minerales (lignitos, antracitas, etc.). Las propiedades finales del carbón activado dependen del precursor usado y del proceso de activación seguido [102].

La activación puede ser física o química. La activación física generalmente se lleva a cabo en dos pasos. Primero se realiza una carbonización de la materia prima en atmósfera inerte a alta temperatura (~800 ºC), durante la cual se desprende la materia volátil (gases y vapor de agua) y alquitranes dejando un residuo de mayor contenido en C que la materia prima original, y con un retículo poroso rudimentario que se desarrollará posteriormente durante la activación. El segundo paso es la activación, que tiene como objetivo incrementar el volumen de poros mediante la creación de nuevos poros y el ensanchamiento de los ya existentes. Este paso se lleva a cabo a temperaturas entre 800 y 1000 ºC en flujo de vapor de agua o CO_2, a veces se introduce aire en el horno de activación junto a algunos de los gases anteriores. Las reacciones de gasificación son las siguientes:

$$C + H_2O \rightarrow CO + H_2 \qquad \Delta H = +117 \text{ kJ/mol}$$

$$C + CO_2 \rightarrow 2\,CO \qquad \Delta H = +159 \text{ kJ/mol}$$

La reacción con vapor de agua también conduce a la de desplazamiento del gas de agua catalizada por la superficie del carbón

$$CO + H_2O \rightarrow CO_2 + H_2$$

Al ser las reacciones endotérmicas se pueden controlar bastante bien. A veces se introduce aire en el horno que oxida al CO y al H_2 de acuerdo con las reacciones exotérmicas:

$$CO + 1/2\ O_2 \rightarrow CO_2 \qquad \Delta H = -285 \text{ kJ/mol}$$

$$H_2 + 1/2\ O_2 \rightarrow H_2O \qquad \Delta H = -238 \text{ kJ/mol}$$

Estas reacciones suministran un calor extra a las reacciones de activación (haciendo que se use menos energía en calentar el horno) y al mismo tiempo eliminan del reactor el CO y el H_2 que son fuertes inhibidores de las reacciones de gasificación.

El volumen y distribución del tamaño de los poros en el carbón activado final se pueden controlar mediante el agente activante usado y la temperatura y tiempo de activación.

La activación química generalmente se usa con la materia prima de origen vegetal y se suele llevar a cabo en una sola etapa. Para ello, la materia prima se impregna con un agente activante en la forma de disolución de carbonatos o hidróxidos alcalinos (K o Na) o H_3PO_4. El material impregnado se seca y se piroliza en atmosfera inerte entre 400 y 700 ºC. El sólido obtenido se lava para eliminar el agente activante. Durante la pirólisis el agente activante reacciona con la materia prima lo que da lugar a su carbonización y aromatización y a la creación de la textura porosa. En el caso de la activación química las propiedades superficiales del carbón activado obtenido dependen de la materia prima usada, la proporción materia prima/agente activante y la temperatura y tiempo de activación [83,101].

Los carbones activados se preparan en forma de polvo (10 < Ø < 50 μm) o granular (0,5 < Ø < 4 mm). El polvo se puede compactar a presión y con la ayuda de aglutinantes que dan lugar a monolitos de diferentes formas. El monolito tiene un área superficial y porosidad menor que el material en polvo del que procede. El área superficial y textura porosa de los carbones activados varía mucho en función de la materia prima y método de preparación seguido. El área superficial suele estar entre 800 y 2000 m^2/g y el volumen de microporos puede ser de hasta 0,7 $cm^3\ g^{-1}$. Se ha llegado a preparar un carbón activado con un área superficial de ~3000 $m^2\ g^{-1}$ y un volumen de total de poros excepcionalmente elevado, entre 2,0 y 2,6 $cm^3\ g^{-1}$. Este carbón activado es conocido como súper carbón activado, lo comercializa Kansai Coke (Japón), y se prepara a partir de coque y carbón mineral mediante activación química con KOH. Este carbón activado debido a su pequeñísima densidad de partícula es muy difícil de manejar por lo que su utilización no es muy exitosa.

Evidentemente cuanto mayor es el volumen de poros de un material (cualquiera) menor es su densidad de partícula, lo que hace que sea difícil de manejar y que no sea útil para ser usado en sistemas de volumen fijo, ya que se necesitaría un reactor de enorme volumen.

1.7. Química superficial de los materiales de carbón

La química superficial de los materiales de carbón determina su carácter ácido-básico, carga superficial y carácter hidrófobo, la cual depende de la presencia de heteroátomos y de regiones ricas en electrones π. Los heteroátomos más comunes son oxígeno, nitrógeno e hidrógeno y en menor medida azufre, fósforo y cloro. Estos heteroátomos pueden provenir de la materia prima y del método de preparación usado para la obtención de los materiales de carbón o bien ser introducidos en ellos mediante tratamientos químicos adecuados [103,104]. Los heteroátomos se encuentran enlazados en los bordes de las capas grafénicas y a veces en defectos localizados en el interior de ellas formando diferentes grupos funcionales orgánicos como puede verse en la Figura 11 para el caso de los grupos funcionales de oxígeno y nitrógeno.

La química superficial de los materiales de carbón es muy importante cuando estos se usan como electrodos de supercondensadores, ya que pueden dar lugar a fenómenos de pseudocapacidad, por ejemplo mediante reacciones redox, o incrementando la atracción hacia los iones del electrolito. También pueden afectar a la capacidad de mojado de los electrodos, cuando estos se usan en disoluciones acuosas, y a su conductividad eléctrica [105,106].

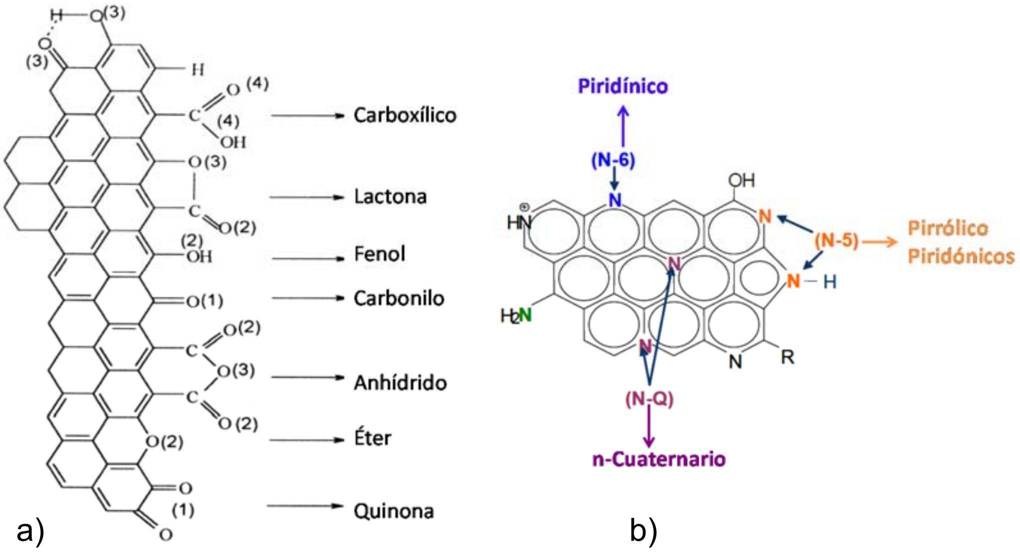

Figura 11. Representación esquemática de los grupos a) oxígeno y b) nitrógeno en superficies carbonosas. N-6: nitrógeno piridínico, N-5: nitrógeno pirrólico o piridónico, N-Q: nitrógeno cuaternario o sustitucional, N-X: formas oxidadas de nitrógeno piridínico.

Los grupos superficiales oxígeno pueden ser de carácter ácido (ácidos carboxílicos, lactonas y fenoles), básicos (quinonas y pironas) y neutros (éteres y aldehídos). En muchos materiales de carbón usados como electrodos de supercondensadores con medio a alto contenido de oxígeno la reacción redox hidroquinona/quinona es la considerada como la mayor responsable de la pseudocapacidad. Los grupos superficiales de oxígeno se pueden introducir en los materiales de carbón mediante tratamientos en fase líquida o gaseosa usando oxidantes como ácido nítrico, peróxido de hidrógeno, peroxidisulfato amónico, aire o vapor de agua [107,108]. La naturaleza de los grupos funcionales de oxígeno incorporados no sólo depende del tipo de agente oxidante utilizado, sino también de las condiciones en las que se lleva a cabo el proceso oxidativo [109,110].

La incorporación de grupos superficiales nitrogenados a los materiales de carbón se puede realizar de dos formas i) directamente durante la síntesis mediante la selección de precursores ricos en grupos nitrogenados como melamina y urea [111,112,113,114], y ii) modificación post-síntesis mediante tratamientos que introduzcan estos grupos, como por ejemplo el tratamiento con amoniaco a alta temperatura [111].

Las diferentes funcionalidades nitrogenadas pueden ser nitrógeno piridínico (N-6), nitrógeno pirrólico o piridónico (N-5), nitrógeno cuaternario o sustitucional (N-Q), formas oxidadas de nitrógeno piridínico (N-X), así como grupos aminas (Figura 1b) [113]. La presencia de las funcionalidades N-5 y N-6 incrementan la carga negativa en las láminas de grafeno, mientras que las funcionalidades N-Q incrementan la carga positiva e influyen sobre la adsorción de los iones del electrolito y la pseudocapacidad [115].

En el caso de los geles y esferas de carbono es fácil la adición de elementos dopantes, metálicos o no metálicos, mediante la adición de los compuestos precursores de estos elementos en la receta original, antes de que polimericen los monómeros empleados. Estos elementos pueden influir en la química superficial del material finalmente obtenido.

2. OBJETIVOS GENERALES DE LA TESIS DOCTORAL

En la presente tesis doctoral se recoge la síntesis y caracterización de una serie de materiales como son las esferas y aerogeles de carbono y carbones activados para su utilización como electrodos de supercondensadores. Estudiándose el efecto de los precursores de carbono y del contenido en nitrógeno sobre la morfología y tamaño de las esferas, así como la química superficial, textura porosa, área superficial y capacidad electroquímica de todos los materiales obtenidos.

Las esferas de carbono se prepararon por polimerización por emulsión a partir de la reacción de resorcinol, pirocatecol y 3-hidroxipiridina con formaldehído usando amoniaco como catalizador. También se prepararon esferas de carbono mediante el uso de sílice como molde sólido y residuos líquidos procedentes del almacenamiento de aceitunas como precursor de carbono. Los objetivos de estos trabajos fueron los siguientes:

i) Comparar los resultados obtenidos al usar pirocatecol en vez de resorcinol como precursor de carbono. Existen muchos estudios sobre la preparación de esferas de carbono usando resorcinol pero muy pocos sobre el uso de pirocatecol, el cual es menos reactivo que el resorcinol.

ii) Comparación de la activación de las esferas de carbono usando KOH como agente activante o ciclos de adsorción-desorción de oxígeno.

iii) Efecto de las funcionalidades de N introducidas en las esferas de carbono al usar 3-hidoxipiridina.

iv) Capacidad de los líquidos residuales procedentes del almacenamiento de las aceitunas en almazaras para producir esferas de carbono sólidas y huecas empleando moldes de sílice micro-mesoporosa y corteza mesoporosa-núcleo sólido.

Los aerogeles de carbono se prepararon mediante la polimerización de resorcinol con formaldehído. Los materiales obtenidos eran fundamentalmente microporosos y el objetivo principal fue estudiar su comportamiento como electrodos de supercondensadores a elevadas velocidades de carga-descarga en electrolitos ácido y básico.

La preparación de carbones activados a partir de residuos lignocelulósicos para aplicaciones en adsorción y catálisis se conoce desde hace tiempo. Sin embargo, recientemente hay un renovado interés en la preparación de estos materiales a partir de residuos lignocelulósicos para su aplicación en el almacenamiento de energía y en la descontaminación de aguas [116,117]. Así en la presente tesis doctoral se han usado los huesos de los frutos de la *Melia Azedarach* y el *Schinus Molle* como precursores de los carbones activados, los cuales se prepararon por activación con KOH de los huesos originales, los huesos previamente carbonizados y los huesos tratados hidrotermalmente. Estos árboles son muy abundantes en países mediterráneos y asiático donde se usan con motivo ornamentales para dar sombra y como sumideros de carbono.

3. BIBLIOGRAFÍA

[1] Kötz R, Carlen M. Principles and applications of electrochemical capacitors. Electrochim. Acta. 2000;45:2483–98.

[2] Pandolfo A, Hollenkamp A. Carbon properties and their role in supercapacitors. J. Power Sources. 2006;157(1):11–27.

[3] Inagaki M, Konno H, Tanaike O. Carbon materials for electrochemical capacitors. J. Power Sources. 2010;195(24):7880–903.

[4] Shi H. Activated carbons and double layer capacitance. Electrochim. Acta. 1996;41(10):1633–9.

[5] Shukla A, Banerjee A, Ravikumar M, Jalajakshi A. Electrochemical capacitors: Technical challenges and prognosis for future markets. Electrochim. Acta. 2012;84:165–73.

[6] Sanz Lázaro J, Álvarez Amarilla JM, Alonso Alonso JA, Rojo Martín JM. Energía eléctrica y materiales: baterías recargables, supercondensadores y pilas de combustible. Madrid, ESP: CSIC - Ministerio de Economía y Competitividad; 2012.

[7] Butler P, Miller J, Taylor P. Energy Storage Opportunities Analysis Phase II Final Report A Study for the DOE Energy Storage Systems Program. Albuquerque USA: Sandia National Laboratories; 2002.

[8] Adhyapak P V, Maddanimath T, Pethkar S, Chandwadkar AJ. Application of electrochemically prepared carbon nanofibers in supercapacitors. J. Power Sources. 2002;109(1):105–10.

[9] Miller JR, Simon P. Fundamentals of electrochemical capacitor design and operation. Electrochem. Soc. Interface. 2008;17(1):31–2.

[10] Halper MS, Ellenbogen JC. Supercapacitors: A Brief Overview. McLean VA: The MITRE; 2006. p. 41.

[11] Sharma P, Bhatti TS. A review on electrochemical double-layer capacitors. Energ. Convers. Manage. 2010;51(12):2901–12.

[12] Lota G, Centeno T, Frackowiak E, Stoeckli F. Improvement of the structural and chemical properties of a commercial activated carbon

for its application in electrochemical capacitors. Electrochim. Acta. 2008;53(5):2210–6.

[13] Zhang Y, Feng H, Wu X, Wang L, Zhang A, Xia T, et al. Progress of electrochemical capacitor electrode materials: A review. Int. J. Hydrogen Energy. 2009;34(11):4889–99.

[14] Simon P, Burke A. Nanostructured Carbons: Double-Layer Capacitance and More. Electrochem. Soc. Interface. 2008;17(1):38–43.

[15] Qu D, Shi H. Studies of activated carbons used in double-layer capacitors. J. Power Sources. 1998;74(1):99–107.

[16] Chang B-Y, Park S-M. Electrochemical impedance spectroscopy. Annu. Rev. Anal. Chem. 2010;3:207–29.

[17] Nishino A. Capacitors: Operating principles, current market and technical trends. J. Power Sources. 1996;60(2):137–47.

[18] Béguin F., Presser V., Balducci A., Frackowiak E. Carbons and Electrolytes for Advanced Supercapacitors. Adv. Mater. 2014; 2219-2251.

[19] Béguin F., Presser V., Balducci A., Frackowiak E. Carbons and Electrolytes for Advanced Supercapacitors. Adv. Mater. 2014; 2219-2251.

[20] Menéndez R, Cazorla-Amorós D, Cordero T. Carbon for energy storage and environment protection 2009 special issue. Energy Fuels. 2010;24(6):3301.

[21] Dandekar M, Arabale G, Vijayamohanan K. Preparation and characterization of composite electrodes of coconut-shell-based activated carbon and hydrous ruthenium oxide for supercapacitors. J. Power Sources. 2005;141(1):198–203.

[22] Frackowiak E, Béguin F. Carbon materials for the electrochemical storage of energy in capacitors. Carbon. 2001;39(6):937–50.

[23] Li W, Chen D, Li Z, Shi Y, Wan Y, Wang G, et al. Nitrogen-containing carbon spheres with very large uniform mesopores: The superior electrode materials for EDLC in organic electrolyte. Carbon. 2007;45(9):1757–63.

[24] Raymundo-Piñero E, Béguin F. Application of nanotextured carbons for supercapacitors and hydrogen storage. In: Bandosz T, editor. Activated Carbon Surfaces in Environmental Remediation. Oxford: Elsevier; 2006. p. 293–343.

[25] Hulicova D, Kodama M, Hatori H. Electrochemical Performance of Nitrogen-Enriched Carbons in Aqueous and Non-Aqueous Supercapacitors. Chem. Mater. 2006;18(9):2318–26.

[26] Jayalakshmi M, Balasubramanian K. Simple Capacitors to Supercapacitors - An Overview. Int. J. Electrochem. Sci. 2008;3:1196–217.

[27] Prasad KR, Koga K, Miura N. Electrochemical Deposition of Nanostructured Indium Oxide: High-Performance Electrode Material for Redox Supercapacitors. Chem. Mater. 2004;16(22):1845–7.

[28] Khomenko V, Raymundo-Piñero E, Frackowiak E, Béguin F. High-voltage asymmetric supercapacitors operating in aqueous electrolyte. Applied Physics A. 2006;82(4):567–73.

[29] Frackowiak E, Khomenko V, Jurewicz K, Lota K, Béguin F. Supercapacitors based on conducting polymers/nanotubes composites. J. Power Sources. 2006;153(2):413–8.

[30] Bleda-Martínez MJ, Lozano-Castelló D, Cazorla-Amorós D, Morallón E. Kinetics of Double-Layer Formation: Influence of Porous Structure and Pore Size Distribution. Energy Fuels. 2010;24(6):3378–84.

[31] Simon P, Gogotsi Y. Materials for electrochemical capacitors. Nature Materials. 2008;7(11):845–54.

[32] Sato T, Masuda G, Takagi K. Electrochemical properties of novel ionic liquids for electric double layer capacitor applications. Electrochim. Acta. 2004;49(21):3603–11.

[33] Sato T, Marukane S, Morinaga T. Ionic Liquids for the Electric Double Layer Capacitor Applications. In: Handy S, editor. Applications of

Ionic Liquids in Science and Technology. Tennessee: Middle Tennessee State University; 2011. p. 109–34.

[34] Ohno H. Electrochemical Aspects of Ionic Liquids. Ohno H, editor. Hoboken NJ: John Wiley & Sons, Inc.; 2005.

[35] Pandey G.P., Kumar Y., Hashmi S.A. Ionic liquid incorporated polymer electrolytes for supercapacitor application. Indian Journal of Chemistry 2010; 49A:743-751

[36] Taberna P, Simon P, Fauvarque J. Electrochemical characteristics and impedance spectroscipy studies of carbon-carbon supercapacitors. J. Electrochem. Soc. 2003;150(3):A292–300.

[37] Sakka M Al, Gualous H, Omar N. Batteries and Supercapacitors for Electric Vehicles. In: Stevic Z, editor. New Generation of Electric Vehicles. InTech; 2012. p. 135–65.

[38] De Levie R. On porous electrodes in electrolyte solutions - IV*. Electrochim. Acta. 1964;9:1231–45.

[39] Jang JH, Yoon S, Ka BH, Jung Y-H, Oh SM. Complex Capacitance Analysis on Leakage Current Appearing in Electric Double-layer Capacitor Carbon Electrode. J. Electrochem. Soc. 2005;152(7):A1418–22.

[40] Conway B. Electrochemical Supercapacitors Scientific Fundamentals and Technological Applications. New York: Kluwer Academic; 1996.

[41] Pekala R. Low density, resorcinol-formaldehyde aerogels. US patent 4873218; 1989. p. 8.

[42] Pekala R. Organic aerogels from the polycondensation of resorcinol with formaldehyde. J. Mater. Sci. 1989;24:3221–7.

[43] Pajonk G. Catalytic aerogels. Catalysis Today. 1997;35(3):319–37.

[44] Pierre A, Pajonk GM. Chemistry of aerogels and their applications. Chem. Rev. 2002;102(11):4243–65.

[45] Livage J, Sanchez C. Sol-gel chemistry. J Non-Cryst Solids. 1992;145:11–9.

[46] Gonzalez R, Lopez T, Gomez R. Sol—Gel preparation of supported metal catalysts. Catalysis Today. 1997;35(3):293–317.

[47] Pierre A. Introduction to Sol-Gel Processing. 2nd ed. Norwell: Kluwer Academic; 1998.

[48] Kabbour H, Baumann T, Satcher J, Saulnier A, Ahn C. Toward New Candidates for Hydrogen Storage: High Surface Area Carbon Aerogels. Chem. Mater. 2006;18:6085–7.

[49] Maldonado-Hódar FJ, Moreno-Castilla C, Carrasco-Marín F, Pérez-Cadenas AF. Reversible toluene adsorption on monolithic carbon aerogels. J. Hazard. Mater. 2007;148(3):548–52.

[50] Kadirvelu K, Goel J, Rajagopal C. Sorption of lead, mercury and cadmium ions in multi-component system using carbon aerogel as adsorbent. J. Hazard. Mater. 2008;153(1-2):502–7.

[51] Moreno-Castilla C, Maldonado-Hódar FJ. Carbon aerogels for catalysis applications: An overview. Carbon. 2005;43(3):455–65.

[52] Du H, Li B, Kang F, Fu R, Zeng Y. Carbon aerogel supported Pt–Ru catalysts for using as the anode of direct methanol fuel cells. Carbon. 2007;45(2):429–35.

[53] Maldonado-Hódar F, Moreno-Castilla C, Pérez-Cadenas A. Surface morphology, metal dispersion, and pore texture of transition metal-doped monolithic carbon aerogels and steam-activated derivatives. Micropor. Mesopor. Mater. 2004;69(1-2):119–25.

[54] Moreno-Castilla C, Maldonado-Hódar FJ, Rivera-Utrilla J, Rodríguz-Castellón E. Group 6 metal oxide-carbon aerogels . Their synthesis, characterization and catalytic activity in the skeletal isomerization of 1-butene. Applied Catalysis A. 1999;183:345–56.

[55] Padilla-Serrano M, Maldonado-Hódar F, Moreno-Castilla C. Influence of Pt particle size on catalytic combustion of xylenes on carbon aerogel-supported Pt catalysts. Applied Catalysis B. 2005;61(3-4):253–8.

[56] Forest L, Gibiat V, Woignier T. Biot's theory of acoustic propagation in porous media applied to aerogels and alcogels. J Non-Cryst Solids. 1998;225:287–92.

[57] Baetens R, Jelle BP, Gustavsen A. Aerogel insulation for building applications: A state-of-the-art review. Energy and Buildings. 2011;43(4):761–9.

[58] Wei G, Liu Y, Zhang X, Yu F, Du X. Thermal conductivities study on silica aerogel and its composite insulation materials. Int. J. Heat Mass Tran. 2011;54(11-12):2355–66.

[59] Hostler S, Abramson A, Gawryla M, Bandi S, Schiraldi D. Thermal conductivity of a clay-based aerogel. Int. J. Heat Mass Tran. 2009;52(3-4):665–9.

[60] Finlay K, Gawryla MD, Schiraldi DA. Biologically Based Fiber-Reinforced/Clay Aerogel Composites. Ind. Eng. Chem. Res. 2008;47(3):615–9.

[61] Sander MT. Ultra-thin prestressed fiber reinforced aerogel honeycomb catalyst monoliths. US patent 5972254; 1999.

[62] Nguyen BCN, Meador MAB, Medoro A, Arendt V, Randall J, McCorkle L, et al. Elastic behavior of methyltrimethoxysilane based aerogels reinforced with tri-isocyanate. ACS Applied Materials & Interfaces. 2010;2(5):1430–43.

[63] Smirnova A, Dong X, Hara H, Vasiliev A, Sammes N. Novel carbon aerogel-supported catalysts for PEM fuel cell application. Int. J. Hydrogen Energy. 2005;30(2):149–58.

[64] Petričević R, Glora M, Fricke J. Planar fibre reinforced carbon aerogels for application in PEM fuel cells. Carbon. 2001;39(6):857–67.

[65] Hwang S-W, Hyun S-H. Synthesis and characterization of tin oxide/carbon aerogel composite electrodes for electrochemical supercapacitors. J. Power Sources. 2007;172(1):451–9.

[66] Fang B, Binder L. A modified activated carbon aerogel for high-energy storage in electric double layer capacitors. J. Power Sources. 2006;163(1):616–22.

[67] Li J, Wang X, Huang Q, Gamboa S, Sebastian P. Studies on preparation and performances of carbon aerogel electrodes for the application of supercapacitor. J. Power Sources. 2006;158(1):784–8.

[68] Schmitt C, Pröbstle H, Fricke J. Carbon cloth-reinforced and activated aerogel films for supercapacitors. J Non-Cryst Solids. 2001;285:277–82.

[69] Czakkel O, Marthi K, Geissler E, László K. Influence of drying on the morphology of resorcinol–formaldehyde-based carbon gels. Micropor. Mesopor. Mater. 2005;86(1-3):124–33.

[70] Pekala R. Melamine-formaldehyde aerogels. US patent 5086085; 1992.

[71] Long D, Zhang J, Yang J, Hu Z, Cheng G, Liu X, et al. Chemical state of nitrogen in carbon aerogels issued from phenol–melamine–formaldehyde gels. Carbon. 2008;46(9):1259–62.

[72] Pekala R, Alviso C, Lu X, Gross J, Fricke J. New organic aerogels based upon a phenolic-furfural reaction. J Non-Cryst Solids. 1995;188:34–40.

[73] Wu D, Fu R. Synthesis of organic and carbon aerogels from phenol–furfural by two-step polymerization. Micropor. Mesopor. Mater. 2006;96(1-3):115–20.

[74] Long D, Zhang J, Yang J, Hu Z, Li T, Cheng G, et al. Preparation and microstructure control of carbon aerogels produced using m-cresol mediated sol-gel polymerization of phenol and furfural. New Carbon Materials. 2008;23(2):165–70.

[75] Scherdel C, Reichenauer G. Carbon xerogels synthesized via phenol–formaldehyde gels. Micropor. Mesopor. Mater. 2009;126(1-2):133–42.

[76] Al-Muhtaseb S, Ritter J. Preparation and Properties of Resorcinol-Formaldehyde Organic and Carbon Gels. Adv. Mater. 2003;15(2):101–14.

[77] Pekala R, Alviso C, LeMay J. Organic aerogels: microstructural dependence of mechanical properties in compression. J Non-Cryst Solids. 1990;125(1-2):67–75.

[78] Yamamoto T, Yoshida T, Suzuki T, Mukai SR, Tamon H. Dynamic and static light scattering study on the sol-gel transition of resorcinol-formaldehyde aqueous solution. J. Colloid Interface Sci. 2002;245(2):391–6.

[79] Fairén-Jiménez D, Carrasco-Marín F, Moreno-Castilla C. Inter- and intra-Primary-Particle Structure of Monolithic Carbon Aerogels Obtained with Varying Solvents. Langmuir. 2008;24:2820–5.

[80] Lin C, Ritter JA. Carbonization and activation of sol – gel derived carbon xerogels. Carbon. 2000;38:849–61.

[81] Tamon H, Ishizaka H, Mikami M, Okazaki M. Porous structure of organic and carbon aerogels synthesized by sol-gel polycondensation of resorcinol with formaldehyde. Carbon. 1997;35(6):791–6.

[82] Pekala RW, Alviso CT, Kong FM, Hulsey SS. Aerogels derived from multifunctional organic monomers. J Non-Cryst Solids. 1992;145:90–8.

[83] Elkhatat A, Al-Muhtaseb S. Advances in tailoring resorcinol-formaldehyde organic and carbon gels. Adv. Mater. 2011;23(26):2887–903.

[84] Czakkel O, Geissler E, Moussaïd A, Koczka B, László K. Copper-containing resorcinol–formaldehyde networks. Micropor. Mesopor. Mater. 2009;126(3):213–21.

[85] Reynolds G, Fung A, Wang Z, Dresselhaus M, Pekala R. The effects of external conditions on the internal structure of carbon aerogels. J Non-Cryst Solids. 1995;188(1-2):27–33.

[86] Calvo EG, Menéndez JÁ, Arenillas A. Designing Nanostructured Carbon Xerogels. In: Rahman MM, editor. Nanomaterials. InTech; 2011. p. 189–238.

[87] Wu D, Fu R, Zhang S, Dresselhaus MS, Dresselhaus G. Preparation of low-density carbon aerogels by ambient pressure drying. Carbon. 2004;42(10):2033–9.

[88] Li W, Lu A, Schu F. Preparation of monolithic carbon aerogels and investigation of their pore interconnectivity by a nanocasting pathway. Chem. Mater. 2005;17(15):3620–6.

[89] Job N, Pirard R, Marien J, Pirard J-P. Porous carbon xerogels with texture tailored by pH control during sol–gel process. Carbon. 2004;42(3):619–28.

[90] Zubizarreta L, Arenillas A, Pirard J-P, Pis JJ, Job N. Tailoring the textural properties of activated carbon xerogels by chemical activation with KOH. Micropor. Mesopor. Mater. 2008;115(3):480–90.

[91] Kappe CO, Stadler A. Microwave Theory. Microwaves in Organic and Medicinal Chemistry. Weinheim: WILEY-VCH Verlag GmbH & Co. KGaA; 2005. p. 9–29.

[92] Kang KY, Hong SJ, Lee BI, Lee JS. Enhanced electrochemical capacitance of nitrogen-doped carbon gels synthesized by microwave-assisted polymerization of resorcinol and formaldehyde. Electrochem. Commun. 2008;10(7):1105–8.

[93] Calvo E, Juárez-Pérez E, Menéndez J, Arenillas A. Fast microwave-assisted synthesis of tailored mesoporous carbon xerogels. J. Colloid Interface Sci. 2011;357(2):541–7.

[94] Tamon H, Ishizaka H, Yamamoto T, Suzuki T. Preparation of mesoporous carbon by freeze drying. Carbon. 1999;37(12):2049–55.

[95] Babić B, Kaluđerović B, Vračar L, Krstajić N. Characterization of carbon cryogel synthesized by sol–gel polycondensation and freeze-drying. Carbon. 2004;42(12-13):2617–24.

[96] Maldonado-Hódar F, Moreno-Castilla C, Rivera-Utrilla J. Catalytic Graphitization of Carbon Aerogels by Transition Metals. Langmuir. 2000;16(9):4367–73.

[97] Moreno-Castilla C. Colloidal and micro-carbon spheres derived from low-temperature polymerization reactions. Adv. Colloid Interface Sci. 2016;236:113-141.

[98] Slomkowski S, Alemán JV, Gilbert RG, Hess M, Horie K, Jones RG, Kubisa P, Meisel I, Mormann W, Penczek S, Stepto RFT. Terminology of polymers and polymerization processes in dispersed systems (IUPAC recommendations 2011). Pure Appl Chem 2011; 83:2229-2259.

[99] Myers D: Surfaces, Interfaces, and Colloids. Principles and Applications. 2nd Edition. Wiley, 1999.

[100] Ryoo R, Joo SH, Jun S. Solid state NMR studies of hydrogen bonding network formation of novolac type phenolic resin and poly(ethylene oxide) blend. J Phys Chem B 1999; 103:7743-7746.

[101] Rodríguez-Reinoso F. Carbón activado: Estructura, preparación y aplicaciones. Alicante, España; 1981.

[102] Rodríguez-Reinoso F. Activated carbon: Structure, preparation and applications. In: Marsh H, Heinz E, Rodríguez-Reinoso F, editors. Introduction to carbon technologies. Alicante: Universidad de Alicante; 1977. p. 35–101.

[103] Lillo-Ródenas M, Cazorla-Amorós D, Linares-Solano A. Understanding chemical reactions between carbons and NaOH and KOH an insight into the chemical activation mechanism. Carbon. 2003;41(2):267–75.

[104] Yang T, Lua AC. Characteristics of activated carbons prepared from pistachio-nut shells by physical activation. J. Colloid Interface Sci. 2003;267(2):408–17.

[105] Frackowiak E. Carbon materials for supercapacitor application. Phys. Chem. Chem. Phys. 2007;9(15):1774–85.

[106] Shukla A, Sampath S, Vijayamohanan K. Electrochemical supercapacitors: Energy storage beyond batteries. Current Science. 2000;79(12):1656–61.

[107] Mahata N, Pereira M, Suárez-García F, Martínez-Alonso A, Tascón J, Figueiredo J. Tuning of texture and surface chemistry of carbon xerogels. J. Colloid Interface Sci. 2008;324(1-2):150–5.

[108] Moreno-Castilla C, Ferro-García M, Joly J, Bautista-Toledo I, Carrasco-Marín F, Rivera-Utrilla J. Activated Carbon Surface Modifications by Nitric Acid, Hydrogen Peroxide, and Ammonium Peroxydisulfate Treatments. Langmuir. 1996;11(19):4386–92.

[109] Seredych M, Hulicova-Jurcakova D, Lu GQ, Bandosz TJ. Surface functional groups of carbons and the effects of their chemical character, density and accessibility to ions on electrochemical performance. Carbon. 2008;46(11):1475–88.

[110] Shen W, Li Z, Liu Y. Surface Chemical Functional Groups Modification of Porous Carbon. Recent Patents Chem. Eng. 2008;1(1):27–40.

[111] Gorgulho HF, Gonçalves F, Pereira MFR, Figueiredo JL. Synthesis and characterization of nitrogen-doped carbon xerogels. Carbon. 2009;47(8):2032–9.

[112] Chen XY, Chen C, Zhang ZJ, Xie DH, Deng X, Liu JW. Nitrogen-doped porous carbon for supercapacitor with long-term electrochemical stability. J. Power Sources. 2013;230:50–8.

[113] Pérez-Cadenas M, Moreno-Castilla C, Carrasco-Marín F, Pérez-Cadenas AF. Surface chemistry, porous texture, and morphology of N-doped carbon xerogels. Langmuir. 2009;25(1):466–70.

[114] Barbosa MB, Nascimento JP, Martelli PB, Furtado CA, Mohallem NDS, Gorgulho H. Electrochemical properties of carbon xerogel containing nitrogen in a carbon matrix. Micropor. Mesopor. Mater. 2012;162:24–30.

[115] Moreno-Castilla C, Dawidziuk MB, Carrasco-Marín F, Morallón E. Electrochemical performance of carbon gels with variable surface chemistry and physics. Carbon. 2012;50(9):3324–32.

[116] A.M. Abioye, F.N. Ani, Recent development in the production of activated carbon electrodes from agricultural waste biomass for supercapacitors: A review, Renew. Sustain. Energy Rev. 2015; 52:1282-1293.

[117] Q. Ma, Y. Yu, M. Sindoro, A.G. Fane, R. Wang, H. Zhang, Carbon-based functional materials derived from waste for water remediation and energy storage, Adv. Mater. 2017;37:1605361.

CAPÍTULO II

MATERIALES Y MÉTODOS EXPERIMENTALES

Los materiales usados fueron esferas y aerogeles de carbono y carbones activados, los cuales se sintetizaron mediante diferentes compuestos fenólicos, moldes de sílice y residuos lignocelulósicos los cuales están detallados en los siguientes Capítulos de esta tesis, así como los métodos de síntesis utilizados.

Los materiales obtenidos se caracterizaron para conocer su morfología, tamaño, química superficial, porosidad y área superficial. La morfología se estudió mediante microscopia electrónica de transmisión y barrido. El tamaño se estudió mediante dispersión dinámica de luz y microscopia electrónica de barrido.

La química superficial se estudió mediante análisis termogravimétrico para conocer el contenido en cenizas de los materiales lignocelulósicos y los carbones activados, análisis elemental y espectroscopia fotoelectrónica de rayos X. Estas dos últimas técnicas son complementarias, ya que la primera nos permite conocer la composición global y la segunda la composición de la superficie externa del sólido. Por lo que entre ambas se puede tener una idea de la distribución de los grupos funcionales en el sólido.

La porosidad y área superficial se estudiaron mediante las isotermas de adsorción de N_2 a -176 ºC y de CO_2 a 0 ºC. La ecuación de Dubinin-Raduskevich se aplicó a ambas isotermas para conocer el volumen y tamaño de los microporos. El volumen total de poros se obtuvo de la isoterma de adsorción de N_2 a una presión relativa de 0,95. El volumen de mesoporos se obtuvo de la diferencia entre el volumen total y el de microporos obtenidos con N_2. Cuando se obtuvieron isotermas tipo IV se aplicó el método BJH para la determinación de la distribución y el volumen de mesoporos. El área superficial se obtuvo mediante la aplicación de la ecuación de BET a las isotermas de adsorción de N_2. Los poros de mayores dimensiones, macro y mesoporos fueron caracterizados mediante porosimetría de mercurio.

La caracterización electroquímica se llevó a cabo usando células de dos y tres electrodos y H_2SO_4 1 M o KOH 6 M como electrolitos. Los electrodos de trabajo se prepararon a partir de una mezcla del material de carbón (90 % en peso) finamente dividido y politetrafluoroetileno (10 % en peso en agua). Esta mezcla se presionó a 3 bar sobre papel de grafito y se secó a 120 ºC. La célula de dos electrodos era un dispositivo simétrico que comprendía los dos electrodos y un separador de microfibra de vidrio poroso impregnado en el electrolito. La célula de tres electrodos estaba constituida por el electrodo de trabajo, el electrodo de referencia (Ag/AgCl) y el contra electrodo (una espiral de hilo de Pt).

Las medidas que se llevaron a cabo en las dos células fueron las siguientes: voltametría cíclica, carga-descarga galvanostática y espectroscopia de impedancia electroquímica. A partir de estas determinaciones se obtuvo la capacidad específica de los supercondensadores a distintas densidades de corriente, la energía almacenada y potencia suministrada, la resistencia en serie equivalente, la resistencia a la transferencia de carga interfacial y la estabilidad de los supercondensadores en función del tiempo de carga y descarga.

En los siguientes Capítulos de esta tesis se da una información más detallada de todos estos métodos experimentales.

CAPÍTULO III

CHAPTER III

SYNTHESIS AND CHARACTERIZATION OF SOLID POLYMER AND CARBON SPHERES DERIVED FROM AN EMULSION POLYMERIZATION REACTION OF DIFFERENT PHENOLIC COMPOUNDS WITH FORMALDEHYDE

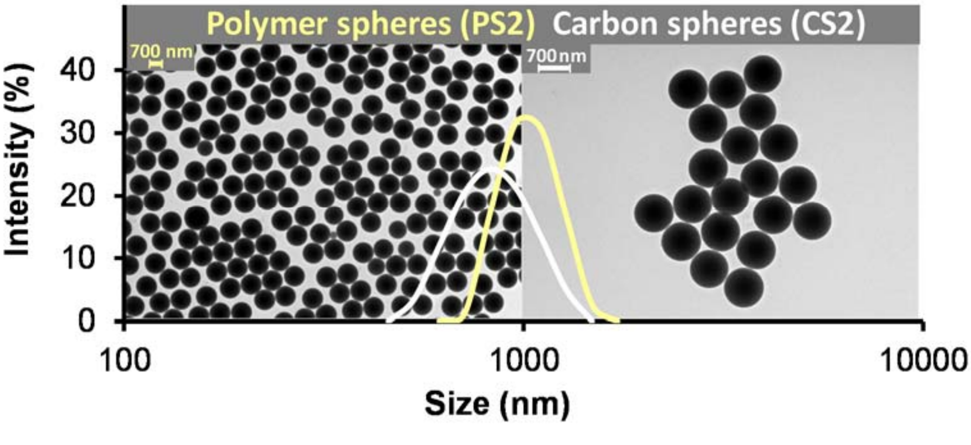

1. ABSTRACT

In this study, polymer spheres (PSs) were prepared by an emulsion polymerization of resorcinol, pyrocatechol, or 3-hydroxypyridine with formaldehyde under basic conditions. Carbon spheres (CSs) were obtained by carbonization of PSs at 900 ºC, and some of them were activated with KOH and oxygen adsorption-desorption cycles. Resorcinol and pyrocatechol differ in their reactivity during the polycondensation reaction with formaldehyde. The use of 3-hydroxypyridine allowed the introduction of N functionalities in the final CSs obtained. The objective was to examine the effects on the diameter of the carbon spheres, their surface physics and chemistry, and their performance as electrochemical double-layer (EDL) capacitors produced by: i) the replacement of resorcinol with pyrocatechol in the polymerization reaction and the utilization of different carbon sphere activation methods; and ii) the introduction of N functionalities. The size, surface area, micropore volume, total pore volume, and micropore width of the CSs ranged between 159 and 856 nm, 7 and 1156 $m^2 g^{-1}$, 0.06 and 0.46 $cm^3 g^{-1}$, 0.15 and 0.58 $cm^3 g^{-1}$, and 0.50 and 1.23 nm, respectively. The physically-activated sample showed the highest capacitance at 1 A g^{-1}, 200 F g^{-1} or 17.3 μF cm^{-2}. Capacitance was higher in N-doped samples than in the non-doped sample.

Keywords: Emulsion polymerization; Solid polymer spheres; Solid carbon spheres; Resorcinol; Pyrocatechol; 3-hydroxypyridine

2. INTRODUCTION

CSs have recently attracted considerable interest due to their new applications, mainly in energy storage and conversion but also in hard-templating, sorption/catalysis processes, and drug delivery systems [1]. This is attributable to their physico-chemical properties, including their tunable morphology (solid, hollow, or core-shell), size, surface area and porosity, good electrical conductivity, high packing density, enhanced mass transport, robust mechanical stability, low cytotoxicity, and excellent biocompatibility. Most of their applications require non-aggregated spheres with strict size control, narrow size distribution, smooth surface, and controlled surface chemistry [1,2].

CSs can be obtained using a wide variety of carbon precursors and methods. One of the most frequent approaches is the carbonization of PSs derived from low-temperature (below 250 ºC) polymerization reactions of reactive monomers and oligomers, which is well documented in the literature [1-3]. The different polymerization processes used for this purpose can be classified according to the formation mechanism of the PSs [1] as: emulsion polymerization, and its derivatives seeded emulsion and inverse emulsion polymerizations; precipitation polymerization, and its derivative dispersion polymerization; suspension polymerization; hard-templating; spray-drying; and hydrothermal or solvothermal treatment of carbohydrates and biomass in general.

In this study, PSs were prepared by an emulsion polymerization method [4] based on the Stöber process to prepare silica spheres [5]. The method used the polymerization reaction of resorcinol (R) and formaldehyde (F) in ethanol-water solution and in the presence of ammonia as polymerization and morphological catalyst, heating at 100 ºC in an autoclave [4]. Most carbon gels prepared by polymerization reactions use R and F mixtures, either in basic or acid medium, but there are scant data on the utilization of P [6]. The two phenolic compounds differ in their reactivity during the polymerization reaction, with R being much more reactive in comparison to P during polycondensation reaction with F under basic conditions. This is because of the electron donating and ortho- para-directing effects of the attached hydroxyl groups [7], leading2-, 4- and 6-positions of R to be doubly activated for the F addition by the two phenolic groups in meta-position, whereas the 3-and 4-positions in P are activated by one of the phenolic groups at the ortho-position and by the other at the 5- and 6-positions. Furthermore, the synthesis method employed to prepare the PSs [4] permits their doping with different elements and, in the present study, HP was used to introduce N functionalities in the final spheres obtained. The objective of this study was to examine the effects on the diameter of the CSs, their surface physics and chemistry, and their performance as EDL capacitors produced by: i) the replacement of R with P in the polymerization reaction and the utilization of different CSs activation methods; and ii) the introduction of N functionalities.

3. MATERIALS AND METHODS

3.1. PSs and CSs synthesis

PSs were prepared by the Liu et al. method [4] using different phenolic compounds (R, P, and HP) as carbon sources. These were polymerized in the presence of F and ammonia as both polymerization and morphological catalyst in a mixture of ethanol-water as solvent. Recipes are given in Table 1. Reactive solutions were introduced in a 250 mL Teflon-lined autoclave and heated at 100 ºC for 24 h. Next, the suspensions were centrifuged, and the residues (PSs) were washed and then immersed in acetone for three days to exchange the solvent, changing the acetone several times. Subsequently, the wet PSs were dried at room temperature overnight and then in a microwave oven under N_2 flow at 384 W for periods of 1 min until constant weight. Weight loss during microwave treatment was around 5 %. CSs were subsequently obtained by carbonization of PSs in N_2 flow (300 cm^3/min) at 900 ºC with a heating rate of 1.5 ºC min^{-1} and soaking time of 5 h.

Samples CS2, CS4, and CS5 were further chemically activated with KOH [8] to yield samples CS2-K, CS4-K, and CS5-K, respectively. For this purpose, the CSs were mixed with a concentrated KOH solution to yield a KOH/CSs weight ratio of 2. The slurry was dried at 60 ºC under an infrared lamp and pyrolyzed at 800 ºC in N_2 flow for 1 h at a heating rate of 1 ºC min^{-1}. Cooled samples were then treated with HCl solution and washed with distilled water until no chloride was present in the washing water.

Table 1. Recipes used to prepare the PSs in an ethanol (8 mL)-water (20 mL) solution

Sample	Phenolic compound (g)	Formaldehyde solution (mL)	NH_4OH solution 25 wt.% (mL)
PS1	0.1 R	0.14	0.10
PS2	0.2 R	0.28	0.20
PS3	0.1 P	0.14	0.10
PS4	0.2 P	0.28	0.20
PS5	0.3 P	0.42	0.30
PS6	0.15R+0.05HP	0.28	0.20
PS7	0.10R+0.10HP	0.28	0.20
PS8	0.05R+0.15HP	0.28	0.20

Sample CS2 was also physically activated by oxygen adsorption-desorption cycles [9]. For this purpose, the carbon was heated in Ar flow at 900 ºC for 2 h and was then cooled in Ar to 370 ºC, when Ar was replaced with an Ar-O_2 mixture (10 vol. % O_2). Reaction with air was carried out for 2 h at 370 ºC and then desorbed at 900 ºC in Ar flow. Following the oxidation step, the Ar-O_2 mixture was replaced with Ar and the sample was again heated to 900 ºC in order to desorb surface oxygen functionalities. The above cycle was repeated several times to yield a weight loss of *ca.* 20 %.

These mild activation conditions permit progressive enlargement of the microporosity [9]. Samples activated in this way are referred to as CS2-O hereafter.

3.2. Characterization methods

The morphology of the CSs was characterized by transmission electron microscopy (TEM) and high-resolution field-emission scanning electron microscopy (HRFESEM). TEM experiments were carried out with a Philips CM-20 microscope and HRFESEM micrographs were obtained with Carl Zeiss SMT Auriga equipment. Dynamic light scattering (DLS) was used to determine the hydrodynamic diameter distribution (HDD) and the mean diameter (d_{DLS}) of the PSs and CSs. DLS measurements were performed at 25 ºC using a Malvern Zetasizer NanoZS instrument (detection range: 0.6~600 nm) equipped with a 4 mW He-Ne laser (wavelength 633 nm) and avalanche photodiode detector. The selected measurement scattering angle was 173 º, using the non-invasive back-scatter (NIBS) technique. Surface area and pore texture were obtained from N_2 adsorption isotherms at -196 ºC determined with an Autosorb 1 from Quantachrome. Samples were previously outgassed overnight at 110 ºC under high vacuum (10^{-6} mbar). N_2 adsorption isotherms were analyzed by BET equation to measure the surface area, S_{BET}, and by Dubinin-Radushkevich (DR) equation to determine the micropore volume, W_0, and the mean width, L_0. The total pore volume, V_T, was taken as the volume of nitrogen adsorbed at a relative pressure of 0.95, while the mesopore volume, V_{meso}, was obtained from the difference between V_T and $W_0(N_2)$. The surface chemistry of samples was characterized by X-ray photoelectron spectroscopy (XPS) using an Escalab 200R system (VG Scientific Co.) equipped with MgK_α X-ray source ($h\upsilon$ = 1253.6 eV) and hemispherical electron analyzer. Survey and multi-region spectra were recorded at C_{1s}, N_{1s}, and O_{1s} photoelectron peaks. Each spectral region of photoelectron interest was scanned several times to obtain good signal-to-noise ratios. The C_{1s} peak at a binding energy (BE) of 284.6 eV was used as internal standard to obtain the number of components, position of peaks, and peak areas. The depth of the XPS analysis is around 2-3 nm; therefore, the O and N contents obtained, O_{XPS} and N_{XPS}, respectively, were the concentrations on the outermost surface of the materials.

The EDL capacitance of the CSs was evaluated in 1M H_2SO_4 using a two-electrode Teflon Swagelok-type cell and a Biologic VMP multichannel potentiostat. Electrodes were prepared from a well-mixed slurry of the CSs (90 wt. %) with PTFE as binder (10 wt. %). The slurry was pressed at 8 bar on graphite paper discs and dried in an oven at 120 ºC. The discs all had an area of 0.50 cm^2 and contained 5 mg of active material. Electrodes were immersed in an excess of the electrolyte solution for five days at room temperature before performing any measurement and were electrically isolated in the cell by a porous fibrous separator impregnated with the electrolyte solution

Cyclic voltammograms (CVs) were obtained at scan rates between 0.5 and 30 mV s^{-1}, and the gravimetric capacitance, C_{CV} (F/g), was calculated from these curves by the equation $C_{CV} = \sum I\Delta t / 2m\Delta V$, where $\sum I\Delta t$ is the area of the current (A) against time (s) curve, m the total mass of the active material in the two electrodes (g), and $\triangle V$the voltage window (V). Chronopotentiograms (CPs) were performed at current loading between 0.125 and 33 A/g in a voltage interval of 0-0.85 V. The gravimetric capacitance, C_{CP} (F/g), was obtained from the discharge curves of the CPs by equation $C_{CP} = I_d\Delta t / m\Delta V$, where I_d is the discharge current, Δt the discharge time, m the total mass of the active material in the two electrodes, and $\triangle V$ the voltage interval after the ohmic drop. In addition, the equivalent series resistance (ESR) was determined from the ohmic drop at the beginning of the discharge side of the CPs.

For performance comparisons, the gravimetric capacitances obtained from the above equations were multiplied by four to obtain the expression per single electrode, which is the three-electrode cell equivalent [10]. However, *per convention,* the gravimetric capacitances of two-electrode cells obtained from galvanostatic charge-discharge, $C_{CP(2E)}$, were used to calculate the energy density in the Ragone plot using the equation $E = C_{2EC}(\Delta V_d)^2 / 2$, where ΔV_d is the operation voltage taken as $\Delta V_d = V_{max} - IR_{drop}$. Power density was calculated from $P = E / \Delta t$ [11,12].

4. RESULTS AND DISCUSSION

HRFSEM images of PS2 and their physically and chemically activated CSs derivatives, CS2-O and CS2-K, respectively are shown, as an example, in Figure 1. They demonstrate that the spheres were uniform with a smooth surface, allowing them (PS2) to form ordered arrays. TEM images (Figure 2, and 3) confirm the spherical morphology of the PSs, some of which self-assembled into 2D hexagonal arrays on the carbon film of the grid during preparation of the TEM sample. These figures also show that the CSs obtained from the PSs preserved their spherical morphology. However, unlike some PSs samples, there was no tendency for them to form self-assembled arrays, probably attributable to the major loss of surface oxygen functionalities produced by the carbonization of PSs to obtain CSs.

HDDs of PSs and CSs are depicted in Figure 4, which shows that both types of samples were well dispersed. Table 2 exhibits the d_{DLS} values obtained, which ranged between 159 and 856 nm for the CSs according to the recipe and the activation treatment, as follows: i) an increase in the concentration of phenolic precursor (R or P), F, and ammonia in the solution augmented the diameter of both PSs and CSs, as previously reported with the use of R as phenolic compound [4]; ii) utilization of P (samples CS3 and CS4) instead of R (samples CS1 and CS2) produced a major decrease in d_{DLS} values, attributable to the higher reactivity of R than that of P in the polymerization reaction (*vide supra*), which would increase the size of the clusters formed; iii) d_{DLS} values were reduced by the carbonization of PSs, and this decrease was highly marked in some samples, although TEM images showed that they preserved their spherical shape. However, CSs activation produced virtually no change in their size or shape.

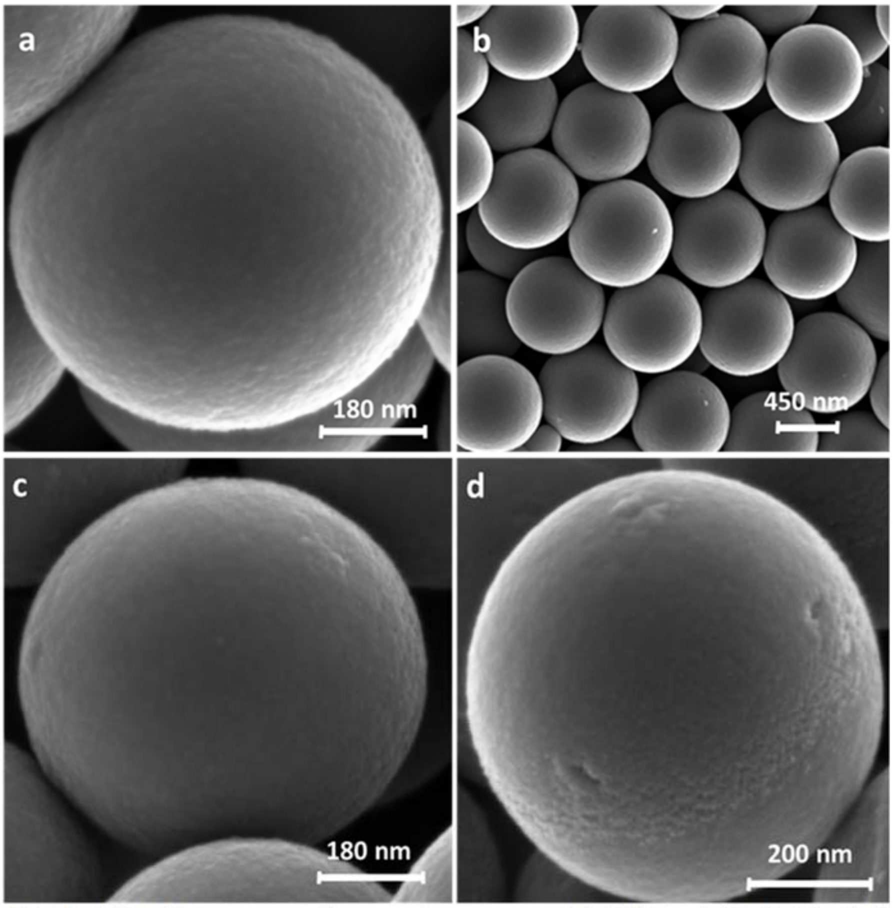

Figure 2. HRFSEM images of samples: a and b) PS2, c) CS2-O, d) CS2-K.

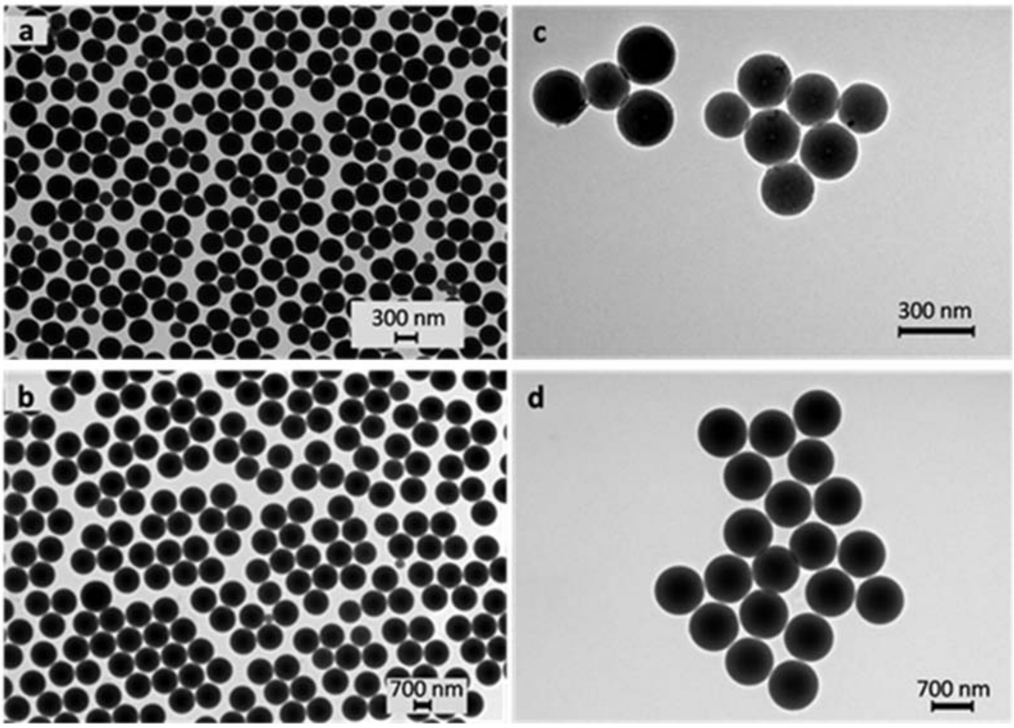

Figure 2. TEM images of samples: a) PS1, b) PS2, c) CS1, d) CS2

Samples CS6, CS7, and CS8 were prepared using the same recipe as for CS2 but replacing R with the same mass of R+HP. Therefore, the R/HP mass ratio was 3 for CS6, 1 for CS7, and 0.33 for CS8. Sample CS6, with the highest R/HP ratio, had a lower d_{DLS} value in comparison to CS2, but a decrease in the R/HP ratio in CS7 and CS8 brought the d_{DLS} value close to that of CS2.

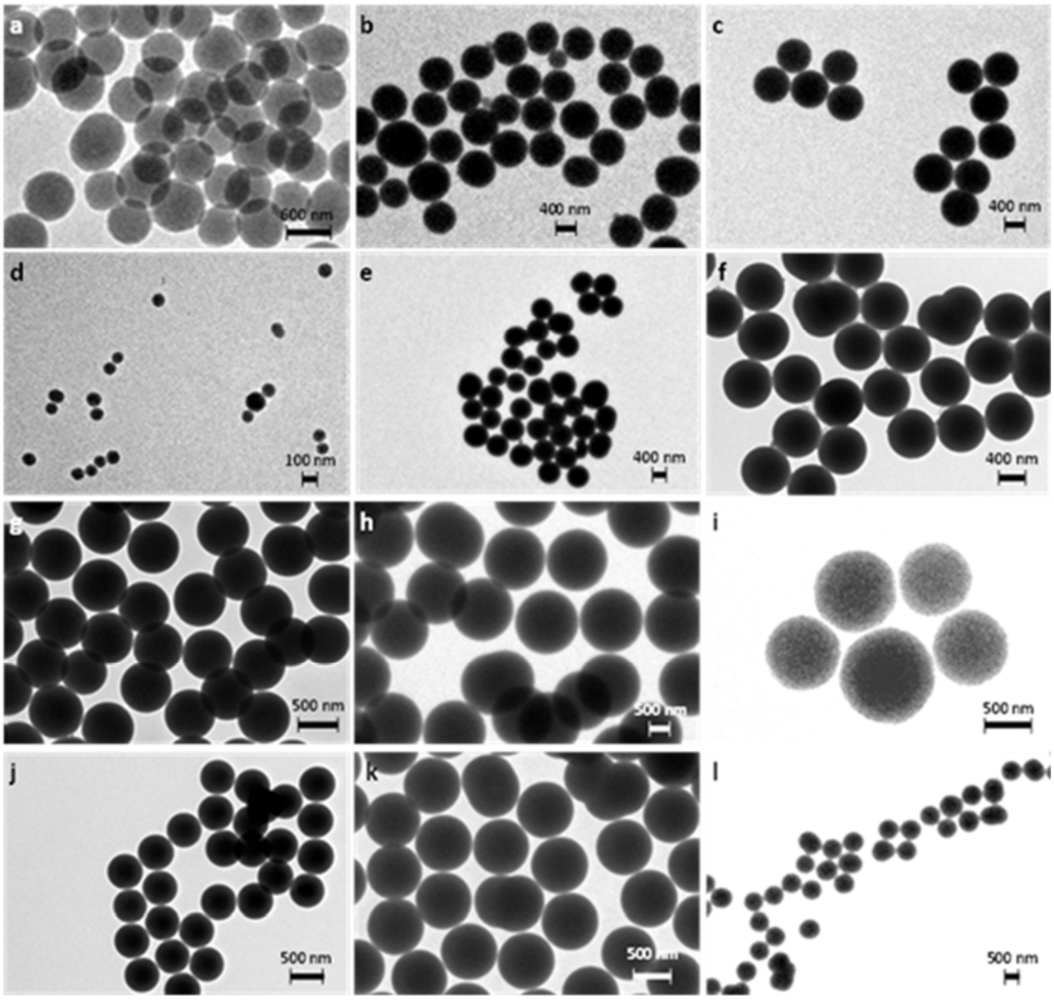

Figure 3. TEM images of samples: a) PS3, b) PS4, c) PS5, d) CS3, e) CS4, f) CS5, g) PS6, h) PS7, i) PS8, j) CS6, k) CS7, l) CS8.

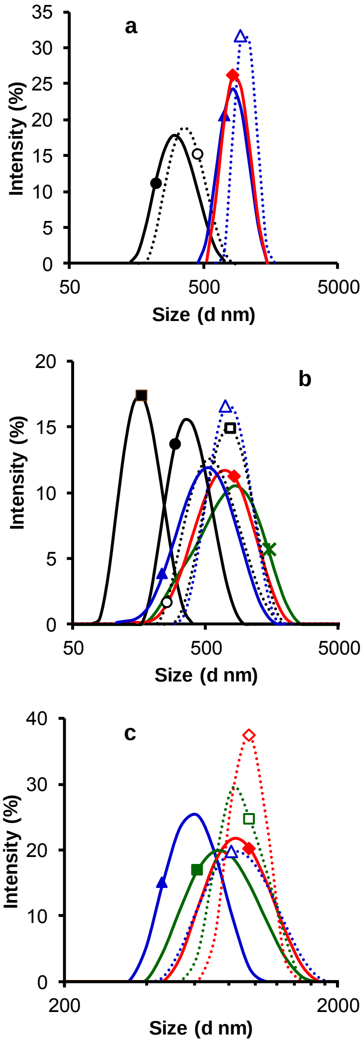

Figure 4. DLS plots of PSs (dotted lines) and CSs (solid lines). a) PS1 ○, PS2 △, CS1 ●, CS2 ▲and CS2-K ◆; b) PS3 □, PS4 ○, PS5 △, CS3 ■, CS4 ●, CS5 ▲, CS4-K ◆ and CS5-K ∗; c) PS6 △, PS7 ◇, PS8 □, CS6 ▲, CS7 ◆ and CS8 ■.

Table 2. Mean diameter of PSs and CSs and surface area and porosity of CSs

Sample	d_{DLS} nm	S_{BET} $m^2 g^{-1}$	W_0 $cm^3 g^{-1}$	L_0 nm	V_T $cm^3 g^{-1}$	V_{meso} $cm^3 g^{-1}$
CS1	312 (379)[a]	621	0.24	0.52	0.34	0.10
CS2	797 (1220)	579	0.23	0.51	0.27	0.04
CS2-K	856	1082	0.43	0.61	0.58	0.15
CS2-O	nd[b]	1156	0.46	0.80	0.50	0.04
CS3	159 (739)	531	0.20	0.79	0.38	0.18
CS4	381 (578)	158	0.06	1.23	0.15	0.09
CS5	468(734)	64	nd	nd	nd	nd
CS4-K	410	758	0.28	0.90	0.42	0.14
CS5-K	417	980	0.35	0.80	0.46	0.11
CS6	588 (827)	742	0.28	0.50	0.26	0.06
CS7	819 (1513)	660	0.26	0.50	0.37	0.11
CS8	780 (1325)	7	nd	nd	nd	nd

[a] In parentheses: d_{DLS} value of PSs. [b] nd: non-determined

Figure 5 depicts the N_2 adsorption isotherms on the CS samples, which were all type I except for samples CS5 and CS8. This is typical of microporous solids [13], although there was a slight increase in N_2 uptake with the rise in relative pressure after micropore filling, indicating the presence of mesopores below 4 nm in size. All isotherms also showed a large increase in the amount adsorbed at relative pressures above 0.95, due to N_2 condensation within void spaces left in the CS packing. Samples CS5 and CS8 showed type II adsorption isotherms typical of non-porous or macroporous samples [13]. Results of applying the BET and DR equations are compiled in Table 2.

S_{BET}, W_0, and L_0 values were very similar between samples CS1 and CS2, prepared using R as carbon source, but V_{meso} was higher in CS1 than in CS2. A major increase in S_{BET}, W_0, and L_0 values was produced by activation of CS2 to yield CS2-K and CS2-O. The method of activation had virtually no influence on S_{BET} or W_0 values, whereas L_0 was wider after oxygen adsorption-desorption cycles, because this mild activation method widens micropores progressively and more gently and homogeneously in comparison to KOH [9]. Finally, an increase in V_{meso} was only observed with KOH activation.

The O_{XPS} content of CS2, CS2-K, and CS2-O was 3.0, 10.4, and 4.4 at. %, respectively, reflecting the striking increase in oxygen content introduced by KOH activation. The O_{1s} core level spectrum (not shown) had two components in all samples, the first at BE between 531.0 and 531.6 eV, assigned to double C=O bonds in ketone, quinone, and carboxyl acid groups, and the second at BE between 532.3 and 533.3 eV, assigned to C–O bonds from alcohols, phenols, and ethers [14,15].

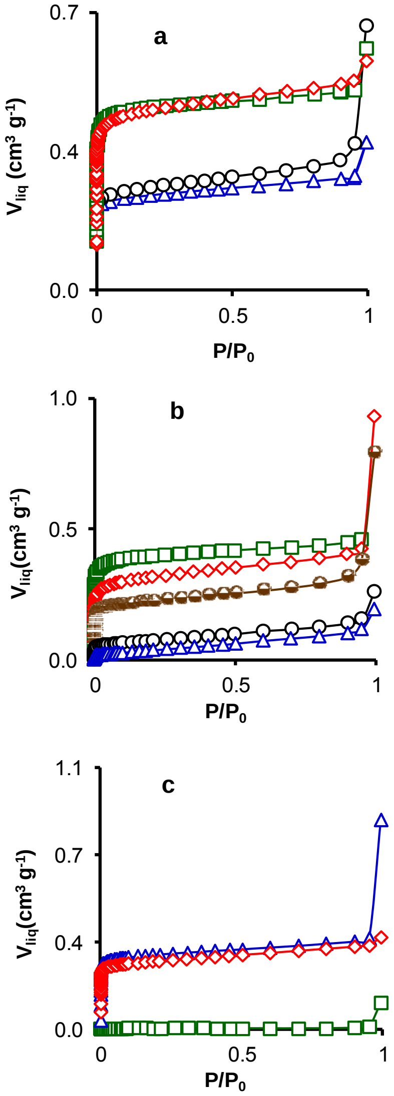

Figure 5. N_2 adsorption isotherms at -196 ºC on samples a) CS1 ○, CS2 △, CS2-K ◇ and CS2-O □; b) CS3 ◒, CS4 ○, CS5 △, CS4-K ◇ and CS5-K □; c) CS6 △, CS7 ◇ and CS8 □.

P was used as carbon source instead of R in samples CS3, CS4, and CS5. The recipes of CS3 and CS4 were comparable to those of CS1 and CS2, respectively (Table 1). The replacement of R with P produced a decrease in S_{BET} and W_0 and a widening of L_0, especially in the case of CS4, and there was also a marked reduction in these values at higher concentrations of P and F (sample CS5). These changes are likely induced by the differences in reactivity between these phenolic compounds. A large increase in S_{BET} and pore volume resulted from KOH activation to yield CS4-K and CS5-K, and this increase was higher in CS5-K.

Samples CS6 to CS8 can be compared with CS2, as indicated above. CS6, with the highest R/HP mass ratio, showed higher S_{BET} and W_0 values than for sample CS2. However, a decrease in the R/HP mass ratio progressively diminished these values until a non-porous carbon, CS8, was obtained.

The N_{1s} core level spectra of PS6, PS7, CS6, and CS7 are depicted in Figure 6. The fitting of the peaks showed the presence of various contributions with BEs that are displayed in Table 3 together with their corresponding percentages.

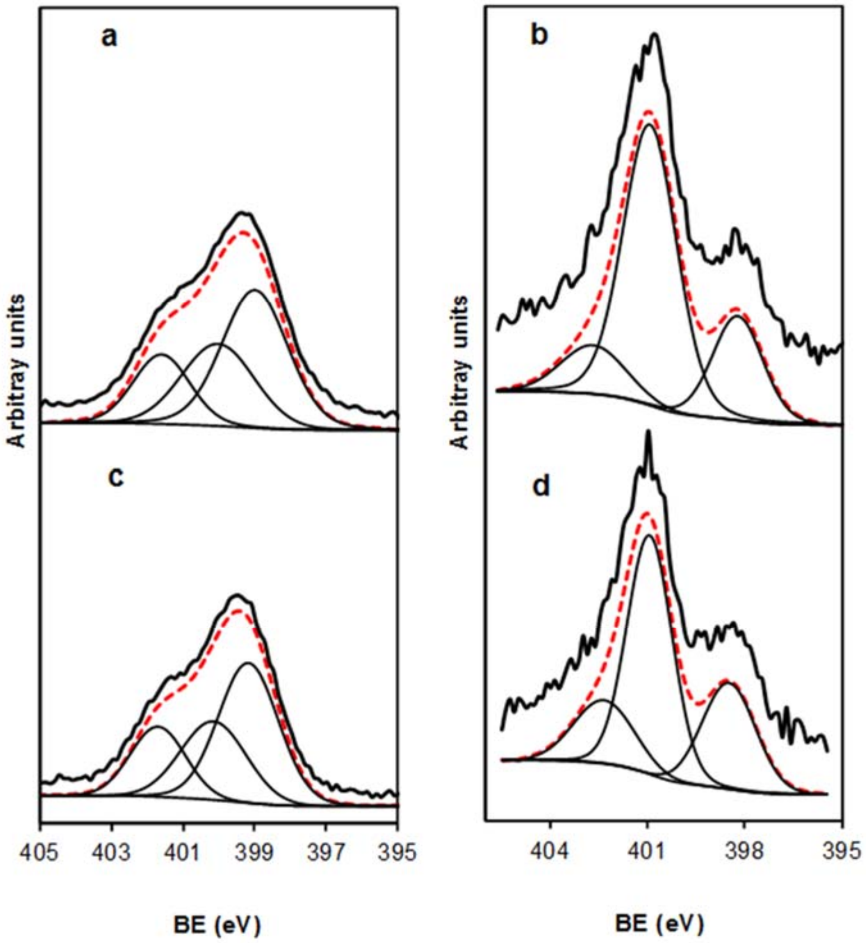

Figure 6. N_{1s} core-level spectra of samples: a) PS6, b) CS6, c) PS7 and d) CS7.

Table 3. Contribution to N_{1s} peak in XPS patterns of N-doped PSs and CSs. Nitrogen and oxygen contents

Sample	BE (eV) and area of the peak (%)			N_{XPS} (at. %)	O_{XPS} (at. %)
PS6	399.2(49)	400.1(29)	401.7(22)	5.3	19.6
PS7	399.2(50)	400.0(30)	401.6(21)	5.9	18.7
CS2	---	---	---	0	3.0
CS6	398.5(27)	401.0(54)	402.6(18)	1.4	2.6
CS7	398.2(22)	401.1(65)	402.7(13)	1.6	3.0

The polymer spheres PS6 and PS7 showed three peaks at around 399.2, 400.1, and 401.7 eV. The first peak at 399.2 eV can be assigned to substituted pyridines at the 2-, 4- or 6-positions of the aromatic ring [16-18]. These pyridine derivatives would result from the attack of formaldehyde against the above positions of 3-hydroxypyridine, producing its hydroxymethylene derivatives. The second peak at 400.1 eV can be assigned to pyrrolic-N or pyridonic-N, N-5 functionalities [19]. However, the N-5 peak in both samples were likely due solely to pyridonic-N functionalities because they had sufficient oxygen content (Table 3) to form these functionalities, which would require one N atom per one O atom with a single C-O bond (phenolic functionality). Furthermore, 5-membered rings cannot be formed from pyridinic nitrogen compounds during polymerization. The third peak at 401.7 eV can be assigned to pyridinium due to the protonation of pyridinic-N (N-6 functionalities), because the polymer cannot contain N within or in a valley position of a graphene layer, i.e., quaternary-N (N-Q functionalities), which give the same BE [18,19]. This is because N-Q functionalities appear after the condensation of aromatic rings and would only arise after heat treatment of the polymer spheres [18]. Almost 50 % of the N functionalities in these samples were substituted pyridines at the 2-, 4- and 6-positions.

After PS carbonization, the CSs showed three peaks at around 398.5, 401.0, and 402.3 eV. The peak at 398.5 eV can be assigned to N-6 functionalities from the substituted pyridines that appeared at 399. 2 eV in the PSs. The second peak at 401.0 eV can be assigned to N-Q functionalities, which are the most abundant by peak area percentage (Table 3) because HP favors their formation during polymer gel carbonization [18]. Therefore, the pyridonic-N functionalities that appeared in the PSs were converted to N-6 and N-Q functionalities during the carbonization process to obtain CSs samples. Finally, the third peak at 402.3 eV can be assigned to pyridin-N-oxide (N-X functionalities), i.e., pyridinic N bonded to oxygen species [20,21]. These N-X functionalities are formed when pyridine functionalities on the external surface are exposed to atmospheric air [22].

N_{XPS} and O_{XPS} contents are displayed in Table 3. Carbonization yielded CSs with lower nitrogen and oxygen contents than their corresponding PSs, and these contents were slightly higher in CS7 than in CS6.

The heteroatoms and functional groups on carbon surfaces can significantly alter their performance as supercapacitors due to the introduction of pseudocapacitance effects and variations in electronic conductivity and surface wettability [11,23,24]. Electrochemical measurements in aqueous acid solutions show that quinone and hydroquinone groups originate pseudocapacitance through redox reactions. Moreover, carboxylic and other CO_2-evolving groups have an acid character and introduce electron-acceptor properties on the carbon surface that also contribute to the overall capacitance through pseudocapacitance interactions [25]. In addition, the polarity of the surface oxygen functionalities improves the wettability of the carbon surface by the electrolyte, facilitating EDL formation. However, this advantage can be offset by the binding of oxygen polar groups with water molecules, which produces water clusters on the carbon surface that hinder and retard migration of the electrolyte into the pores, thereby increasing ohmic resistance [23].

N-6 and N-5 functionalities at the edges of graphene layers enhance carbon basicity [26] through a strong π delocalization in graphene layers due to the electron-rich nature of these nitrogen sites. Therefore, protons from the electrolyte can be attracted to the electrode surface, giving rise to pseudocapacitive interactions [27]. Furthermore, N-Q functionalities are localized within the graphene layers and produce a major increase in the HOMO energy of the graphene sheet [28]. Because of this increased HOMO energy, graphene sheets with N-Q functionalities are more positively charged when used as anode material in supercapacitors, attracting more negatively-charged ions and increasing the capacitance.

The electrochemical performance of the CSs was studied in a two-electrode cell. CVs at 5 mV s^{-1} and CPs at 0.5 A g^{-1} are depicted in Figures 7a and b, respectively, and in Figure 8. The CVs had a quasi-rectangular shape and the CPs were triangular, indicating that these samples behaved as ideal EDL capacitors. C_{CV} decreased when the scan rate was increased between 0.5 and 30 mV s^{-1} (Figure 9). This is because ions could reach the internal and external surface of the porous electrodes at low scan rates, whereas part of the internal surface of the micropore walls was inaccessible at high scan rates, due to ion diffusion, [29].

The gravimetric and areal capacitances from CPs, C_{CP}, and A_{CP}, respectively, and the ESR values at 1 A g^{-1} are compiled in Table 4. A_{CP} was obtained by dividing the gravimetric capacitance by the BET surface area. The non-activated samples CS2 to CS5 had a low C_{CP} value but this was markedly increased by activation, attributable to increases in surface area and porosity; the CS2-O sample had the highest C_{CP} value, 200 F g^{-1} at 1 A g^{-1}.

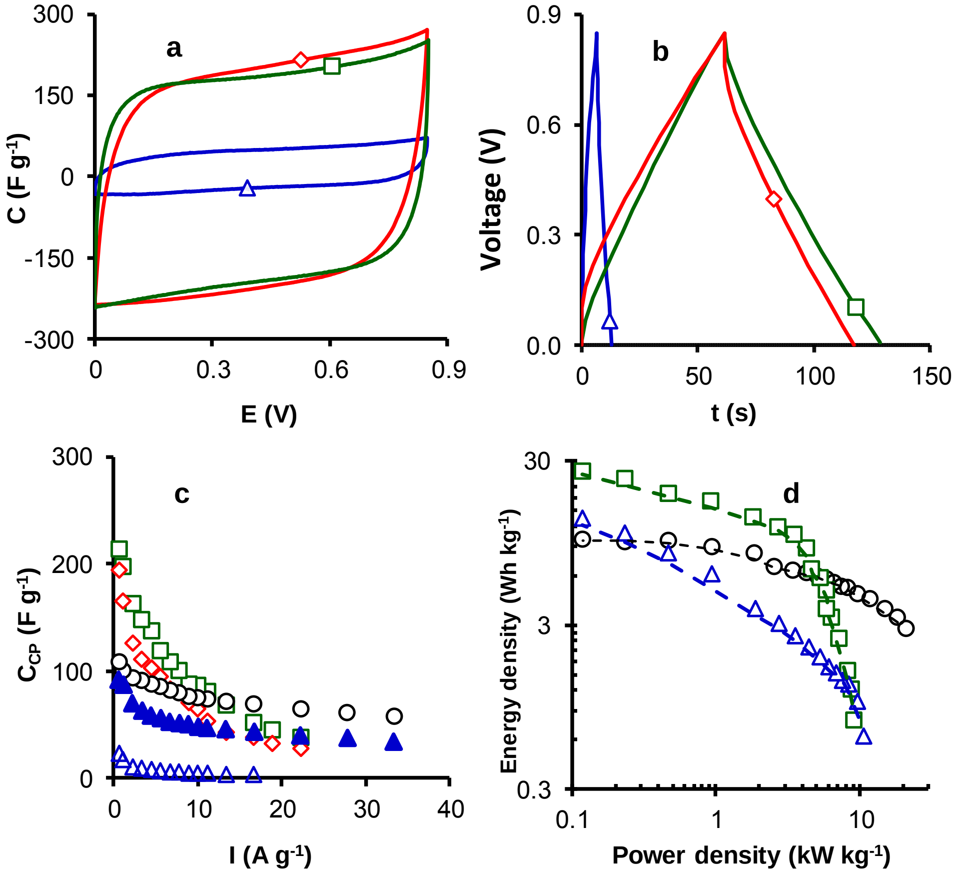

Figure 7. a) CVs a 5 mV s^{-1} of samples: CS2 △, CS2-K ◇ and CS2-O □; b) CPs at 0.5 A g^{-1} of samples: CS2 △, CS2-K ◇ and CS2-O □; c) C_{CP} variation *vs*. charge loading for samples: CS2 △, CS2-K ◇, CS2-O □, CS6 ○ and CS7▲; d) Ragone diagram of samples: CS2 △, CS2-O □ and CS6 ○.

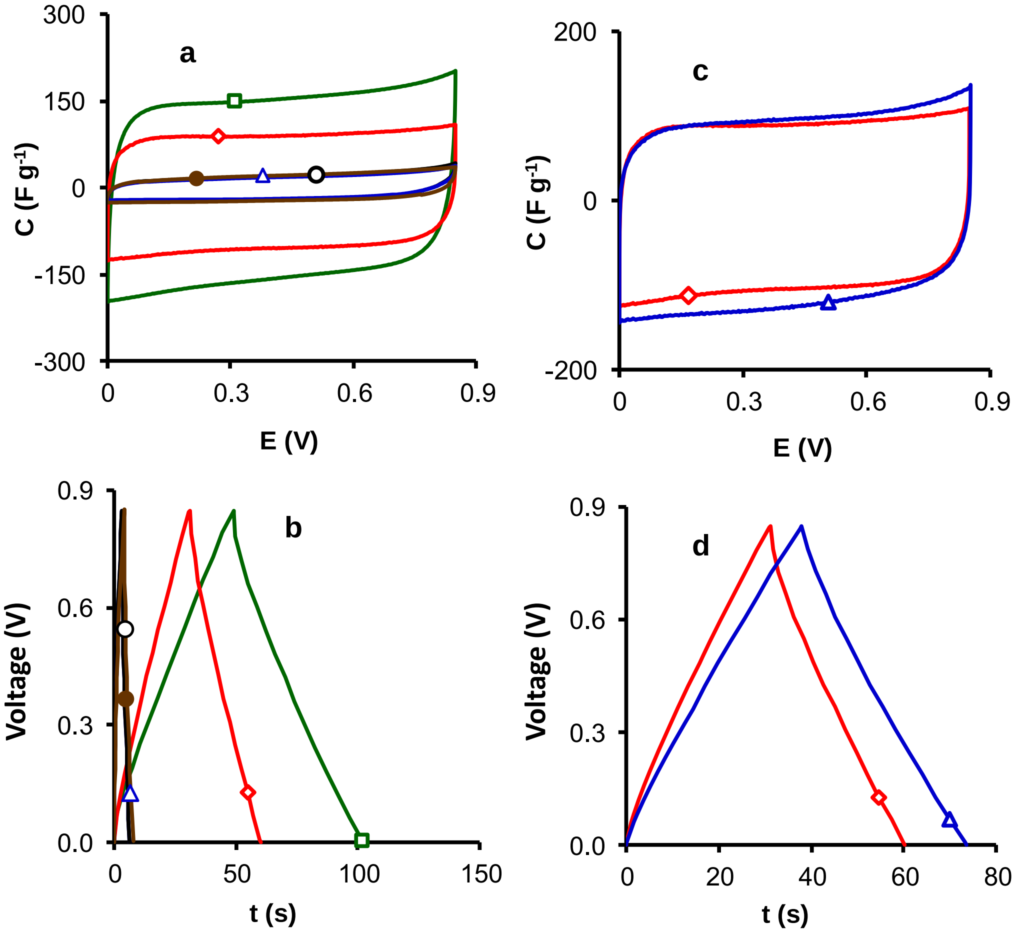

Figure 8. CVs at 5 mV s^{-1} (a) and CPs at 0.5 A g^{-1} (b) of samples: CS3 ●, CS4 ○, CS5 △, CS4-K ◇ and CS5-K □. CVs at 5 mV s^{-1} (c) and CPs at 0.5 A g^{-1} (d) of samples: CS6 △ and CS7 ◇.

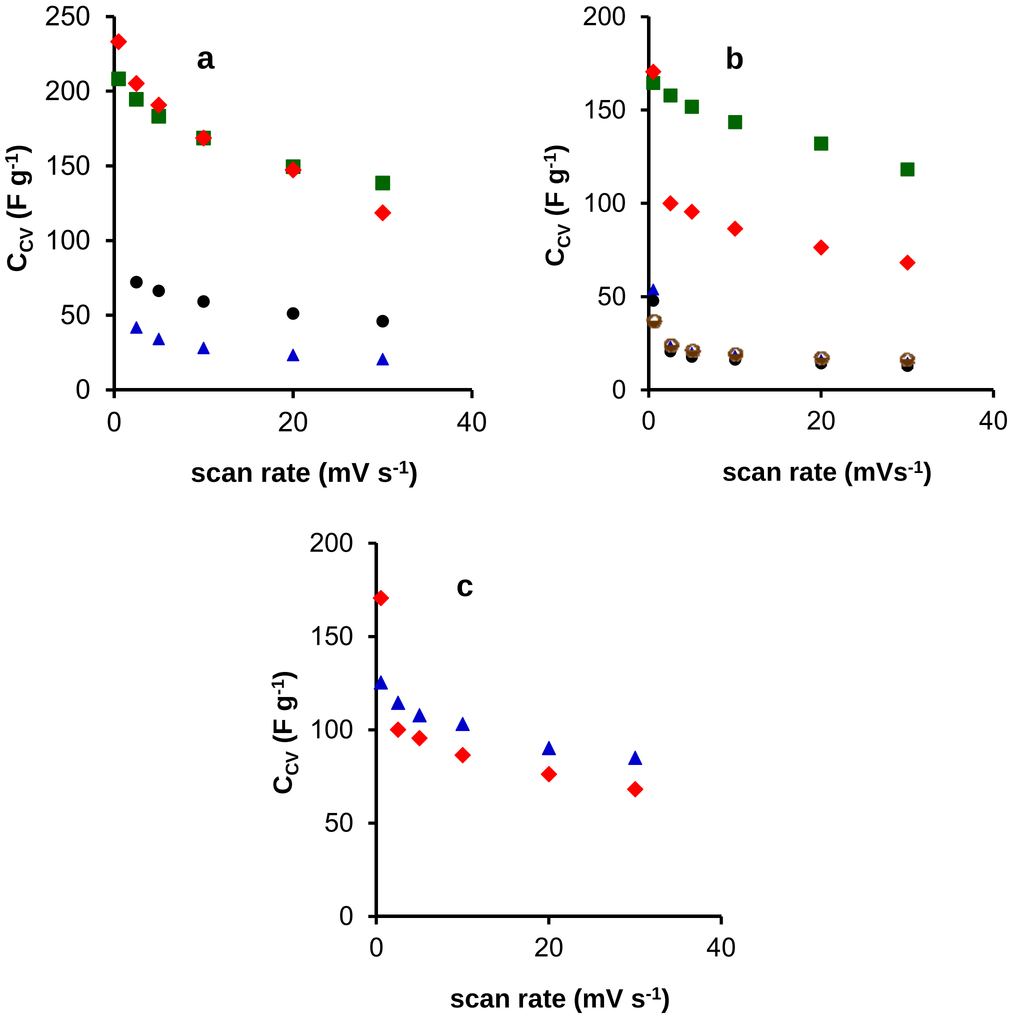

Figure 9. C_{CV} variation *vs.* scan rate for samples: a) CS1 ●, CS2 ▲, CS2-K ◆ and CS2-O ■; b) CS3 ◒, CS4 ●, CS5 ▲, CS4-K ◆ and CS5-K ■ and c) CS6 ▲ and CS7 ◆.

Table 4. Gravimetric (C_{CP}) and areal (A_{CP}) capacitances, and equivalent series resistance (ESR) from CPs at 1 A g^{-1}

Sample	C_{CP} F g^{-1}	A_{CP} μF cm^{-2}	ESR Ω
CS2	17	2.9	0.08
CS2-K	166	15.3	0.23
CS2-O	200	17.3	0.06
CS3	10	1.9	0.07
CS4	8	5.0	0.07
CS5	6	9.4	0.08
CS4-K	122	16.1	0.11
CS5-K	157	16.0	0.07
CS6	101	13.6	0.06
CS7	87	13.2	0.06

Unambiguous delineation of the relative importance of surface area and surface chemistry requires comparison of the areal capacitance of the CSs. Thus, A_{CP} was higher in CS2-O than in CS2-K because of the wider L_0 value (0.80 *vs.* 0.61 nm) and lower O_{XPS} content (4.4 *vs*. 10.4 at. %) of the former. Its wider L_0 value means that CS2-O would better accommodate the hydrated bisulfate anions (sized around 0.53 nm [30]) within the micropores for EDL formation. In addition, the higher O_{XPS} content of CS2-K would produce water clusters on the carbon surface, hindering ion mobility (*vide supra*) and decreasing the capacitance. Notably, the ESR value was much higher for CS2-K than for CS2-O, attributable to the lower ion mobility in the former. Both CS4-K and CS5-K showed similar A_{CP} value because they had larger L_0 values than CS2-K.

As to the N-doped samples, CS6 and CS7, they were compared with CS2 to determine the effects of N functionalities on the capacitance. A_{CP} values varied in the following order: CS6 = CS7 >> CS2, indicating that the presence of surface N functionalities increased the capacitance (*vide supra*). The similar A_{CP} of the two N-doped samples is explained by their highly similar N content.

CS2-O sample, as above indicated, showed the highest capacitance at 1 A g^{-1}, 200 F g^{-1} or 17.3 μF cm^{-2}. These values were compared with others reported in the literature (Table 5) for different CSs (mesoporous, micro- and mesoporous, hierarchically porous, hollow and N-doped). The gravimetric capacitance of CS2-O was similar or higher than reported for CSs at the same current density [24,31-35], whereas its areal capacitance was also similar or higher than other CSs [31-33,35,39]. It is noticeable that the micro- and mesoporous CSs [39] had a higher gravimetric capacitance than CS2-O but similar areal capacitance ~ 17 μF cm^{-2}.

The capacitance of CS2-O at 5 mV s^{-1} was 183 F g^{-1} or 15.8 μF cm^{-2}. The gravimetric capacitance was higher than that reported for CSs prepared by the same method as in the present study [4] except for the use of an ultrasound-mediated technique [40] instead of hydrothermal treatment, 33.5 F g^{-1} at 5 mV s^{-1} (Table 5). However, it was similar to the C_{CV} of the non-activated CS2 sample, 34 F g^{-1}, under the same experimental conditions. On the other hand, the C_{CV} of CS2-O was lower than reported for mesoporous CSs from hydrothermal treatment of glucose and KOH activation [41], 248 F g^{-1} at 5 mV s^{-1}, but the areal capacitance of these CSs was 14.8 μF cm^{-2}, lower than that of CS2-O.

Figure 7c shows that C_{CP} decreased when the current loading increased. Thus, when the loading increased from 1 to 22 A g^{-1} the capacitance retention decreased to 17 and 22 % for CS2-K and CS2-O, respectively. N-doped samples CS6 and CS7 showed capacitance retention at 33 A g^{-1} of 57 and 39 %, respectively, which was higher than did CS2-O and CS2-K. This behavior can be attributed to the pseudocapacitance effects introduced by N functionalities.

The energy and power characteristics of selected CSs are compared in the Ragone plot in Figure 7d. CS2-O showed a maximum energy density of 26.1 Wh kg^{-1} at a power density of 0.12 kW kg^{-1}, which decreased markedly to 0.8 Wh kg^{-1} at 9.9 kW kg^{-1}. Notably, CS6 exhibited a decrease in energy density from 9.9 to 2.9 Wh kg^{-1} when the power density was increased 175-fold from 0.12 to 21 kW kg^{-1}.

Table 5. Gravimetric and areal (in parentheses) capacitances at 1 A g^{-1} of carbon spheres from the literature

Carbon spheres	S_{BET} $m^2\ g^{-1}$	Capacitance F g^{-1} (µF cm^{-2})	Electrolyte	Ref.
Mesoporous CSs	1000	130 (13)	6M KOH	31
N-doped hollow CSs	213	176 (82.6)	6M KOH	24
Mesoporous CSs	1321	190 (14.4)	2M H_2SO_4	32
Mesoporous CSs	1280	196 (15.3)	5M H_2SO_4	33
CS2-O	1156	200 (17.3)	1M H_2SO_4	This work
N-doped hollow mesoporous CSs	718	206 (28.7)	6M KOH	34
N-doped mesoporous CSs	1330	211 (15.9)	5M H_2SO_4	35
Hierarchical porous CSs	1141	230 (20.2)	1M H_2SO_4	36
N-doped hollow CSs	753	260 (34.5)	2M H_2SO_4	37
N-doped microporous CSs	1280	270 (21.1)	1M H_2SO_4	38
Micro and mesoporous CSs	1620	276 (17)	6M KOH	39
CSs	953	33.5 (3.5) *	1M H_2SO_4	40
CS2-O	1156	183 (15.8) *	1M H_2SO_4	This work
Mesoporous CSs	1676	248 (14.8) *	0.5M H_2SO_4	41

* Capacitances at 5 mV s^{-1}

5. CONCLUSIONS

In summary, the present results demonstrated that the diameter, surface area and porosity of the CSs depended on the type of phenolic compound used and the activation treatment. Thus, the replacement of R with P produced changes in these characteristics due to differences in the reactivity of R and P with F in the polycondensation reaction. Activation of the CSs increased their surface area and porosity while having little effect on their size. The use of R and HP mixtures introduced surface N functionalities on the CSs and their surface characteristics depended on the R/HP mass ratio. Both chemical activation with KOH and physical activation by oxygen adsorption-desorption cycles (up to 20 % activation) produced activated CSs with similar surface area and micropore volume, but the latter treatment yielded wider micropores.

CS2-O sample showed the highest capacitance at 1 A g^{-1}, 200 F g^{-1} or 17.3 µF cm^{-2}, attributable to its wide microporosity (0.80 nm) and low O_{XPS} content (4.4 at.%). The areal capacitance was higher in N-doped CSs than in the non-doped sample due to pseudocapacitance effects introduced by surface N functionalities. One of these samples, CS6, had the highest capacitance retention between 1 and 33 A g^{-1}, 57 %, and its Ragone plot also showed a good electrochemical performance.

6. REFERENCES

[1] C. Moreno-Castilla, Colloidal and micro-carbon spheres derived from low-temperature polymerization reactions, Adv. Colloid Interface Sci. 236 (2016) 113-141.

[2] A.A. Deshmukh, S.D. Mhlanga, N.J. Coville, Carbon spheres, Mat. Sci. Eng. R. 70 (1-2) (2010) 1-28.

[3] M. Inagaki, C-R. Park, J.M. Skowronski, A.W. Morawski, Glass like carbon spheres – Activation, porosity and application possibilities, Adsorpt. Sci. Technol. 26 (9) (2008) 735-787.

[4] J. Liu, S.Z. Qiao, H. Liu, J. Chen, A. Orpe, D. Zhao, et al., Extension of the Stöber method to the preparation of monodisperse resorcinol-formaldehyde resin polymer and carbon spheres, Angew. Chem. Int. Ed. 50 (26) (2011) 5947-5951.

[5] W. Stöber, A. Fink, E.J. Bohn, Controlled growth of monodisperse silica spheres in the micron size range, J. Colloid. Interface Sci. 26 (1) (1968) 62-69.

[6] C. Moreno-Castilla, M.B. Dawidziuk, F. Carrasco-Marín, Z. Zapata-Benabithe, Surface characteristics and electrochemical capacitances of carbon aerogels obtained from resorcinol and pyrocatechol using boric and oxalic acids as polymerization catalysts, Carbon 49 (12) (2011) 3808-3819.

[7] R.W. Pekala, C.T. Alviso, F.M. Kong, S.S. Hulsey, Aerogels derived from multifunctional organic monomers, J. Non-Crystalline Solids145 (1992) 90-98.

[8] C. Falco, J.P. Marco-Lozar, D. Salinas-Torres, E. Morallón, D. Cazorla-Amorós, M.M. Titirici, et al., Tailoring the porosity of chemically activated hydrothermal carbons: Influence of the precursor and hydrothermal carbonization temperature, Carbon 62 (2013) 346-355.

[9] O.P. Mahajan, C. Moreno-Castilla, P.L. Walker Jr, Surface-treated activated carbon for removal of phenol from water, Sep. Sci. Technol. 15 (10) (1980) 1733-1752.

[10] T.E. Rufford, D. Hulicova-Jurcakova, E. Fiset, Z. Zhu, G.Q. Lu, Double-layer capacitance of waste coffee ground activated carbons in an organic electrolyte, Electrochem. Commun. 11 (5) (2009) 974-977.

[11] G.A. Ferrero, A.B. Fuertes, M. Sevilla, N-doped microporous carbon microspheres for high volumetric performance supercapacitors, Electrochim. Acta 168 (2015) 320-329.

[12] T. Liang, C. Chen, X. Li, J. Zhang, Popcorn-derived porous carbon for energy storage and CO_2 capture, Langmuir 32 (32) (2016) 8042-8049.

[13] M. Thommes, K. Kaneko, A.V. Neimark, J.P. Olivier, F. Rodríguez-Reinoso, J. Rouquerol, et al., Physisorption of gases, with special reference to the evaluation of surface area and pore size distribution

(IUPAC technical report) Pure Appl. Chem. 87 (9-10) (2015) 1051-1069.

[14] M. Seredych, D. Hulicova-Jurcakova, G.Q. Lu, T.J. Bandosz, Surface functional groups of carbons and the effects of their chemical character, density and accessibility to ions on electrochemical performance, Carbon 46 (11) (2008) 1475-1488.

[15] Z.W. He, J. Yang, Q.F. Lü, Q. Lin. Effect of Structure on the Electrochemical Performance of Nitrogen- and Oxygen-Containing Carbon Micro/Nanospheres Prepared from Lignin-Based Composites. ACS Sustainable Chem. Eng. 1 (3) (2013) 334-340.

[16] C.D. Wagner, X-Ray Photoelectron Spectroscopy Database. Version 1.0 NIST Standard Reference Database 20. National Institute of Standards and Technology: Gaithersburg, Md, USA, 1989.

[17] H. Schmiers, J. Friebel, P. Streubel, R. Hesse, R. Köpsel, Change of chemical bonding of nitrogen of polymeric N-heterocyclic compounds during pyrolysis, Carbon 37 (12) (1999) 1965-1978.

[18] M. Pérez-Cadenas, C. Moreno-Castilla, F. Carrasco-Marín, A. F. Pérez-Cadenas, Surface chemistry, porous texture, and morphology of N-doped carbon xerogels, Langmuir 25 (1) (2009) 466-470.

[19] J.R. Pels, F. Kapteijn, J.A. Moulijn, Q. Zhu, K.M. Thomas, Evolution of nitrogen functionalities in carbonaceous materials during pyrolysis, Carbon 33 (11) (1995) 1641-1653.

[20] D. Wang, M. Chen, C. Wang, J. Bai, J. Zheng, Synthesis of carbon microspheres from urea formaldehyde resin. Mater. Lett. 65 (7) (2011) 1069-1072.

[21] M. Wang, J. Fu, J. Zhu, Y. Yan, Q. Xu, Novel N-doped porous carbon microspheres containing oxygen and phosphorus for CO_2 absorbent and metal-free electrocatalysts, RSC Adv. 5 (36) (2015) 28080-28084.

[22] K.Y. Kang, B.I. Lee, J.S. Lee, Hydrogen adsorption on nitrogen-doped carbon xerogels, Carbon 47 (4) (2009) 1171-1180.

[23] Z. Zapata-Benabithe, F. Carrasco-Marín, C. Moreno-Castilla, Preparation, surface characteristics, and electrochemical double-layer capacitance of KOH-activated carbon aerogels and their O- and N-doped derivatives, J. Power Sources 219 (2012) 80-88.

[24] J. Han, G. Xu, B. Ding, J. Pan, H. Dou H, D.R. MacFarlane, Porous nitrogen-doped hollow carbon spheres derived from polyaniline for high performance supercapacitors, J. Mater. Chem. A 2 (15) (2014) 5352-5357.

[25] L. Zhao, L.Z. Fan, M.Q. Zhou, H. Guan, S. Qiao, M. Antonietti, et al., Nitrogen-containing hydrothermal carbons with superior performance in supercapacitors, Adv. Mater. 22 (45) (2010) 5202-5206.

[26] M. Koh, T. Nakajima, Adsorption of aromatic compounds on C_xN-coated activated carbon, Carbon 38 (14) (2000) 1947-1954.

[27] D. Hulicova, J. Yamashita, Y. Soneda, H. Hatori, M. Kodama, Supercapacitors prepared from melamine-based carbon, Chem. Mater. 17 (5) (2005) 1241-1247.

[28] Z.H. Zhu, H. Hatori, S.B. Wang, G.Q. Lu, Insights into hydrogen atom adsorption on and the electrochemical properties of nitrogen-substituted carbon materials, J. Phys. Chem. B 109 (35) (2005) 16744-16749.

[29] R. Kotz, M. Carlen, Principles and applications of electrochemical capacitors, Electrochim. Acta 45 (15-16) (2000) 2483-2498.

[30] C. Moreno-Castilla, M.B. Dawidziuk, F. Carrasco-Marín, E. Morallón, Electrochemical performance of carbon gels with variable surface chemistry and physics, Carbon 50 (9) (2012) 3324-3332.

[31] S. Chen, W. Shen, S. Zhang, Synthesis of spherical mesoporous carbon for electric double-layer capacitors, J. Sol-Gel Sci. Technol. 60 (2) (2011) 131-136.

[32] Q. Li, R. Jiang, Y. Dou, Z. Wu, T. Huang, D. Feng, J. Yang, A. Yu, D. Zhao, Synthesis of mesoporous carbon spheres with a hierarchical pore structure for the electrochemical double-layer capacitor, Carbon 49 (2011) 1248-1257.

[33] M.K. Seo, S. Yang, I.J. Kim, S.J. Park, Preparation and electrochemical characteristics of mesoporous carbon spheres for supercapacitors, Mater. Res. Bull. 45 (2010) 10-14.

[34] A. Chen, K. Xia, L. Zhang, Y. Yu, Y. Li, H. Sun, Y. Wang, Y. Li, S. Li, Fabrication of nitrogen-doped hollow mesoporous spherical carbon capsules for supercapacitors, Langmuir 32 (2016) 8934-8941.

[35] W. Li, D. Chen, Z. Li, Y. Shi, Y. Wan, J. Huang, J. Yang, D .Zhao, Z .Jiang, Nitrogen enriched mesoporous carbon spheres obtained by a facile method and its application for electrochemical capacitor, Electrochem. Commun. 9 (2007) 569-573.

[36] L. Jiang, Q. Cheng, Y. Xia, V. Pavlinek, P. Saha, C. Li, Effect of phenolic resin infiltration content on the structural and electrochemical properties of hierarchical porous carbons, J. Mater. Sci. 49 (2014) 7489-7496.

[37] F. Ma, H. Zhao, L. Sun, Q. Li, L. Huo, T. Xia, S. Gao, G. Pang, Z. Shi, S. Feng, A facile route for nitrogen-doped hollow graphitic carbon spheres with superior performance in supercapacitors, J. Mater. Chem. 22 (2012) 13464-13468.

[38] G.A. Ferrero, A.B. Fuertes, M. Sevilla, N-doped microporous carbon microspheres for high volumetric performance supercapacitors, Electrochim. Acta, 168, (2015) 320-329.

[39] X. Ma, M. Liu, L. Gan, Y. Zhao, L. Chen, Synthesis of micro- and mesoporous carbon spheres for supercapacitor electrode, J. Solid. State. Electrochem. 17 (2013) 2293-2301.

[40] V.G. Pol, L.K. Shrestha, K. Ariga, Tunable, functional carbon spheres derived from rapid synthesis of resorcinol-formaldehyde resins, ACS Appl. Mater. Interfaces 6 (13) (2014) 10649-10655.

[41] J. Chen, N. Xia, T. Zhou, S. Tan, F. Jiang, D. Yuan, Mesoporous carbon spheres: Synthesis, characterization and supercapacitance, Int. J. Electrochem. Sci. 4 (2009) 1063-1073.

CAPÍTULO IV

CHAPTER IV

HOLLOW AND SOLID CARBON SPHERES FROM OLIVE-MILL STORAGE WASTE USING A HARD-TEMPLATING METHOD

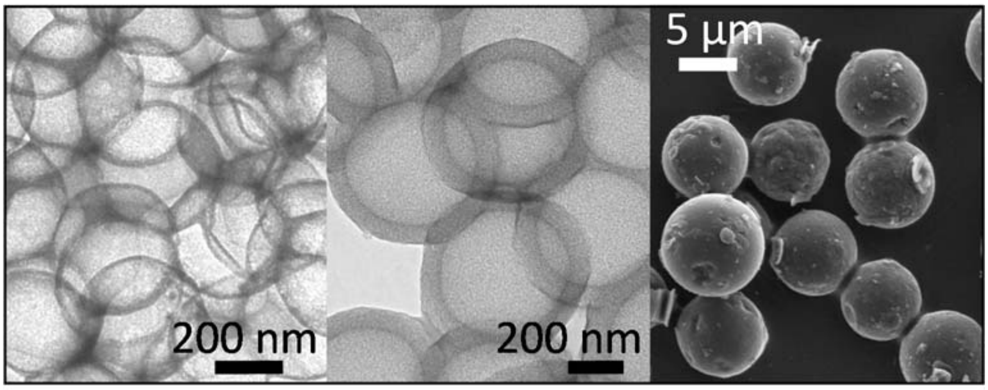

1. ABSTRACT

Hollow and solid carbon spheres (CSs) were prepared from olive-mill storage waste using solid core-mesoporous-shell (SCMS) and micro-mesoporous silica spheres as hard-template. Two hollow CSs were prepared with external diameter of 385 and 678 nm and shell width of 23 and 100 nm, respectively. Solid CSs had a diameter of 9 µm. Surface area, micropore volume, micropore width, total pore volume and mean mesopore width of the CSs ranged between 646-806 m^2 g^{-1}, 0.21-0.27 cm^3 g^{-1}, 1.3-1.6 nm, 0.47-1.81 cm^3 g^{-1}, and 3.1-3.7 nm, respectively. Electrochemical capacitance in 1 M H_2SO_4 ranged between 2.5 and 17.5 µF cm^{-2}

Keywords: Olive-mill waste; Hollow carbon spheres; Solid carbon spheres; Silica templates

2. INTRODUCTION

The olive oil industry is an important activity in Mediterranean countries, especially in Spain, which is the world's leading producer [1,2]. Today, this industry generates various types of waste that are rich in potentially useful compounds or can be converted into carbon materials [1,2]. Thus, in a previous study, our group used olive-mill waste water from the old three-phase olive-oil-extraction system to prepare activated carbon by chemical activation with KOH [3]. Another liquid waste obtained is the liquor exuded from the olive fruit storage hopper, which is rich in oligosaccharides, mannitol, triterpenes, phenolic compounds, and fatty residues.

3. MATERIALS AND METHODS

In the present investigation, the storage liquor (supplied by N.S. Asunción olive-oil mill, Noalejo, Jaén, Spain) was used as carbon source to prepare hollow and solid CSs after removal of the fatty compounds by n-hexane extraction. The dry matter content of the resulting solution was 13.4 %. This dry matter had an ash content of 7.6 % and its ultimate analysis was 41.8 % C, 5.7 % H, 0.5% N, and 44.4 % O (by difference).

CSs are now mainly employed in energy storage and conversion, sorption/catalysis processes, hard-templating, and drug-delivery systems

[4]. One of the most frequent methods to prepare hollow and solid CSs is to cover a spherical hard-template (e.g., silica) with carbon precursor, followed by polymerization and carbonization steps and subsequent removal of the template [4]. We utilized three types of silica sphere: SiO_2-A and SiO_2-B SCMS silica spheres, synthesized by the method reported by Büchel et al [5]; and commercial silica spheres, SiO_2-C, supplied by Thermo Fisher with chromatographic-grade and *ca*. 10 µm in diameter. SCMS silica spheres were prepared using absolute ethanol (1.91 mol), distilled water (0.83 mol), aqueous ammonia (37 wt. %, 0.17 mol), and tetraethoxysilane (TES, 27 mmol) distilled in vacuum immediately before use. After 1 h, a mixture of TES (22 mmol) and n-octadecyltrimethoxysilane (C18-TMS) at TES/C18-TMS molar ratio of 4.7was added drop by drop at 0.2 or 0.3 mL min^{-1} to obtain SiO_2-A or SiO_2-B, respectively. Samples were dried in an air-oven at 110 ºC for 24 h and then calcined at 500 ºC (1 ºC min^{-1}) for 6 h. CSs were synthesized in the following steps: i) impregnation of silica spheres by drop-wise addition of carbon precursor under infrared lamp (70 ºC), b) washing with ethanol and drying in air-oven at 110 ºC, c) carbonization at 840 ºC for 1 h in N_2 flow, and d) hard-template removal with HF. Henceforth, CSs are designated by replacing SiO_2 with the letter C in the name of the hard-template.

Hard-templates and CSs were characterized by TEM and N_2 adsorption-desorption isotherms at -196 ºC. The BET equation was applied to adsorption isotherms to measure the surface area, S_{BET}, while the DR equation was applied to determine the micropore volume, V_{micro}, and mean width, L_0. Non-local density functional theory (NLDFT) was applied to the adsorption branch of the isotherm to determine the total pore volume, V_{tot}, the pore size distribution, and the mean pore width, $\bar{D}$. Mesopore volume, V_{meso}, was obtained as (V_{tot} - V_{mic}). CSs were analyzed by cyclic voltammetry (CV) using a two-electrode cell and 1 M H_2SO_4 as electrolyte. Electrodes were prepared from a well-mixed slurry of CSs (90 wt. %) with PTFE as binder (10 wt. %). Capacitances were calculated per single electrode.

4. RESULTS AND DISCUSSION

Fig. 1a-d depicts TEM images of SiO_2-A and SiO_2-B silica templates and their corresponding CA and CB CSs, respectively. Both silica templates had a spherical shape and uniform size, with a core-shell morphology that is most evident in sample SiO_2-B (Fig. 1c) due to its thicker shell. Diameters of SiO_2-A, CA, SiO_2-B, and CB spheres were *ca.* 402, 385, 635, and 678 nm, respectively, with the diameter of the hollow CSs being similar to that of the templates used in their synthesis. The shell was thinner in CA (*ca.* 23 nm) than in CB (*ca.* 100 nm), consistent with the shell width of the corresponding templates revealed by TEM (Figs. 1b and d). Utilization of the SiO_2-C template yielded solid CSs, sample CC (TEM image in Fig.1e), with a diameter of *ca.* 9 µm from SEM images (Fig 1f).

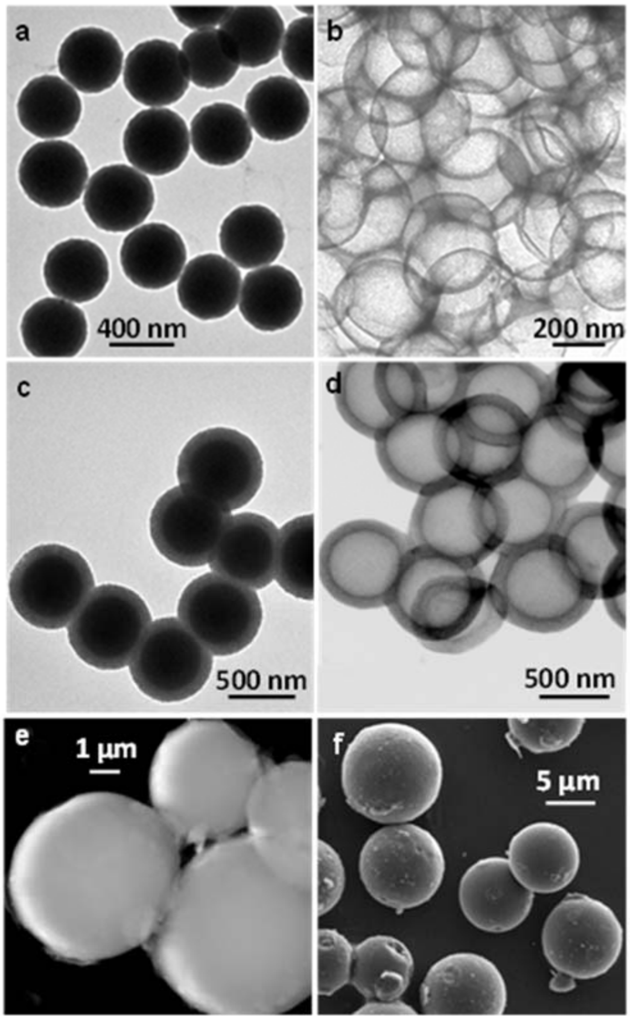

Figure 1. TEM images of a) SiO_2-A, b) CA c) SiO_2-B, d) CB and e) CC, and f) SEM image of CC

Fig 2 depicts N_2 adsorption-desorption isotherms at -196 ºC and pore size distributions, and Table 1 compiles the corresponding results.

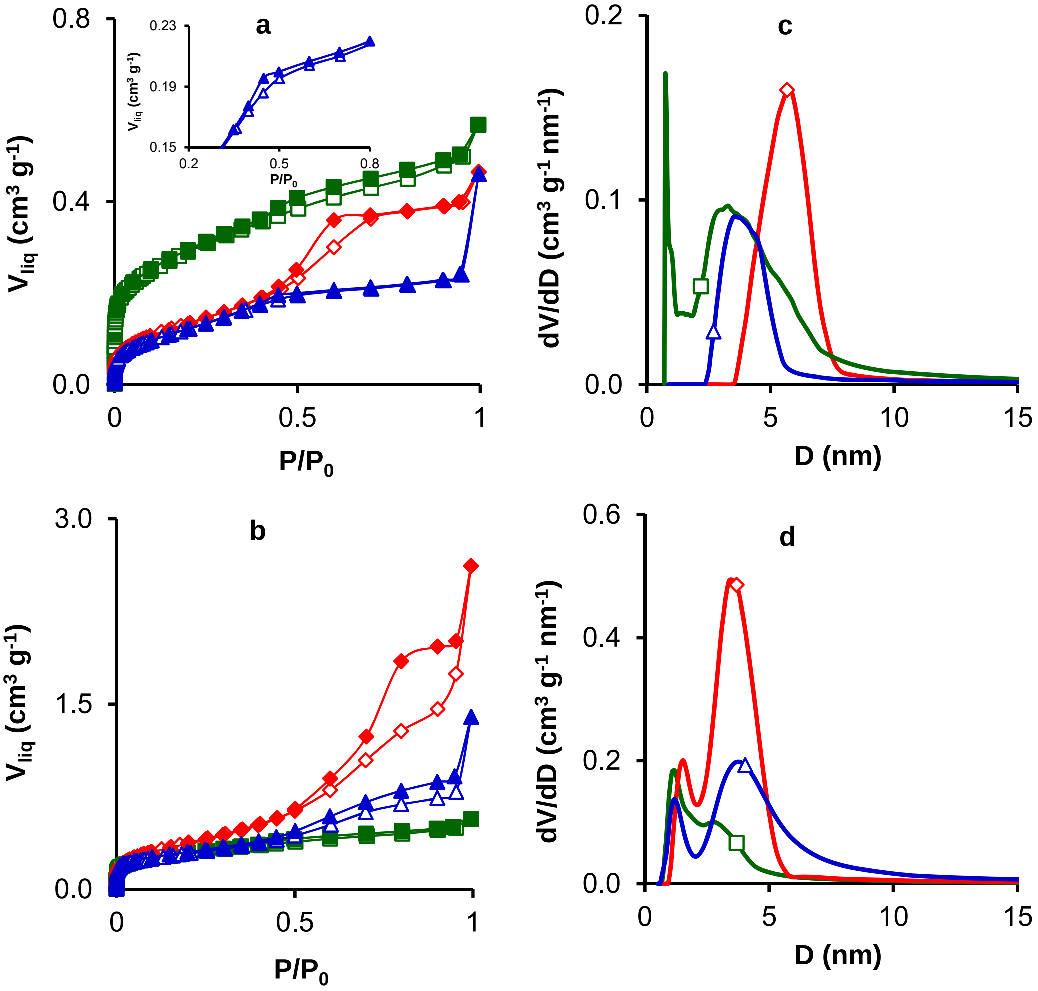

Figure 2. N_2 adsorption (open symbols)-desorption (closed symbols) isotherms on samples: a) SiO_2-A △, SiO_2-B ◇ and SiO_2-C □; b) CA △, CB ◇ and CC □. Pore size distributions of c) SiO_2-A △, SiO_2-B ◇ and SiO_2-C □; d) CA △, CB ◇ and CC □

Table 1. Surface area and pore texture of the silica templates and CSs. Areal capacitance (AC_{CV}) at 5 mV s^{-1} in 1 M H_2SO_4.

Sample	S_{BET}	V_{mic}	V_{meso}	V_{tot}	L_0	$\bar{D}$	AC_{CV}
	$m^2\ g^{-1}$	$cm^3\ g^{-1}$	$cm^3\ g^{-1}$	$cm^3\ g^{-1}$	nm	nm	μF cm^{-2}
SiO_2-A	258	0.09	0.14	0.23	1.7	3.5	
CA	650	0.27	0.60	0.87	1.5	1.3 - 3.7	2.5
SiO_2-B	278	0.09	0.29	0.38	1.7	5.7	
CB	806	0.27	1.54	1.81	1.6	1.5 - 3.4	8.2
SiO_2-C	655	0.21	0.27	0.48	1.3	0.7 - 3.4	
CC	646	0.21	0.26	0.47	1.3	1.1 - 3.1	17.5

The adsorption-desorption isotherms of the SCMS templates can be classified [6] as type IV with a hysteresis cycle of type H2, although the SiO_2-A template showed a very small hysteresis cycle (see inset in Fig. 2a), in accordance with its very thin shell (Fig. 1a). The SiO_2-C template had an adsorption branch that was a composite of type I and II with a type H4 hysteresis cycle. CSs samples CA and CB had the same type of isotherm and hysteresis cycle as their corresponding SCMS templates, with the exception of a more developed hysteresis cycle in CA than in its template. Sample CC also has the same type of isotherm as its template, typical of micro-mesoporous carbons.

The two SCMS templates had very similar or identical S_{BET}, V_{mic} and L_0 values, but V_{meso} and V_{tot} values were higher in SiO_2-B than in SiO_2-A due to the thicker shell of the former. With the exception of L_0, which remained practically unchanged, all of these values increased in the CSs derived from the templates. There was a markedly greater increase in S_{BET}, V_{meso} and V_{tot} values for CB than for CA. Although V_{mic} values were identical (0.27 cm^3 g^{-1}) in the two samples, the higher S_{BET} of CB indicated a greater contribution of its mesoporosity to the surface area in comparison to CA. In contrast, S_{BET}, V_{mic}, V_{meso}, V_{tot} and L_0 values were highly similar between the SiO_2-C template and the CC CSs. Both SCMS templates displayed a unimodal pore size distribution (Fig. 2c), with a wider mean mesopore width (5.7 nm) in CB than in CA (3.5 nm). However, the corresponding CSs (Fig. 2d) showed a bimodal pore size distribution with highly similar $\overline{D}$ values in the micro-mesopore range. In contrast, both SiO_2-C and CC showed a bimodal pore size distribution, with a slightly smaller mean pore width in CC than in the other CSs.

Figure 3 depicts the CVs at 5mV s^{-1} and Table 1 exhibits the corresponding AC_{CV} values, which increased in the order CA < CB < CC.

5. CONCLUSIONS

This study demonstrates that hollow and solid CSs with different shell widths and diameters, surface areas and pore textures can be synthesized using a low-cost carbon precursor from the olive-oil industry.

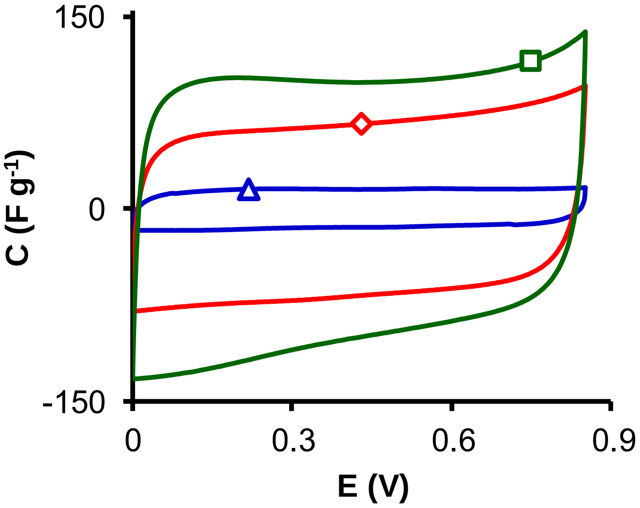

Figure 3. Cyclic voltammograms at 5 mV s^{-1} in 1M H_2SO_4 of samples: CA △, CB ◇ and CC □.

6. REFERENCES

[1] Niaounakis, M. Halvadakis, C.P. Olive processing waste management. 2nd ed. Elsevier; (2006).

[2] Fernández-Hernández, A. Martínez, A. Rivas, F. García-Mesa, J.A. Parra, A. Effect of the solvent and the sample preparation on the determination of triterpene compounds in two-phase olive-mill-waste samples. J Agric Food Chem, 63(17) (2015) 4269-4275.

[3] Moreno-Castilla, C., Carrasco-Marín, F., López-Ramón, M.V., Álvarez-Merino, M.A. Chemical and physical activation of olive-mill waste water to produce activated carbons. Carbon 39(9) (2001) 1415-1420.

[4] Moreno Castilla, C. Colloidal and micro-carbon spheres derived from low-temperature polymerization reactions. Adv. Colloid Interface Sci. 236 (2016) 113-141.

[5] Büchel, G. Unger, K.K. Matsumoto, A. Tsutsumi, K. A novel pathway for synthesis of submicrometer-size Solid core/mesoporous shell silica spheres. Avd. Mater. 10(13) (1998) 1036-1038.

[6] Thommes, M. Kaneko, K. Neimark, A.V. Olivier, J.P. Rodríguez-Reinoso, F. Rouquerol, J. et al. Physisorption of gases, with special reference to the evaluation of surface area and pore size distribution (IUPAC technical report) Pure Appl. Chem. 87(9-10) (2015) 1051-1069.

CAPÍTULO V

CHAPTER V

SUPERCAPACITOR PERFORMANCE IN ACID AND BASIC ELECTROLYTES OF MONOLITHIC CARBON AEROGELS WITH DIFFERENT PORE TEXTURE

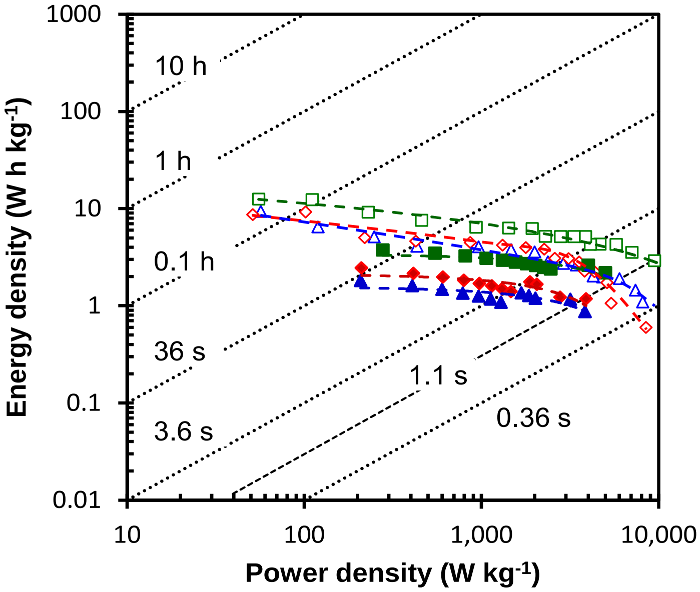

1. ABSTRACT

The objective of this work is to investigate the supercapacitor behavior in acid and basic electrolytes of various carbon aerogels (CAs) up to high charge-discharge rates and to correlate it with their pore texture. For this purpose, three microporous CAs with different pore textures are selected. Their capacitance performance is studied in a two-electrode cell by electrochemical impedance spectroscopy (EIS), and galvanostatic charge-discharge (GCD). Gravimetric capacitances increase with higher mean micropore width. The electrical resistance is higher in basic than in acid electrolytes, and the macroporous CA has the highest electrical resistance in both. The CA with the highest micropore volume, with a mean width of 1.15 nm, and the highest volume of mesopores, with a mean size of 5.8-8.8 nm, has the highest volumetric capacitance at a current load of 1 A g^{-1} in H_2SO_4 (109 F cm^{-3}) and in KOH (120 F cm^{-3}), with a capacitance retention *ca.* 75 % at 14 A g^{-1} (H_2SO_4) and at 20 A g^{-1} (KOH). These volumetric capacitances are higher than those required for utilization in small-volume systems. The above sample delivers the best performance in acid electrolyte at higher rates, with an energy density of 3 W h kg^{-1} at a power density of 10 kW kg^{-1}.

Keywords: Carbon aerogels; Supercapacitor performance; Galvanostatic charge-discharge; Electrochemical impedance spectroscopy.

2. INTRODUCTION

Porous carbon materials are among the best candidates for utilization as supercapacitor electrodes, because their high surface area and developed porosity favors the electrochemical double-layer (EDL) formation [1]. Furthermore, they can be treated to introduce chemical functionalities containing oxygen or nitrogen, which can enhance the capacitance through pseudocapacitance effects [1]. However, many microporous carbons, including activated carbons, have an irregular pore size distribution with a predominance of narrow micropores, limiting the transportation of electrolyte ions throughout the porous network [2,3]. This hampers the use of these materials at high charge-discharge rates, because the accessibility of ions to the porosity also depends on the process rate. It has been proposed to overcome this drawback by using micropore carbons with a regular size that contain some mesoporosity [3] or by using microporous carbons with a wide micropore size distribution [2].

Carbon gels are porous materials obtained after carbonizing organic gels prepared by sol-gel polymerization of compounds such as resorcinol (R) and formaldehyde (F) using basic or acid catalysts. They can have a high surface area and a well-developed and interconnected pore texture and their synthesis and processing conditions were recently reviewed [4].

The objective of this work was to investigate the supercapacitor behavior of various CAs up to high charge-discharge rates and to correlate it with their pore texture. For this purpose, three microporous CAs with different pore textures were selected [5,6]: the first also contained some mesopores up to 4 nm width; the second had a higher mesoporosity, with width of 32 nm, and a well-developed macroporosity, and the third had a similar mesopore volume to that of the second but with a mean width of 5.8 to 8.8 nm and no macropores. The supercapacitor performance was studied by GCD, and EIS in a two-electrode cell using H_2SO_4 and KOH as electrolytes.

3. EXPERIMENTAL

3.1. Synthesis of the carbon aerogels

Three organic aerogels were prepared by sol-gel polymerization reaction of R and F according to recipes given in Table 1 and following the method described elsewhere [5,6]. The hydrogels were supercritically dried with carbon dioxide, after exchanging the solvent by acetone, and pyrolyzed in N_2 flow at 900 ºC for 5 h. Organic and carbon aerogels will be indicated in the text by the letters OA and CA, respectively, designating the samples obtained by appending the numbers 1, 2, or 3.

Table 1. Recipes of the organic gels

Sample	Resorcinol	Formaldehyde	Catalyst	Water	Other solvents
	mol	mol	1.4×10^{-4} mol	mL	mL
OA1	0.224	0.112	K_2CO_3	24.5	2.3 THF
OA2	0.224	0.112	Na_2CO_3	24.5	2.3 MeOH
OA3	0.224	0.112	K_2CO_3	13.1	2.3 MeOH

3.2. Surface characterization

CAs were characterized by N_2 and CO_2 adsorption at -196 and 0 ºC, respectively, mercury porosimetry, and X-ray photoelectron spectroscopy (XPS).Adsorption isotherms were measured with an Autosorb 1 from Quantachrome. The BET equation was applied to the N_2 adsorption isotherms to obtain the surface area, S_{BET}. The Dubinin-Radushkevich (DR) equation was applied to N_2 and CO_2 adsorption isotherms to determine the volume of micropores, W_0, and their mean width, L_0. The mesopore volume, V_{meso}, was obtained from the difference between the volume of nitrogen adsorbed at p/p_0 =0.95and $W_0(N_2)$; the mean mesopore size, d_{BJH}, was determined by the BJH method applied to the adsorption branch of the type IV N_2 adsorption-desorption isotherms.

Mercury porosimetry was obtained up to a pressure of 4200 kgcm^{-2} using Quantachrome Autoscan 60 equipment. This technique yielded the pore size distribution, PSD, of pores wider than 3.7 nm, and their mean width, d_{Hg}. It also provided the volume of macropores (wider than 50 nm), which is not precisely measured by N_2 adsorption [7], and the particle or packing density at atmospheric pressure, ρ.

XPS was performed using an Escalab 200R system (VG Scientific Co.) equipped with MgK_{α} X-ray source (hυ = 1253.6 eV) and hemispherical electron analyzer and using the C_{1s} peak at 284.6 eV as internal standard. This technique provided the surface oxygen content, O_{XPS}.

3.3. Electrochemical measurements

The supercapacitor performance of the carbon aerogels was evaluated in 1M H_2SO_4 and 6M KOH using a two-electrode cell and a Biologic VMP multichannel potentiostat. Electrodes were prepared from a well-mixed slurry of the finely ground carbon aerogel (90 wt. %) with PTFE as binder (10 wt. %). The slurry was pressed at 8 bar on graphite paper discs and dried in an oven at 120 ºC. The discs had an area of 0.50 cm^2 and contained the same amount of active material, 5 mg. The electrodes were immersed in an excess of the electrolyte solution for five days before performing any measurement.

The supercapacitors were constructed using a Teflon Swagelok-type cell formed by two electrodes identical in size and weight that were electrically isolated by a porous fibrous separator impregnated with the electrolyte solution. GCD cycles were determined at current loads between 1 and 20 A g^{-1} (10 and 200 mA cm^{-2}). Gravimetric capacitances were calculated from the discharge curves of the GCD by the equation $C_{GD} = I_d \Delta t / m \Delta V$, where I_d is the discharge current, Δt the discharge time and m (g) is the total mass of the active material in the two electrodes. EIS was performed by sweeping the frequency in the range between 100 kHz and 1 mHz with a sinusoidal signal amplitude of 10 mV. The capacitance value, C, was obtained by the equation $C = -Z'' / 2\pi f |Z|^2$ where f is the frequency and $|Z|^2 = Z'^2 + Z''^2$, with Z' and Z'' being the real and imaginary parts of the complex impedance, respectively.

For performance comparison, the gravimetric capacitances obtained from the above equations were multiplied by four to express them per single electrode, which is the three-electrode cell equivalent. However, as per convention [8], the gravimetric capacitances of two-electrode cells obtained from galvanostatic charge-discharge equation were used to calculate the energy density ($E = C_{GD(2E)}V^2/2$) in the Ragone plot, where V is the voltage omitting the IR drop. Power density was calculated from $P = IV/2m$, where I is the current (A) and m the total mass of active material (g) in the two electrodes.

4. RESULTS AND DISCUSSION

The shapes of N_2 adsorption-desorption isotherms (Figure 1) differ among the samples. Thus, CA1 has a type I isotherm [9] with no hysteresis cycle, typical of microporous solids, although there is a slight increase in N_2 uptake with the rise in relative pressure after micropore filling, indicating the presence of mesopores of *ca.* 4 nm in size [10]. However, CA2 and CA3 show type IV isotherms, typical of mesoporous materials, and the shape of the isotherm for sample CA2 also indicates the presence of macropores.

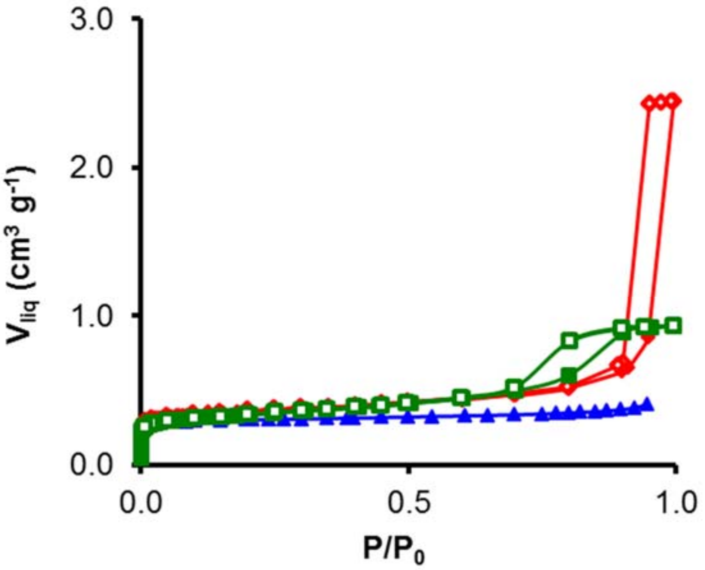

Figure 1. N_2 adsorption-desorption isotherms at -196 °C on carbon aerogels △, CA1; ◇, CA2; □, CA3. Adsorption, closed symbols; desorption, open symbols

PSDs (Figure 2) are monomodal, which is characteristic of CAs [6]. Results obtained (see Table 2) show that CA2 has a large macropore volume, with a mean size of 59 nm, whereas CA1 and CA3 have no macropores and a d_{Hg} value of 4.3 and 5.8 nm, respectively. The d_{Hg} value of CA1 is consistent with the shape of its N_2 adsorption isotherm, and the d_{Hg} value of CA3 is close to its d_{BJH} value, taking into account that they were obtained using very different techniques. On the other hand, samples CA3 and CA2 have a higher particle density than CA2 due to they have no macropores in their structure. The CA3 particle density is close to that of commercial activated carbons used in supercapacitors, such as super DLC-50, i.e. ~ 0.75 cm^3 g^{-1} [11].

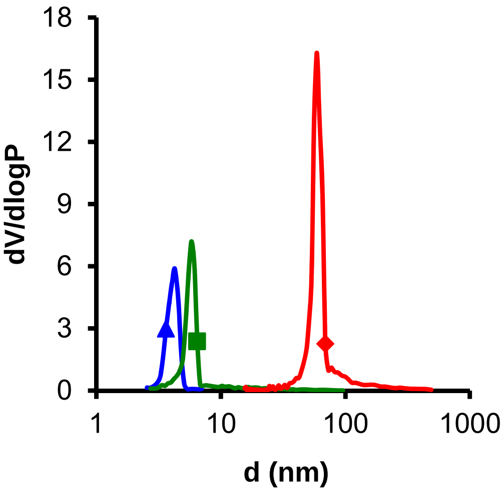

Figure 2. Pore size distribution from mercury porosimetry for carbon aerogels: ▲, CA1; ◆, CA2; ■, CA3

Table 2. Surface area, pore texture and surface oxygen content of carbon aerogels

Sample	S_{BET}	$W_0(N_2)$	$L_0(N_2)$	$W_0(CO_2)$	$L_0(CO_2)$	V_{meso}	V_{macro}	d_{BJH}	d_{Hg}	ρ	O_{XPS}
	$m^2\ g^{-1}$	$cm^3\ g^{-1}$	nm	$cm^3\ g^{-1}$	nm	$cm^3\ g^{-1}$	$cm^3\ g^{-1}$	nm	nm	$g\ cm^{-3}$	%
CA1	724	0.28	0.61	0.25	0.65	0.13	0	--	4.3	0.70	5.0
CA2	850	0.34	0.82	0.30	0.63	0.53	1.93	32.0	59.0	0.35	1.9
CA3	780	0.32	1.15	0.29	0.63	0.58	0	8.8	5.8	0.72	4.0

Table 2 also exhibits the S_{BET} values and microporous characteristics of the carbon aerogels. $W_0(N_2) \geq W_0(CO_2)$ in all samples, indicating no micropore constrictions. In CA1, a typical microporous sample, $L_0(N_2) \approx L_0(CO_2)$, whereas in CA2 and CA3 $L_0(N_2) > L_0(CO_2)$ indicating a more heterogeneous micropore size distribution.

The O_{1s} XP spectra of samples are depicted in Figure 3. The deconvoluted spectra show two peaks at 531.7 and 533.1 eV, corresponding to functionalities with double C=O bonds (as carboxyl and quinone groups) and single C-OH bonds (as carboxyl and phenol groups), respectively [11]. In all samples, the relative surface concentrations of these functionalities are 40 and 60 %, respectively. The O_{XPS} content (Table 2) is the lowest in CA2 and broadly similar between CA1 and CA3. This oxygen increases the wettability of the CAs and can originates pseudocapacitive effects.

The charge transport within the pore network was the first electrochemical property of the CAs evaluated. Thus, Figure4 depicts the Nyquist plots for the CA-based supercapacitors, showing the typical features of porous electrodes, i.e., resistance at high frequency and capacitance at low frequency. Thus, a semicircle appears in the high frequency region and is related to the sum of the electrolyte resistance, carbon material internal resistance, and contact resistance at the active material/current collector interface. It is generally considered that the width of the semicircle, R_p, reflects the resistance of the active material, because the same electrolyte and technique are used to prepare the electrodes in the experiments [13,14].

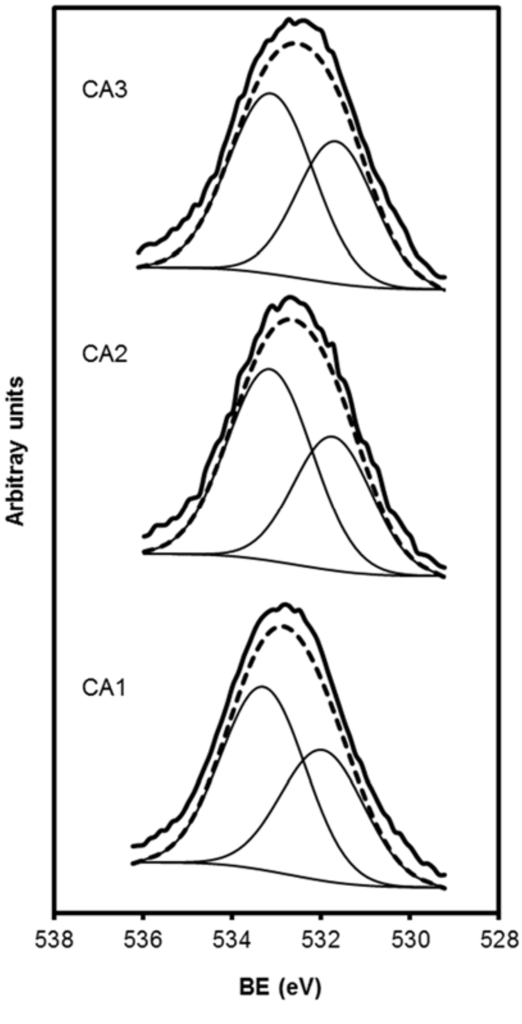

Figure 3. X-ray photoelectron spectroscopy profiles of the O_{1s} region for carbon aerogels CA1, CA2 and CA3

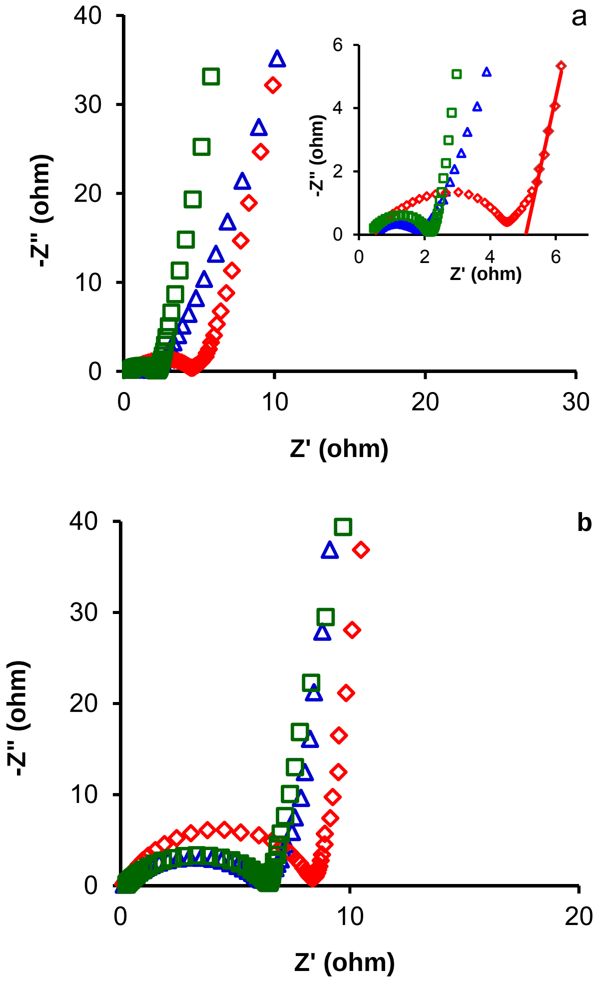

Figure 4. Nyquist plots in (a) 1 M H_2SO_4 and (b) 6 M KOH in the frequency range of 10 kHz to 1mHz. Samples: △, CA1; ◆, CA2; ■, CA3

The equivalent series resistance (ESR) is obtained from the intersection point of the impedance with the real axis in the very low frequency region [15] (see inset in Figure4). ESR and R_p values (Table 3) are fairly similar and are smaller when using H_2SO_4 as electrolyte instead of KOH. In addition, ESR and R_p values in both electrolytes increase in the order CA1 ≈ CA3 < CA2, attributable to the large macropore volume of sample CA2, which increases its internal resistance.

The real part of the capacitance (C') decreases when the frequency increases (Figure 5), and the supercapacitor is converted to a pure resistance at a high frequency. This decrease depends on parameters related to the porous texture of the electrode active material, the electrode thickness, and the electrolyte [16]. Thus, the real capacitance is null at a frequency of around 1 Hz in the acid electrolyte and at 0.1 Hz in the basic electrolyte, reflecting the higher electrical resistance of the electrodes in the latter. In both types of electrolyte, CA3 gives the best performance.

Table 3 displays the capacitance obtained at the lowest frequency of 1 mHz (C_{max}). Each carbon aerogel shows equal C_{max} in both electrolytes and it increases linearly with higher $L_0(N_2)$ within the range studied (Figure 6a). This relationship, previously observed in KOH-activated CAs [17], indicates the importance of the mean size of the total microporosity in EDL formation.

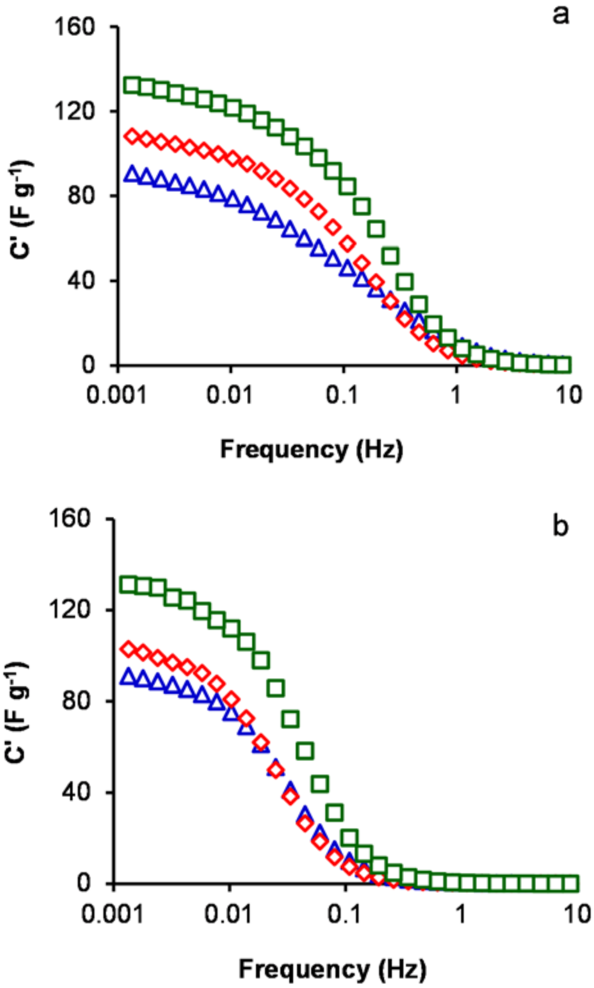

Figure 5. Variation of the real part of the capacitance with the frequency (c) in 1 M H_2SO_4 and (d) 6 M KOH for the supercapacitors based on carbon aerogels: △, CA1; ◇, CA2; □, CA3

Table 3. Electrical resistance (R_p), equivalent series resistance (ESR) from electrochemical impedance spectroscopy, and gravimetric (C_{GD}) and volumetric (VC_{GD}) capacitances from galvanostatic charge-discharge at 1 A g^{-1} in 1 M H_2SO_4 and 6 M KOH

Sample	Electrolyte	R_P Ω	ESR Ω	C_{GD} F g^{-1}	VC_{GD} F cm^{-3}
CA1	H_2SO_4	1.9	2.3	99	69
CA2		4.2	5.2	104	36
CA3		2.1	2.4	152	109
CA1	KOH	5.9	6.2	87	61
CA2		8.1	8.4	109	38
CA3		6.2	6.5	166	120

Figure 7 shows typical G_{CD} curves at 1 A g^{-1} for the supercapacitors using carbon aerogels as electrode materials. G_{CD} curves at higher current loads are depicted for CA3 in Figure 8. These curves present a slight deviation from linearity which reflects the presence of pseudocapacitive processes due to the oxygen content. Gravimetric capacitances were calculated from these curves in the voltage window during the discharge process after the IR drop. The capacitances at 1 A g^{-1} (Table 3) are comparable to the C_{max} from EIS, although C_{GD} is higher than C_{max} for CA3. C_{GD} also shows a linear relationship with $L_0(N_2)$ (Figure 6b).

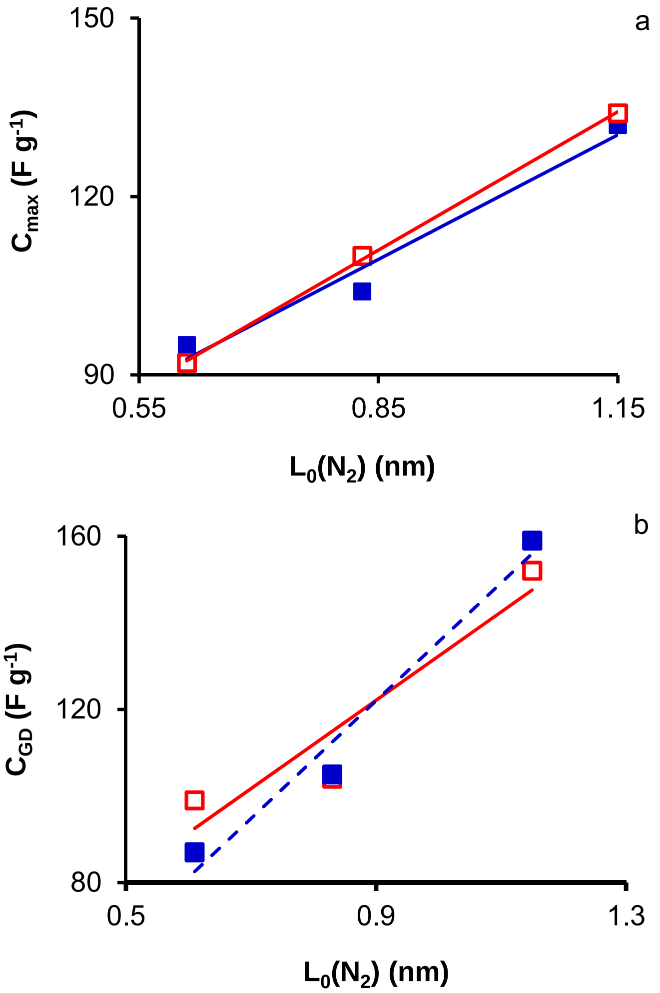

Figure 6. Relationship of C_{max} from EIS at 1mHz (a) and C_{GD} from CGD at 1 A g^{-1} (b) with $L_0(N_2)$ in: □, 1 M H_2SO_4 and ■, 6 M KOH

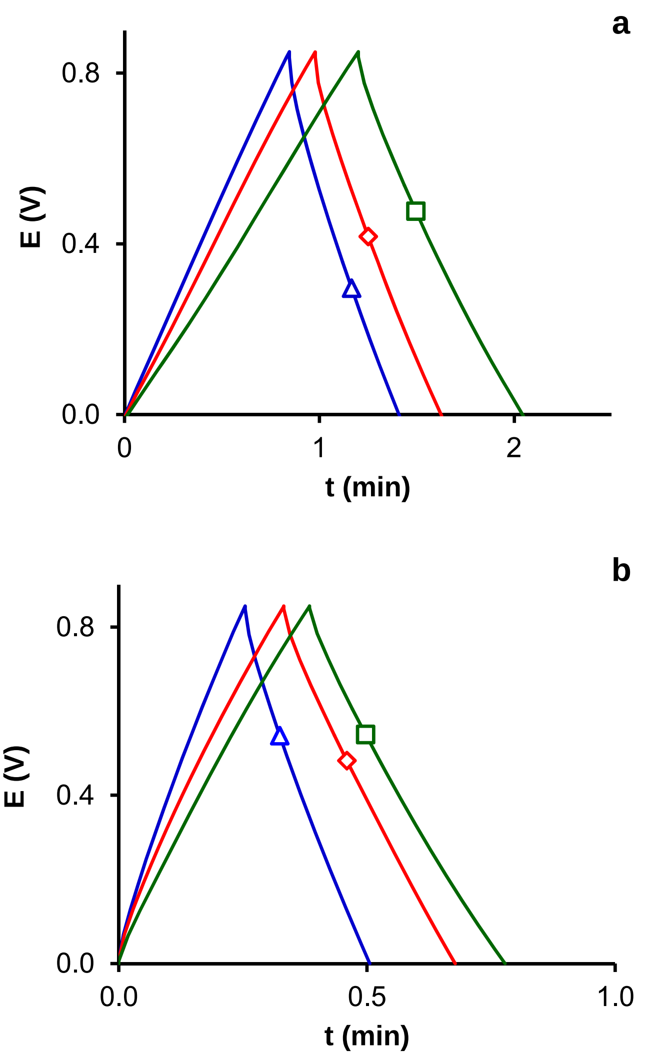

Figure 7. Galvanostatic charge-discharge curves at 1 Ag^{-1} in (a) 1 M H_2SO_4, and (b) 6 M KOH for the supercapacitors based on carbon aerogels: △, CA1; ◇, CA2; □, CA3

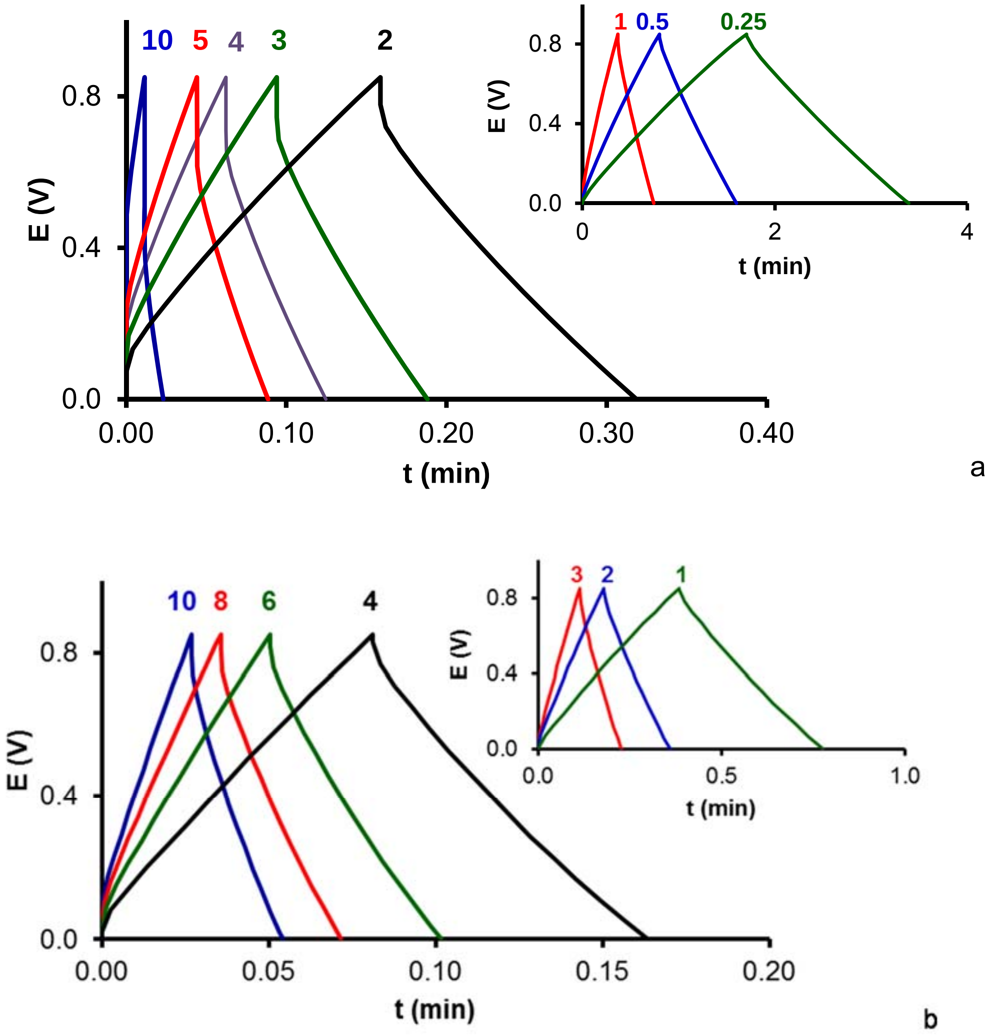

Figure 8. Galvanostatic charge-discharge curves at different current densities, Ag^{-1}, in (a) 1 M H_2SO_4 and (b) 6 M KOH for supercapacitor based on carbon aerogel CA3

The volumetric capacitance is also critical for practical applications in small-volume devices. It involves the use of carbon electrode materials with a high density, which is often incompatible with a developed porosity. Table 3 also compiles the volumetric capacitance, VC_{GD}, obtained from GCD and the particle density [12,18,19], showing that the lowest VC_{GD} value is for CA2 because it has the lowest particle density. The highest volumetric capacitance in H_2SO_4 and KOH as electrolytes, 109 and 120 F cm^{-3}, respectively, is obtained with CA3. These volumetric capacitances are higher than the 54 F cm^{-3} reported for a hierarchical porous carbon [20], 30 F cm^{-3} for carbon aerogels from biomass [21], 92 F cm^{-3} for KOH-activated carbon aerogels at 1 A g^{-1} [17], and the 60 F cm^{-3} generally required for practical applications [22].

C_{GD} decreases with higher current load (Figure 9). Sample CA3 again shows the best performance, with capacitance retention of *ca.* 75 % when the current load increases to 14 A g^{-1} (in H_2SO_4) or to 20 A g^{-1} (in KOH). This is because CA3 has the widest $L_0(N_2)$ value and highest volume of small mesopores, favoring the transport of ions through the carbon porosity at a fast charge-discharge rate.

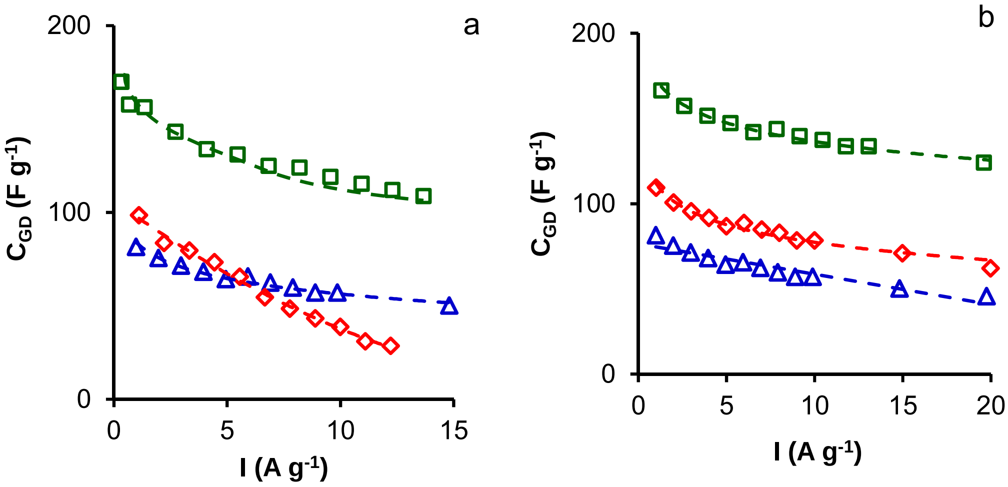

Figure 9. Variation in the gravimetric capacitance with current load in (a) 1 M H_2SO_4 and (b) 6 M KOH for the supercapacitors based on carbon aerogels: △, CA1; ◇, CA2; □, CA3

Ragone diagrams determined from GCDs at different current loads in acid and basic electrolytes are depicted in Figure 10. The best-performing symmetric carbon supercapacitors described in the literature [23] have energy densities of around 10 W h kg^{-1} of active material, and this value decreases at higher power densities. Results obtained in 1 M H_2SO_4 show that the energy density at a power density of 50-55 W kg^{-1} is 10 W h kg^{-1} for CA1 and CA2 and 14 W h kg^{-1} for CA3. These parameters vary significantly at higher rates and shorter current drain times. Thus, for a current drain time of 1.1 s, the energy and power densities are similar for CA1 and CA2 (1.5 W h kg^{-1} and 6 kW kg^{-1}) but higher for CA3 (3 W h kg^{-1} and 10 kW kg^{-1}).

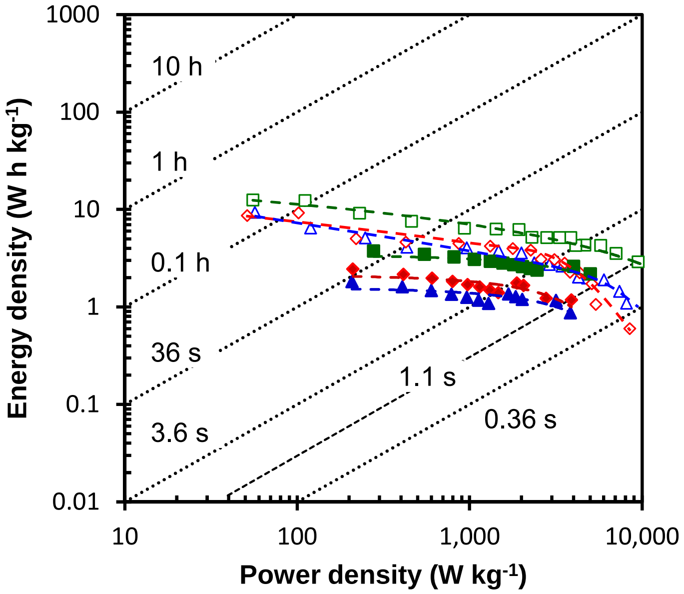

Figure 10. Ragone diagrams in (a) 1 M H_2SO_4 (open symbols) and (b) 6 M KOH (closed symbols) for the supercapacitors based on carbon aerogels: △, CA1; ◇, CA2; □, CA3

The superior performance of CA3 is due to its more suitable pore texture, because it has been shown that the presence of mesopores (usually 2-8 nm in size) accelerates the kinetics of ion diffusion in the electrodes and improves the power at higher current densities, whereas micropores accessible to the electrolyte ions are essential for high energy storage [24,25]. Thus, CA3 (Table 2) has the highest volume of mesopores, with a mean size of 5.8-8.8 nm, and the highest volume of micropores, with a size

(1.15 nm) that is more favorable for EDL formation, as evinced by its highest C_{GD} value at different current loads (Figure9).

Energy and power densities found with these carbon aerogels in 1 M H_2SO_4, especially with CA3, are higher than values reported in the literature for Maxorb (2 W h kg^{-1} and 0.4 kW kg^{-1}) and ordered mesoporous carbons (4-6 W h kg^{-1} and 0.8-1.0 kW kg^{-1}) in 30 wt.% KOH [26], carbide-derived carbons (1-2 W h kg^{-1} and 1.5-3 kW kg^{-1}) in 2M H_2SO_4 [27], mesoporous carbons from polyvinyl alcohol (1 W h kg^{-1} and 2.6 kW kg^{-1}) in 2M H_2SO_4 [28] and activated carbons from cherry stones (1 W h kg^{-1} and 1.5 kW kg^{-1}) in 2M H_2SO_4 [29]. The behavior of CA3 is similar to that of a high-performance carbon obtained by carbonization of sodium alginate (4 W h kg^{-1} and 10 kW kg^{-1}) in 1M H_2SO_4 [23].

The performance of these CAs is something worse in 6 M KOH than in 1 M H_2SO_4 (Figure 5) due to the higher electrical resistance in the basic electrolyte. Thus, at a similar current drain time the energy and power densities are lower in the basic than in the acid electrolyte.

Samples exhibit practically no capacitance fading after 2500 charge-discharge cycles at 5 A g^{-1} in a voltage window between 0 and 0.85 V (Figure 11a). Self-discharge curves (Figure 11b) show that the time needed for a 50 % of self-discharge is higher in acidic than in basic electrolyte. In both electrolytes, this time decreases in the order CA1 > CA3 > CA2, because the volume of meso- and macropores increases in the order CA1 < CA3 < CA2.

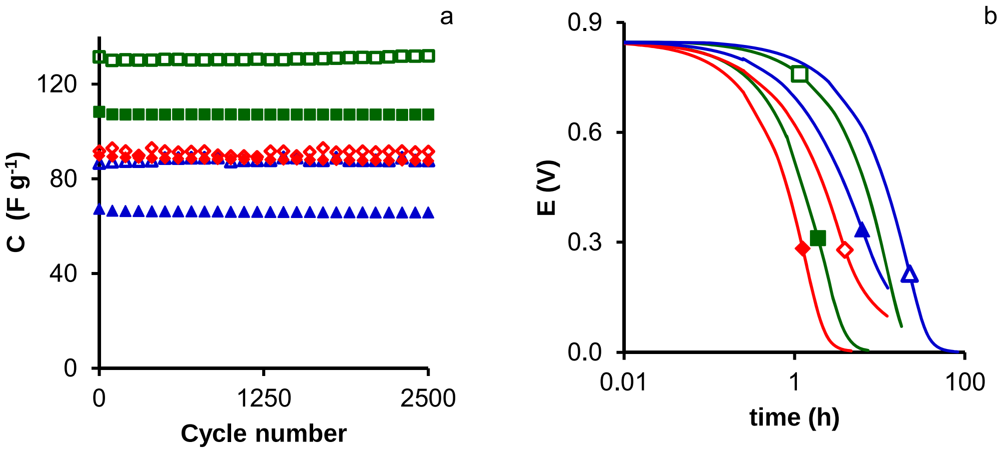

Figure 11. Variation of C_{GD} with the number of charge-discharge cycles at 5 A g^{-1} in the voltage window between 0 and 0.85 V in 1 M H_2SO_4 (open symbols) and 6 M KOH (closed symbols). (b) Self-discharge curves in 1 M H_2SO_4 (open symbols) and 6 M KOH (closed symbols) for the supercapacitors based on carbon aerogels: △, CA1; ◇, CA2; □, CA3

5. CONCLUSIONS

Gravimetric capacitances of CAs determined in 1 M H_2SO_4 or 6 M KOH increase with greater mean width of the total micropore volume in the range studied (0.61-1.15 nm) Electrical resistance is higher in the basic than in the acid electrolyte, and the macroporous carbon aerogel shows the highest electrical resistance in both cases.

The CA with the highest micropore volume, with a mean width of 1.15 nm, and the highest volume of mesopores, with a mean size of 5.8-8.8 nm, has the highest gravimetric and volumetric capacitances at a current load of 1 A g^{-1} in H_2SO_4 (152 F g^{-1} and 109 F cm^{-3}) and in KOH (166 F g^{-1} and 120 F cm^{-3}), respectively. The capacitance retention is *ca.* 75% at 14 A g^{-1}(H_2SO_4) and at 20 A g^{-1} (KOH). These volumetric capacitances are higher than other reported in the literature for carbon materials and than is required for utilization in small-volume systems, 60 F cm^{-3}. This CA has a high supercapacitor performance in acid electrolyte with an energy density of 14 W h kg^{-1} at a power density of 50-55 W kg^{-1} and of 3 W h kg^{-1} and 10 kW kg^{-1} at higher rates, respectively. The CAs all perform something worse in basic electrolyte, due to their higher electrical resistance.

Virtually no fading is observed for any of the CAs after 2500 charge-discharge cycles. The time for a 50 % of self-discharge is longer in acid than in basic electrolyte and increases with lower meso- and macropore volumes in both cases.

6. REFERENCES

[1] Moreno-Castilla C, Maldonado-Hódar FJ. Carbon aerogels for catalysis applications: an overview. Carbon 2005; 43(3): 455-65.

[2] Pekala RW, Kong FM. Resorcinol-formaldehyde aerogels and their carbonized derivatives. Polym. Prep. 1989; 30: 221-3.

[3] Al-Muhtaseb SA, Ritter JA. Preparation and properties of resorcinol-formaldehyde organic and carbon gels. Avd. Mater 2003; 15: 101-14.

[4] Rodríguez-Reinoso F, Rodríguez-Ramos I, Moreno-Castilla C, Guerrero-Ruiz A, López-González JD. Platinum catalysts supported on activated carbon. I Preparation and characterization. J. Catal. 1986; 99(1): 171-83.

[5] Saquing CD, Cheng TT, Aindow M, Erkey C. Preparation of platinum/carbon aerogel nanocomposites using a supercritical deposition method. J Phys Chem B 2004; 108: 7716-22.

[6] Marie J, Berthon-Fabry S, Achard P, Chatenet M, Pradourat A, Chainet E. Highly dispersed platinum on carbon aerogels as supported catalysts for PEM fuel cell-electrodes: comparison of two different synthesis paths. J Non-Cryst Solids 2004; 350: 88-96.

[7] Smirnova A, Dong X, Hara H, Vasiliev A, Sammes N. Novel carbon aerogel-supported catalysts for PEM fuel cell application. Int J Hydrogen Energ 2005; 30(2): 149-58.

[8] Marie J, Berthon-Fabry S, Chatenet M, Chainet E, Pirard R, Cornet N, et al. Platinum supported on resorcinol-formaldehyde based carbon aerogels for PEMFC electrodes: Influence of the carbon support on electrocatalytic properties. J. Appl. Electrochem. 2007; 37: 147-53.

[9] Du H, Gan L, Li B, Wu P, Qiu Y, Kang F, et al. Influences of Mesopore Size on Oxygen Reduction Reaction Catalysis of Pt/Carbon Aerogels. J Phys Chem C 2007; 111(5): 2040-3.

[10] Kim HJ, Kim WI, Park TJ, Park HS, Suh DJ. Highly dispersed platinum-carbon aerogel catalyst for polymer electrolyte membrane fuel cells. Carbon 2008; 46(11): 1393-400.

[11] Maldonado-Hódar FJ, Moreno-Castilla C, Pérez-Cadenas AF. Catalytic combustion of toluene on platinum-containing monolithic carbon aerogels. Appl Catal B 2004; 54(4): 217-24.

[12] Padilla-Serrano MN, Maldonado-Hódar FJ, Moreno-Castilla C. Influence of Pt particle size on catalytic combustion of xylenes on carbon aerogel-supported Pt catalysts. Appl Catal B 2005; 61(3-4): 253-8.

[13] Moreno-Castilla C, Maldonado-Hódar FJ, Pérez-Cadenas AF. Physico-chemical surface properties of Fe, Co, Ni and Cu-doped monolithic organic aerogels. Langmuir 2003; 19(14): 5650-5.

[14] Moreno-Castilla C, Ferro-García MA, Joly JP, Bautista-Toledo I, Carrasco-Marín F, et al. Activated carbons surface modifications by nitric

acid, hydrogen peroxide and ammonium peroxydisulfate treatments. Langmuir 1995; 11(11): 4386-92.

[15] Cazorla-Amorós D, Alcañiz-Monge J, De la Casa-Lillo MA, Linares-Solano A. CO_2 as an adsorptive to characterize carbon molecular sieves and activated carbons.Langmuir 1998;14: 4589-96.

[16] Stoeckli F. Characterization of microporous carbons by adsorption and immersion techniques. In: Patrick JW, editor. Porosity in carbons: characterization and applications, London: Edward Arnold, 1995: 66-97.

[17] Bansal RC, Donnet JB. Stoeckli F. Active Carbon. New York: Marcel Dekker. 1988: Chapter 3.

[18] Ubago-Pérez R, Carrasco-Marín F, Moreno-Castilla C. Carbon-supported Pt as catalysts for low-temperature methanol decomposition to carbon monoxide and hydrogen. Appl Catal A 2004; 275(1-2): 119-26.

[19] Job N, Pirard R, Pirard JP, Alié C. Non intrusive mercury porosimetry: Pyrolysis of resorcinol-formaldehyde xerogels. Part Part Syst Charact 2006; 23(1): 72-81.

[20] Denoyel R, Fernández-Colinas J, Grillet Y, Rouquerol J. Assessment of the surface-area and microporosity of activated charcoals from immersion calorimetry and nitrogen adsorption data. Langmuir 1993; 9(2): 515-8.

[21] Gonzalez MT, Sepúlveda-Escribano A, Molina-Sabio M, Rodriguez-Reinoso F. Correlation between surface areas and micropore volumes of activated carbons obtained from physical adsorption and immersion calorimetry. Langmuir 1995; 11(6): 2151-5.

[22] Silvestre-Albero J, Gómez de Salazar C, Sepúlveda-Escribano A, Rodriguez-Reinoso F. Characterization of microporous solids by immersion calorimetry. Colloids Surf A 2001; 187-188: 151-65.

[23] Villar-Rodil S, Denoyel R, Rouquerol J, Martinez-Alonso A, Tascón JMD. Characterization of aramid based activated carbon fibres by adsorption and immersion techniques. Carbon 2002; 40(8): 1376-80.

[24] Job N, Pereira MFR, Lambert S, Cabiac A, Delahay G, Colomer JF, et al. Highly dispersed platinum catalysts prepared by impregnation of texture-tailored carbon xerogels. J Catal 2006; 240 (2), 160-71.

[25] Ordoñez S, Díez FV, Sastre H. Characterisation of the deactivation of platinum and palladium supported on activated carbon used as hydrodechlorination catalysts. Appl Catal B 2001; 31(2), 113-22.

[26] Choi HC, Choi SH, Yang OB, Lee JS, Lee KH, Kim YG. Hydrodechlorination of Carbon Tetrachloride over Pt/MgO. J Catal 1996; 161(2): 790-7.

[27] Coloma F, Sepúlveda-Escribano A, Fierro JLG, Rodríguez-Reinoso F. Preparation of platinum supported on pregraphitized carbon-blacks. Langmuir 1994; 10(3): 750-5.

[28] Esumi K, Matsuhisa K, Torigoe K. Preparation of Rodlike Gold Particles by UV Irradiation Using Cationic Micelles as a Template. Langmuir 1995; 11(9): 3285-7.

[29] Ohara PC, Heath JR, Gelbart WM. Self-assembly of submicrometer rings of particles from solutions of nanoparticles. Angew Chem Int Ed Engl 1997; 36(10): 1077-80.

[30] Chung SW, Markovich G, Heath JR. Fabrication and Alignment of Wires in Two Dimensions. J Phys Chem B 1998; 102(35): 6685-7.

[31] Hutchinson TO, Liu YP, Kiely C, Kiely CJ, Brust M. Templated gold nanowire self-assembly on carbon substrates. Adv Mater 2001; 13(23): 1800-3.

[32] Murphy CJ, Jana NR. Controlling the aspect ratio of inorganic nanorods and nanowires. Adv Mater 2002; 14(1): 80-2.

[33] Kim F, Song JH, Yang P. Photochemical Synthesis of Gold Nanorods. J Am Chem Soc 2002; 124(48): 14316-7

[34] Sun Y, Xia Y. Large-scale synthesis of uniform silver nanowires through a soft, self-seeding, polyol process. Adv Mater 2002; 14(11): 833-7.

[35] Surendran G, Apostolescu G, Tokumoto M, Prouzel E, Ramos L, Beaunier P, et al. From self-assembly of platinum nanoparticles to nanostructures materials. Small 2005; 1(10): 964-7.

[36] Tang Z, Kotov NA. One-dimensional assemblies of nanoparticles: Preparation, properties and promise. Adv Mater 2005; 17(8): 951-62.

[37] Nakashima H, Furukawa K, Kashimura Y, Torimitsu K. Self-Assembly of Gold Nanorods Induced by Intermolecular Interactions of Surface-Anchored Lipids. Langmuir, 2008; 24(11): 5654-8

CAPÍTULO VI

CHAPTER VI

MELIA AZEDARACH STONE-DERIVED ACTIVATED CARBONS FOR SUPERCAPACITOR ELECTRODES

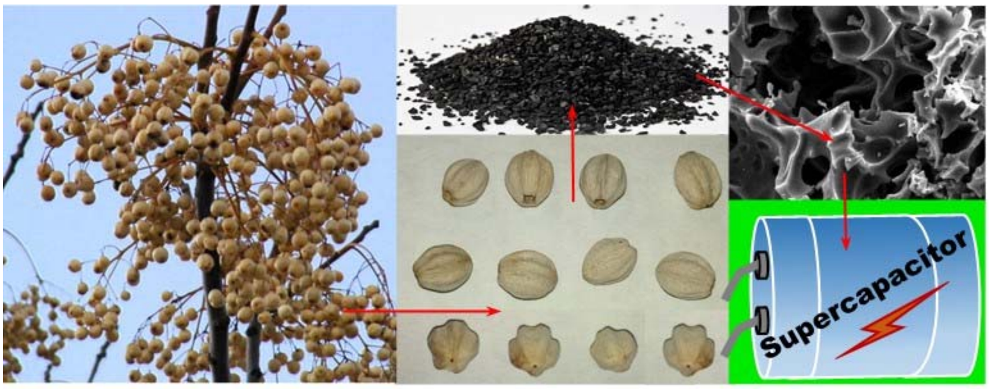

1. ABSTRACT

Waste biomass-derived activated carbons (ACs) are promising materials for supercapacitor electrodes due to their abundance and low cost. In this study, we investigated the potential use of *Melia Azedarach* (MA) stones as raw material to prepare ACs for supercapacitors. The ash content was considerably lower in MA stones (0.7 % ash) than found in other lignocellulosic wastes. Three AC series were prepared by KOH activation of MA stones (MA series), carbonized MA stones (CMA series) and hydrothermally treated MA stones (HMA series). The morphology, composition, surface area, porosity and surface chemistry of the ACs were determined. Electrochemical measurements were carried out in three- and two-electrode cells, 3EC and 2EC, respectively, using 1M H_2SO_4 as electrolyte. The largest surface area obtained was *ca*. 2000 m^2 g^{-1} and the highest capacitance from galvanostatic charge-discharge (GCD) in 2EC ranged between 232 and 240 F g^{-1} at 1 A g^{-1}.The maximum energy density reached was 27.4 Wh kg^{-1} at a power density of 110 W kg^{-1}. Electrochemical impedance spectroscopy (EIS) in 2EC revealed an increase in equivalent series resistance (ESR) and charge transfer resistance (R_{CT}) with greater ash content. Floating tests showed that the ACs have good cycling stability.

Keywords: *Melia Azedarach* stones; Biomass wastes; Activated carbons; Supercapacitor electrodes; Energy storage.

2. INTRODUCTION

Supercapacitors or electrochemical capacitors are energy storage devices with ideal characteristics for the rapid storage and release of energy and for a long-term cycling life [1-3]. This capability is mainly achieved through a non-faradic mechanism by the separation of ions across a very small distance in the electrochemical double-layer (EDL) at the electrolyte/electrode interface, and it is dependent on the surface area of the electrode and the accessibility of the electrolyte to its porosity. EDL capacitance can be improved by reversible faradic reactions that introduce pseudocapacitance [1-3].

Porous carbon materials are widely used as supercapacitor electrodes due to their high surface area, well-developed porosity, high conductivity, good physicochemical stability, and the presence of functionalities such as oxygen and nitrogen complexes, which can introduce pseudocapacitance phenomena [2-5]. ACs are a highly interesting type of porous carbon material for use as supercapacitor electrodes because they can be obtained from readily available, inexpensive and renewable raw materials, including biomass residue and waste. Their utilization is also a form of confronting the problem of waste disposal. Thus, various studies have recently been published on the preparation of ACs from these raw materials for application as supercapacitor electrodes [5-24]. The biomass wastes employed have mostly been lignocellulosic, although other types of material such as algae (composed of proteins and carbohydrates) have been used. Table 1 summarizes the electrochemical characteristics of these ACs, which were all prepared by chemical activation, mainly by KOH [25].

Melia Azedarach (MA), also known as Chinaberry, is a widely planted urban ornamental tree in many Mediterranean countries because of the large shadow it casts in the summer and its carbon sink potential [26]. We investigated the usefulness of MA stones to obtain ACs for application as supercapacitor electrodes, preparing three AC series (MA, CMA and HMA) by KOH activation. The ACs obtained were characterized to determine their morphology, composition, surface area, porosity, surface chemistry, and their electrochemical characteristics (in 3EC and 2EC with 1M H_2SO_4 as electrolyte).

Table 1. Electrochemical capacitance performances of activated carbons from biomass wastes

Biomass precursor	Activation	S_{BET} (m^2 g^{-1})	Capacitances at 1 A g^{-1} (F g^{-1} or µF cm^{-2})	Energy density (Wh Kg^{-1}) at power density (kW kg^{-1})	Electrolyte	Ref
Lotus seedpods	KOH	1813	380 or 20.9	12.5 at 0.26	6M KOH	9
Eulaliopsis binata	KOH	2273	360 or 15.8	nd[a]	6M KOH	10
Cabbage leaves	KOH	3012	336 or 11.2	nd	2M KOH	11
Euonimus japonica leaves	KOH	1268	275 or 21.7	5.0 at 8.6	6M KOH	7
Willow catkins	KOH	1115	275 or 24.7	8.8 at 0.05	6M KOH	23

Dragon fruit skin	KOH	911	240 or 26.3	nd	2M KOH	13
Rapeseed	$ZnCl_2$	682	229 or 33.5	13.5 at 0.4[b]	6M KOH	14
Peanut shells	KOH	1277	228 or 17.9	6 at 0.8	6M KOH	8
Fir sawdust	KOH	2395	225 or 9.4	8.4 at 0.25	6M KOH	24
Soybean residue	KOH	1340	220 or 16.4	12 at 0.025	1M H_2SO_4	5
Enteromorpha prolifera	700 ºC (N_2 atm.)	422	216 or 51.2	nd	6M KOH	15
Chinese fir sawdust	KOH	2294	213 or 9.3	7.8 at 0.25	6M KOH	16
Momordica grosvenori skin	KOH	597	208 or 34.8	nd	2M KOH	13

Firmiana catkins	KOH	287	195 or 67.9	nd	2M KOH	13
Onion husks	K_2CO_3	2571	188 or 7.3	47.6 at 0.67	1 M $TEABF_4$/AN	17
Willow leaves	$ZnCl_2$	1031	172 or 16.7	nd	6M KOH	18
Hemp stem	KOH	2801	167 or 6.0	19.8 at 21	1.8 M $TEMABF_4$/PC	19
Bamboo shells	Na_2CO_3-K_2CO_3	843	164 or 19.5	nd	1M H_2SO_4	20
Rice husk	KOH	2696	120 or 4.5	5.1 at 0.05	6M KOH	21
Pine cones	KOH	1515	78 or 5.1	2.7 at 0.5	1M Na_2SO_4	22

[a] nd: non-determined; [b] in 0.5M Na_2SO_4

3. EXPERIMENTAL

3.1. Preparation of activated carbons

MA fruits were collected from trees on the campus of Granada University. After removal of the peel and pulp, the stones were washed with distilled water and dried at 110 ºC. Three series of ACs were prepared by KOH activation of MA, CMA, and HMA stones. The chemical activation of MA stones was carried out by drop-wise impregnation with a concentrated KOH solution under an infrared lamp (*ca.*70 ºC) to yield a KOH/raw material mass ratio between 1 and 4. The impregnated raw material was then dried and carbonized at 800 ºC for 1 h in a N_2 flow, followed by treatment with 1M HCl and washing with distilled water until the absence of chloride ions in the washing water; these ACs are designated as MAx, with x indicating the KOH/precursor mass ratio. CMA was prepared by carbonization of MA stones at 800 ºC for 1 h in a N_2 flow followed by KOH-activation as above; these ACs are designated as CMAx. HMA samples were prepared by heating a mixture of 50 g MA stones and 100 mL distilled water in a 250 mL Teflon-lined autoclave at 100 - 200 ºC for 24 h followed by KOH-activation as above; these ACs are designated as HMAt-x, with t being the treatment temperature. In all cases, KOH-activation of the precursors produced their breakdown, and the powdered ACs obtained were sieved to a size between 0.15 and 0.25 mm for utilization in all measurements.

3.2. Characterization

The morphology of samples was examined by environmental scanning electron microscopy (ESEM) FEI, model Quanta 400, equipment. Ultimate analysis (C, H, N and S) was carried out using an elemental analyzer Thermo Finnigan (1112 series). Ash content was determined by heating the sample at 800 ºC in air until constant weight using a Shimadzu thermobalance (model TGA-50H). N and O surface contents were determined by X-ray photoelectron spectroscopy (XPS) using an Escalab 200R system (VG Scientific Co.) equipped with MgK_{α} X-ray source ($h\upsilon$ = 1253.6 eV) and hemispherical electron analyzer. Each spectral region of photoelectron interest was scanned several times to obtain good signal-to-noise ratios. The C_{1s} peak at a binding energy (BE) of 284.6 eV was used as internal standard to obtain the number of components, position of peaks, and peak areas.

N_2 and CO_2 adsorption isotherms were measured at -196 and 0 ºC, respectively, using an Autosorb 1 from Quantachrome after outgassing samples overnight at 10^{-6} mbar and 110 ºC. BET equation was applied to the N_2 adsorption isotherm to obtain the surface area, S_{BET}, and the DR equation was applied to both isotherms to obtain the micropore volume, W_0, and micropore width, L_0. The total pore volume, $V_{0.95}$, was obtained from the amount of liquid N_2 adsorbed at p/p_0 = 0.95 and the percentage of micropores from $[W_0(N_2)/V_{0.95}]100$.

3.3. Electrochemical measurements

Electrochemical measurements were investigated at room temperature with 1M H_2SO_4 as electrolyte in both 2EC (Teflon-Swagelok-type) and 3EC. Working electrodes were prepared from a well-mixed slurry of the ACs (90 wt. %) with polytetrafluoroethylene (PTFE) emulsion (10 wt. %) as binder. This slurry was pressed at 3 bar on graphite paper disks (2EC) or graphite foil (3EC) and dried overnight in an oven at 120 ºC. The discs had an area of *ca*. 0.50 cm^2 (ϕ 8 mm) and contained the same amount of active material, *ca*. 4 mg, whereas the graphite foil contained *ca*. 20 mg of active material. Electrodes were immersed in the electrolyte for five days before their assembly in the cells. The 2EC was a symmetric device comprising two electrodes separated by a porous fibrous separator impregnated with the electrolyte solution. The 3ECs comprised the above slurry pasted on graphite paper as working electrode, with reference electrode (Ag/AgCl), and counter electrode (Pt wire).

Cyclic voltammetry (CV), GCD, and EIS measurements were done using a Biologic VMP-300 potentiostat. CVs and GCDs were performed in 2EC and 3EC in the 0-0.85 V range, at scan rates between 0.5 and 30 mV s^{-1} for CVs and current densities between 0.14 and 11.1 A g^{-1} for GCDs. EIS was carried out in 2EC within the frequency range of 1 mHz to 100 kHz with a sinusoidal signal amplitude of 10 mV.

Gravimetric capacitances, C (F/g), were obtained from the discharge curves of the GCDs by equation (1):

$$C = I_d \Delta t / m \Delta V \qquad (1)$$

where I_d is the discharge current, Δt the discharge time, m the total mass of the AC in the electrodes, and ΔV the voltage interval after the ohmic drop. The coulombic efficiency (%) was calculated from the discharge and charge time, t_d and t_c, respectively, by the formula $(t_d/t_c) \times 100$. The capacitance value from EIS, C, was obtained by equation (2):

$$C = -Z'' / 2\pi f |Z|^2 \qquad (2)$$

where f is the frequency and $|Z|^2 = Z'^2 + Z''^2$, with Z' and Z'' being the real and imaginary parts of the complex impedance, respectively.

For performance comparisons, the gravimetric capacitances in 2EC obtained from the above equations were multiplied by four to obtain the expression per single electrode, which is the 3EC equivalent [27]. However, *per convention,* the gravimetric capacitances obtained from equation (1) in 2EC, C_{2EC}, were used to calculate the energy density in the Ragone plot using the equation $E = C_{2EC} (\Delta V_d)^2 / 2$, where ΔV_d is the operation voltage taken as $\Delta V_d = V_{max} - IR_{drop}$. Power density was calculated from $P = E / \Delta t$ [28,29].

4. RESULTS AND DISCUSSION

ESEM images in Figures 1 and 2 reveal the morphology of precursors and ACs, respectively. The CMA precursor showed very large pores and channels (Figures 1a and b), generated by the evolution of the volatile matter during the carbonization of MA stones. Figures 1c-f depicts the precursors obtained by hydrothermal treatment of MA at different temperatures. Sample HMA200 was the only one that contained numerous sphere-like microparticles on the surface of some larger particles, generated during the hydrothermal treatment at 200 ºC of the saccharides contained in MA stones [5,30].

Morphologically, the ACs were composed of irregular, more or less divided particles, which contained large pores and conchoidal cavities caused by brittle fracture of the precursor particles during KOH activation.

The ash content and ultimate analysis of samples are displayed in Table 2. None of the samples contained sulfur. Notably, the ash content of MA stones was very low, considerably below that of other lignocellulosic waste biomasses used to prepare ACs [8,31]. This is important for the selection of potential wastes to prepare activated carbons [32]. The carbonization of MA to obtain CMA increased the ash and C content and reduced the other elements due to volatile matter removal.

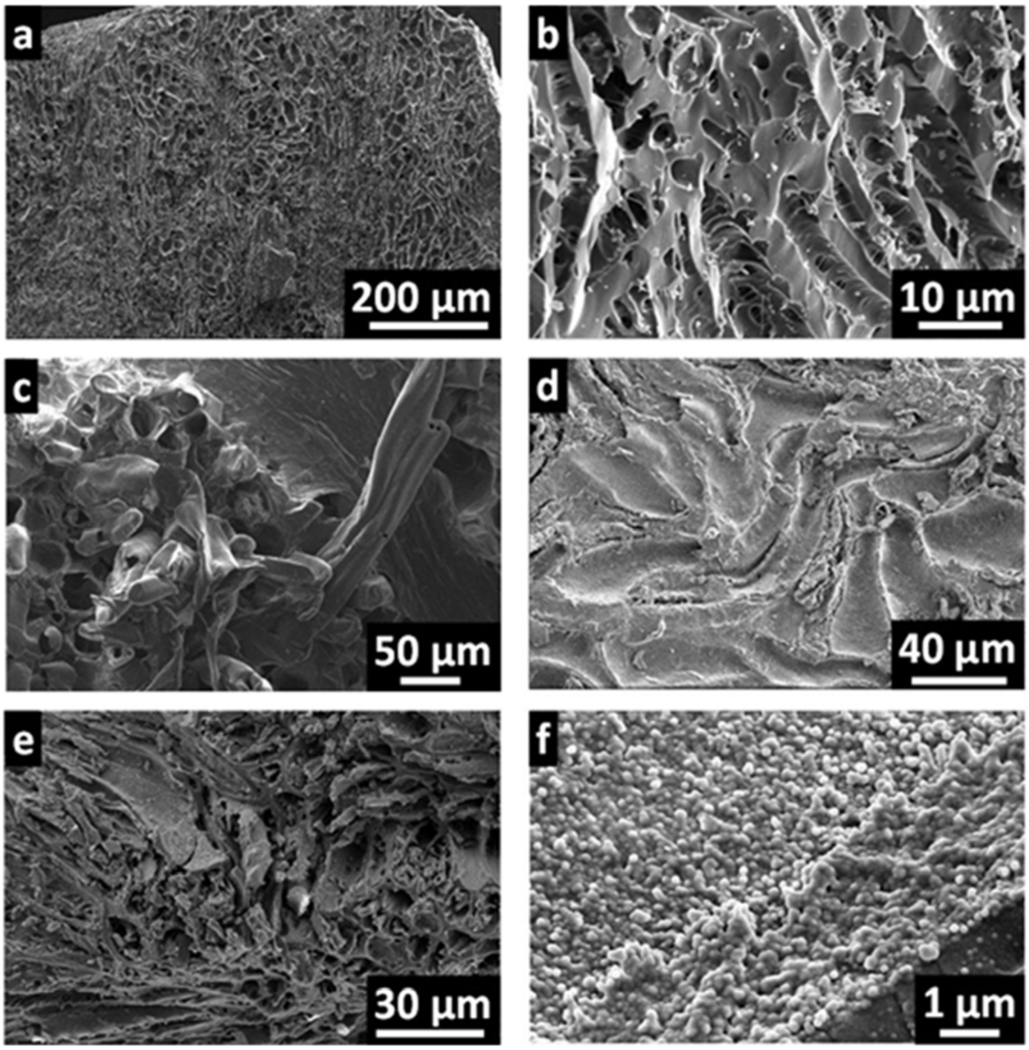

Figure 1. ESEM images of precursors: (a, b) CM; (c) HMA100; (d) HMA150; and (d, f) HMA200.

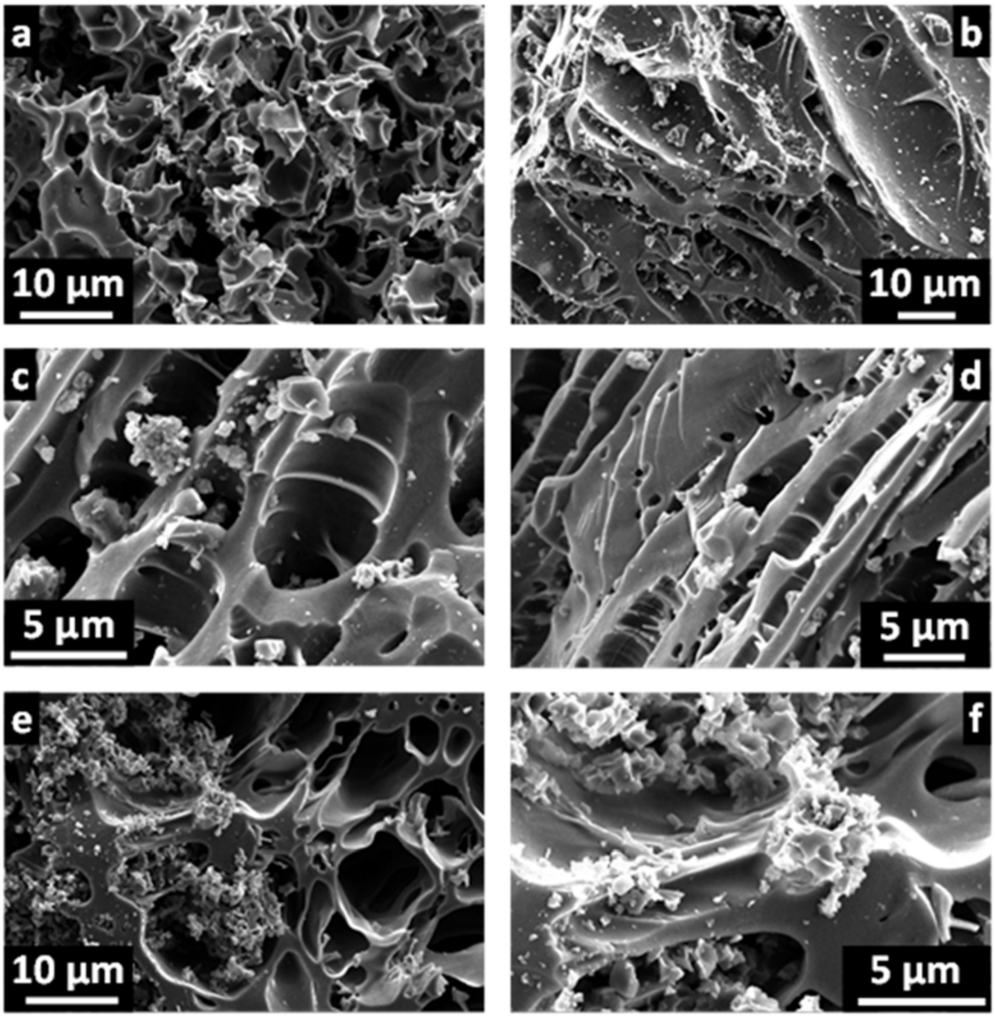

Figure 2. ESEM images of activated carbons: (a) MA2, (b) CMA2, (c) CMA4, (d) HMA100-2, (e) HMA150-2 and (f) HMA200-2.

Table 2. Ash content (%), ultimate analysis (wt. %) in dry basis, and N and O contents (wt. %) from XPS of the raw material, precursors and activated carbons

Sample	Ash	C	H	N	O [a]	N_{XPS}	O_{XPS}
MA	0.70	50.60	6.90	1.28	40.52	nd	nd
MA1	0.59	88.17	0.26	0.73	10.25	0.38	7.60
MA2	0.53	86.62	0.27	0.76	11.82	1.03	10.80
MA3	0.43	85.62	0.34	0.86	12.75	1.07	11.72
CMA	5.28	85.81	0.79	1.32	6.80	1.06	6.51
CMA2	2.36	85.37	0.28	0.44	11.55	0.32	8.43
CMA4	1.61	90.07	0.24	0.53	7.55	0.65	8.90
HMA100	0.62	53.58	7.46	1.38	36.96	nd	nd
HMA150	0.63	61.33	7.68	1.42	28.94	nd	nd
HMA200	0.63	68.17	7.94	1.73	21.53	nd	nd
HMA100-2	1.68	85.75	0.32	0.65	11.60	0.71	7.81
HMA150-2	1.42	88.26	0.20	0.70	9.42	0.85	10.44
HMA200-2	0.80	89.28	0.20	0.79	8.93	0.89	10.95

[a] by difference

The hydrothermal treatment of MA to obtain HMA produced a slight reduction in ash content and increase in C content with the rise in treatment temperature from 100 to 200 ºC. The ash content was lower in all ACs from the MA and CMA series than in their corresponding precursors because the activation included a final hydrochloric acid treatment to remove the potassium compounds formed. The ash content also decreased with higher KOH/precursor mass ratio or hydrothermal treatment temperature. The ash content was higher in ACs from the HMA series than in their respective precursors, despite the final HCl treatment, indicating that the inorganic compounds of the precursors were less accessible or reactive to this acid treatment after KOH activation. The influence of ash accessibility on its removal is indicated by the finding of a reduction in its content with higher hydrothermal treatment temperature of the precursor, because this increased the surface area of the ACs (*vide infra*). The lowest ash content was observed in ACs from the MA precursor.

N and O measured by ultimate analysis and XPS can be considered as the total and surface contents, respectively, giving an idea of their distribution in the ACs. With regard to the N content, N_{XPS} was higher than the total N content in the more highly activated samples (MA3 and CMA4) and in those receiving hydrothermal treatment. A similar trend was observed for the O content in the CMA4 sample. However, O_{XPS} was lower than total O in the MA3 sample and in HMA150-2 and HMA200-2 samples.

Figure 3 depicts the N_2 adsorption isotherms on the ACs, which were of Type I [33], typical of microporous solids; however, there was a slight increase in N_2 uptake with greater relative pressure after micropore filling, indicating the presence of mesopores below 4 nm in size [34]. N_2 and CO_2 adsorption isotherm results are compiled in Table 3.

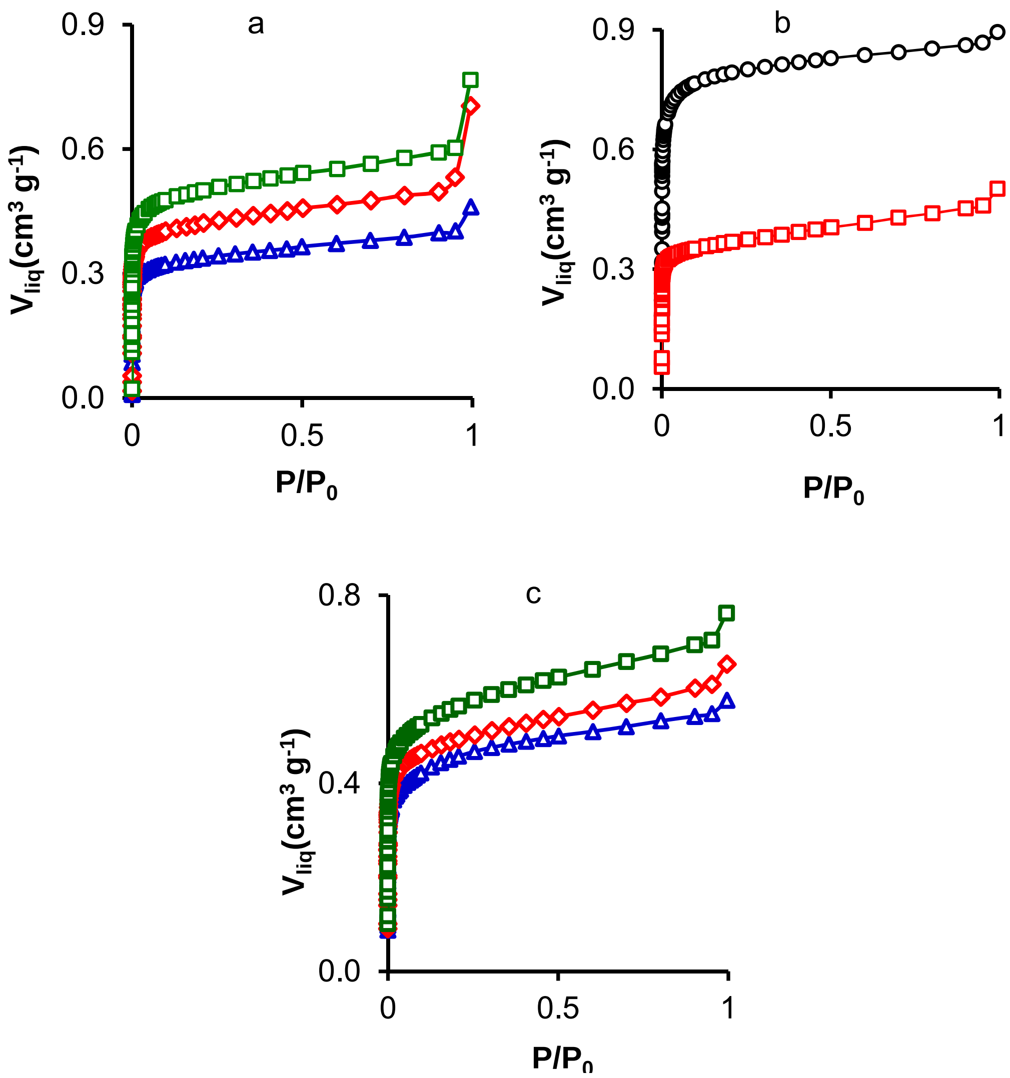

Figure 3. N_2 adsorption isotherms at –196 ºC of samples: (a) MA1 (△), MA2 (◇), and MA3 (□); (b) CMA2 (□), and CMA4 (○); and (c) HMA100-2 (△), HMA150-2 (◇), and HMA200-2 (□).

Table 3. Surface area and pore texture of the activated carbons

Sample	S_{BET}	$W_0(N_2)$	$W_0(CO_2)$	$L_0(N_2)$	$L_0(CO_2)$	$V_{0.95}$	Micro[a]
	$m^2\ g^{-1}$	$cm^3\ g^{-1}$	$cm^3\ g^{-1}$	nm	nm	$cm^3\ g^{-1}$	%
MA1	829	0.32	0.41	0.80	0.63	0.40	80
MA2	1032	0.41	0.44	0.89	0.73	0.50	82
MA3	1234	0.50	0.41	0.94	0.72	0.60	83
CMA2	969	0.37	0.46	0.45	0.71	0.44	84
CMA4	1975	0.76	0.53	0.79	0.74	0.87	87
HMA100-2	1069	0.40	0.32	0.91	0.56	0.55	73
HMA150-2	1154	0.45	0.44	0.85	0.69	0.62	73
HMA200-2	1317	0.51	0.43	0.83	0.71	0.70	73

[a] Micropores (%) = $[W_0(N_2)/V_{0.95}]100$

The surface area, $W_0(N_2)$, and $V_{0.95}$ increased with higher KOH/precursor mass ratio or hydrothermal treatment temperature of MA, while the CMA4 sample showed the highest S_{BET} value (*ca*. 2000 $m^2\ g^{-1}$). CO_2 adsorption at 0 ºC yielded the volume of narrow micropores (below approximately 0.7 nm in width), while N_2 adsorption at –196 ºC gave the total micropore volume if there were no micropores that were very narrow or had constricted entrances [35,36]. Table 3 shows that $W_0(N_2) < W_0(CO_2)$ for ACs obtained with lower KOH/precursor mass ratios, attributable to the presence in these samples of very narrow micropores or micropore constrictions. However, they were widened or the constrictions disappeared at KOH/precursor mass ratios > 2. $W_0(N_2) > W_0(CO_2)$ for all ACs in the HMA series. ACs in the MA and CMA series were more microporous (between 80-87 %) in comparison to ACs in the HMA series (73 %).

CVs at 2.5 mV s^{-1} obtained in 3EC and 2EC are depicted in Figures 4 and 5. CVs obtained with 3EC are very useful for analyzing faradic reactions and voltages at a single surface [37,38]. Thus, they had a quasi-rectangular shape, with a clear faradic hump at cell potential below around 0.4 V, indicating the presence of pseudocapacitance phenomena attributed to the oxygen and nitrogen functionalities [5] contained by all ACs under study. However, CVs in 2EC showed rectangular shapes, with no pseudocapacitance effects.

CVs in 2EC and 3EC showed that voltammograms retained a rectangular-like shape and their capacitance decreased with an increase in the scan rate (Figures 6-8), attributable to the inaccessibility of the internal surface of narrower micropores at high scan rates due to ion diffusion [39]. The pseudocapacitance effects observed in 3EC also disappeared at higher scan rates.

GCDs in 2EC and 3EC at 1 A g^{-1} (Figure 9) showed a triangular shape, and their gravimetric and areal capacitances are exhibited in Table 4. Values were always lower in 2EC than in 3EC, as previously reported at low current densities [37]. The gravimetric capacitance increased with higher KOH/precursor mass ratio in the MA and CMA series due to the resulting increase in surface area and porosity. In samples from the HMA series, C increased with a rise in the hydrothermal treatment temperature from 100 to 150 ºC but was not affected by a further rise up to 200 ºC.

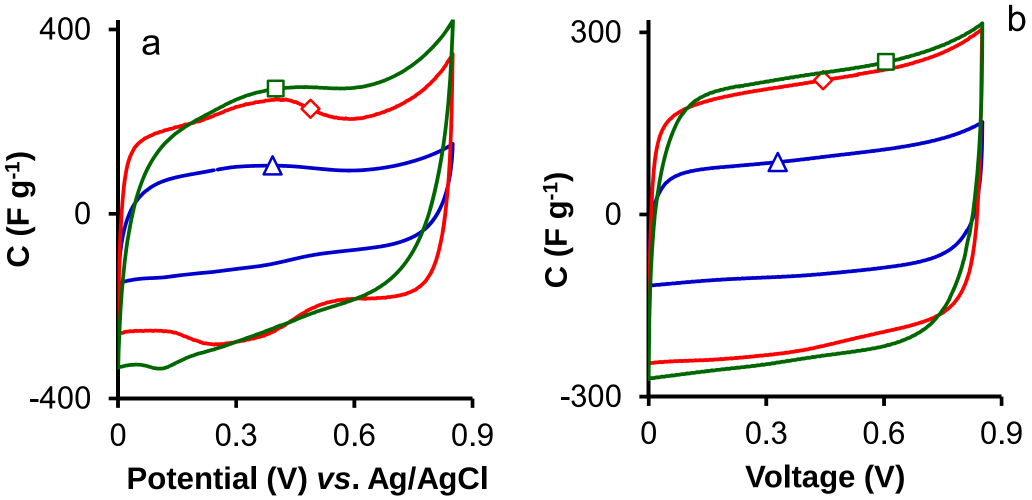

Figure 4. CVs at 2.5 mV s^{-1} of samples: (a, b) MA1 (△), MA2 (□), and MA3 (◇). a) three electrodes cell, b) two electrodes cell.

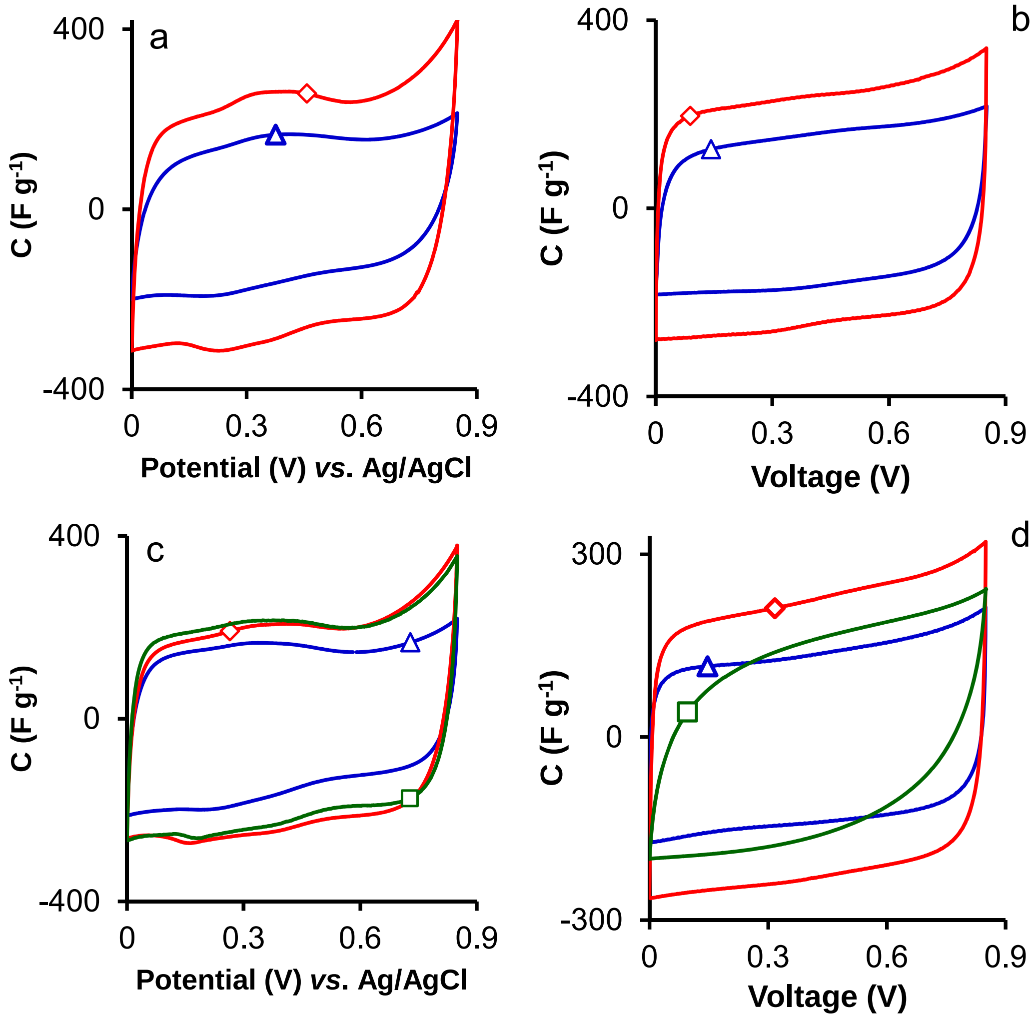

Figure 5. CVs at 2.5 mV s^{-1} of samples (a, b) CMA2 (△), and CMA4 (◇); and (c, d) HMA100-2 (△), HMA150-2 (□), and HMA200-2 (◇).a, c) three electrodes cell, b, d) two electrodes cell.

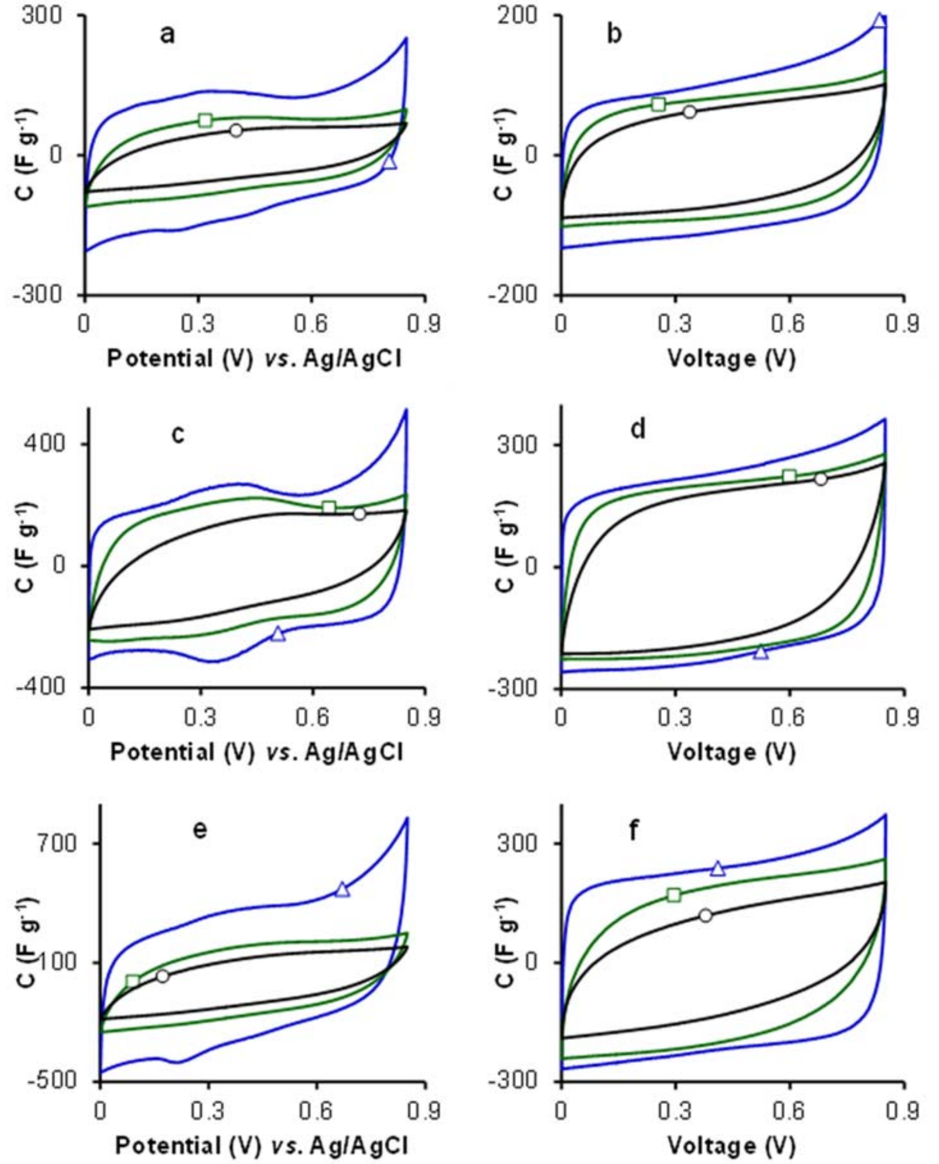

Figure 6. CVs at 0.5 (△), 10 (□), and 30 (○) mV s-1 of samples: (a, b) MA1; (c, d) MA2; and (e, f) MA3.

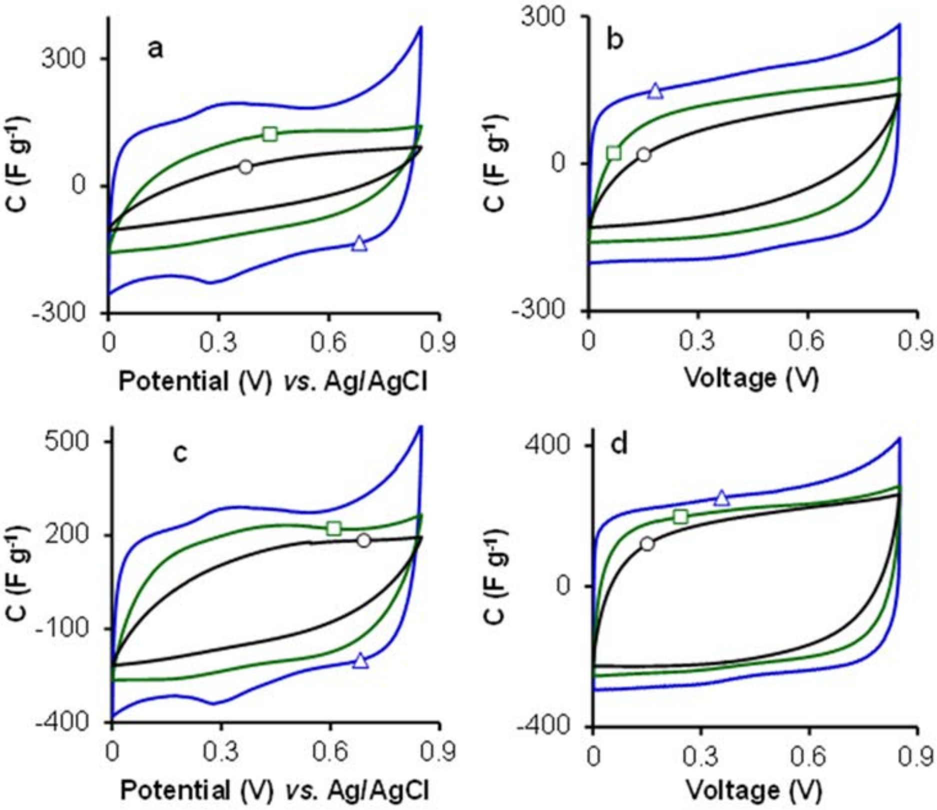

Figure 7. CVs at 0.5 (△), 10 (□), and 30 (○) mV s-1 of samples: (a, b) CMA2; and (c, d) CMA4.

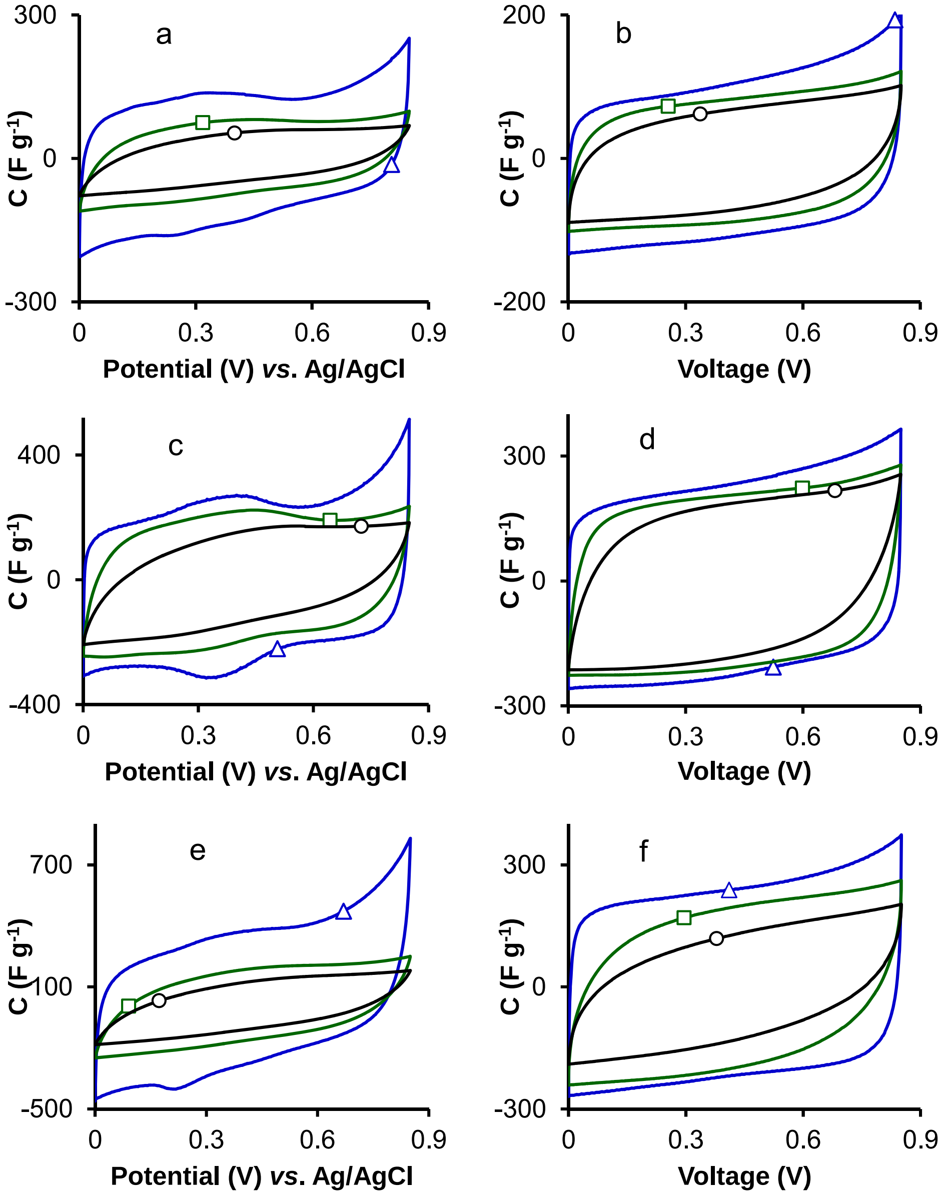

Figure 8. CVs at 0.5 (△), 10 (□), and 30 (○) mV s^{-1} of samples: (a, b) HMA100-2; (c, d) HMA150-2; and (e, f) HMA200-2.

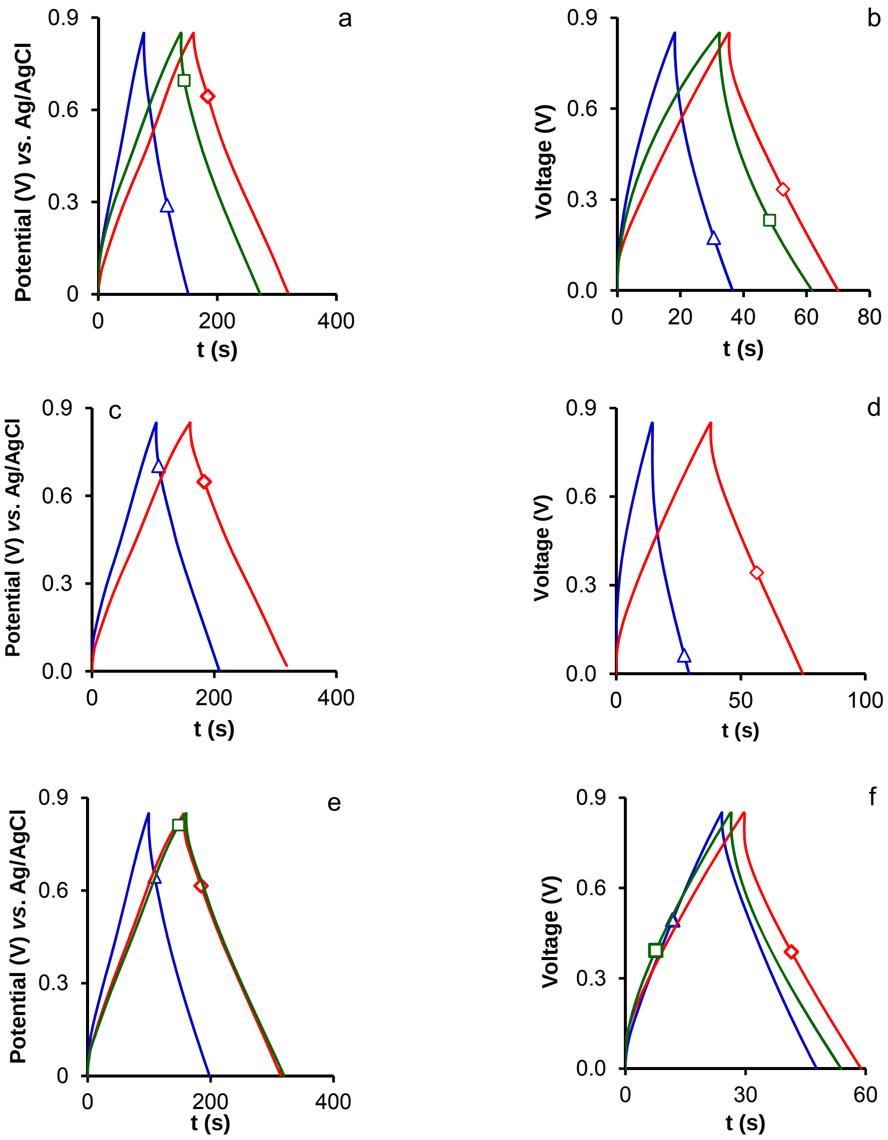

Figure 9. GCDs at 1 A g^{-1} of samples: (a, b) MA1 (△), MA2 (□), and MA3 (c, d) CMA2 (△), and CMA4 (◇); and (e, f) HMA100-2 (△), HMA150-2 (□), and HMA200-2 (◇).

Table 4. Capacitances from GCDs in 2 and 3EC at 1 A g^{-1}. C_{max} at 1 mHz, equivalent series resistance (ESR), charge transfer resistance (R_{CT}) and relaxation time constant (τ) from EIS in 2EC

Sample	3EC	2EC					
	C	C	C_A	C_{max}	ESR	R_{CT}	τ
	F g^{-1}	F g^{-1}	μF cm^{-2}	F g^{-1}	Ω	Ω	s
MA1	149	140	16.9	117	0.41	0.74	1.98
MA2	244	232	22.5	236	0.41	0.71	1.48
MA3	246	240	19.4	235	0.32	0.67	1.11
CMA2	178	131	13.5	159	0.50	2.39	1.48
CMA4	257	240	12.2	261	0.40	2.11	1.11
HMA100-2	185	157	14.7	169	0.52	1.74	1.48
HMA150-2	260	207	17.9	227	0.44	2.08	1.48
HMA200-2	256	202	15.3	205	0.32	1.53	0.83

MA2, MA3 and CMA4 samples, Table 4, showed similar C values in 2EC, in the 232-240 F g^{-1} range. This was the higher capacitance obtained in the present study and was within the range reported for the top six ACs (229-380 F g^{-1} at 1 A g^{-1}) compiled in Table 1. The coulombic efficiency in all cases was 100 % at 1 A g^{-1} and it decreased up to ~ 97 % at the higher current density due to the cell resistance. Although the gravimetric capacitance of these three samples was similar, their areal capacitance, C_A, was very different, attributable to the pseudocapacitance effects of their N and O contents. Thus, the C_A value was considerably higher for MA2 (22.5

μF cm^{-2}) than for CMA4 (12.2 μF cm^{-2}), which was the AC with the lowest N and O contents of these three samples. Gravimetric capacitance decreased with higher current density increased (Figure 10), and the retention capacitance at 11.1 A g^{-1} was 26, 21 and 32 %, for MA2, MA3, and CMA4 samples, respectively.

EIS measurements were performed to investigate the charge kinetic properties of the ACs towards the capacitive behavior. Figure 11 depicts the Nyquist plots, showing that all samples exhibited typical characteristics of porous carbon electrodes [15,21,22,40]. In the high frequency region, the first intersection point on the real axis (Z') was the ESR, which was related to three resistances: the intrinsic resistance of the active material, the electrolyte resistance, and the active material/current collector interface. Results, shown in Table 4, can be considered to approximately reflect the conductive properties of the activated carbon electrodes for comparison purposes, because the same electrolyte, collectors, and technique were used to assemble the cell [41]. ESR values were very low, ranging between ~ 0.3 and 0.5 Ω, and they tended to decrease with higher KOH/precursor mass ratio or hydrothermal temperature. Thus, the lowest ESR values in the AC series were 0.32 Ω (MA3 and HMA200-2) and 0.40 (CMA4).

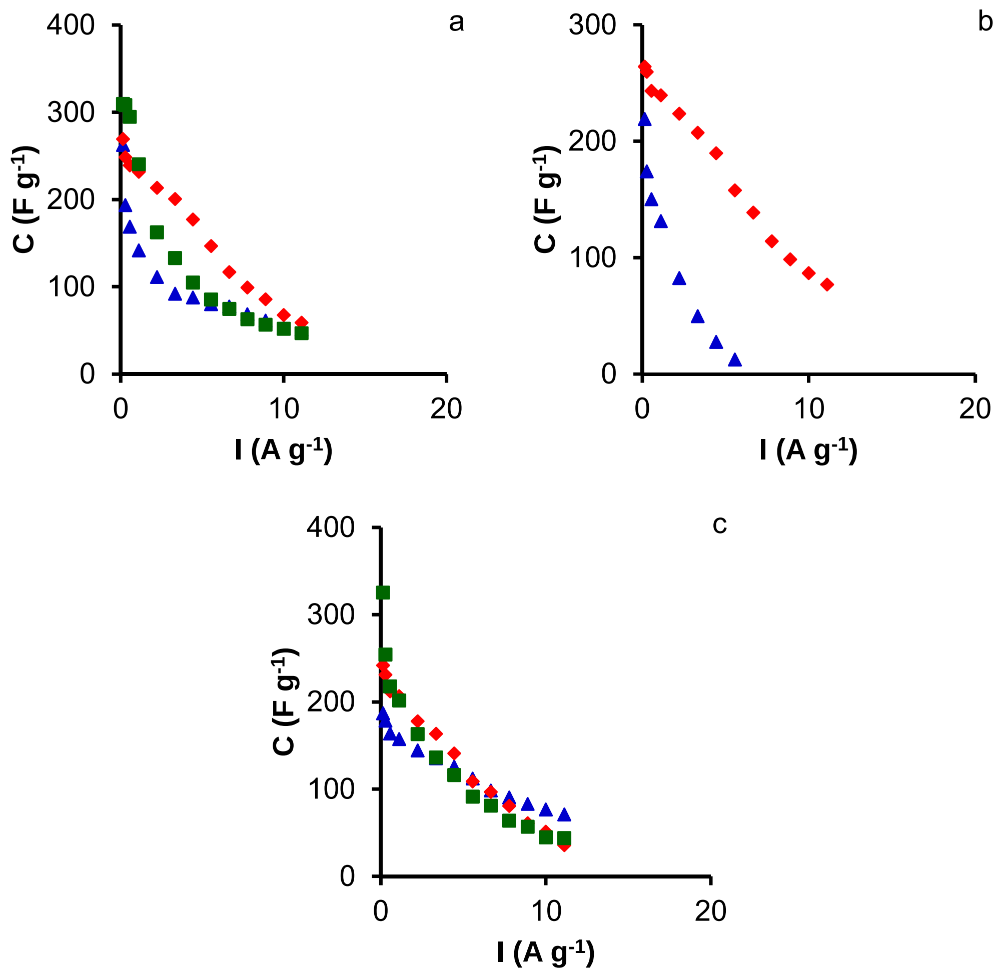

Figure 10. Variation of gravimetric capacitance with current density: (a) MA1 (▲), MA2 (◆) and MA3 (■); (b) CMA2 (▲) and CMA4 (◆); and (c) HMA100-2 (▲), HMA150-2 (◆) and HMA200-2 (■).

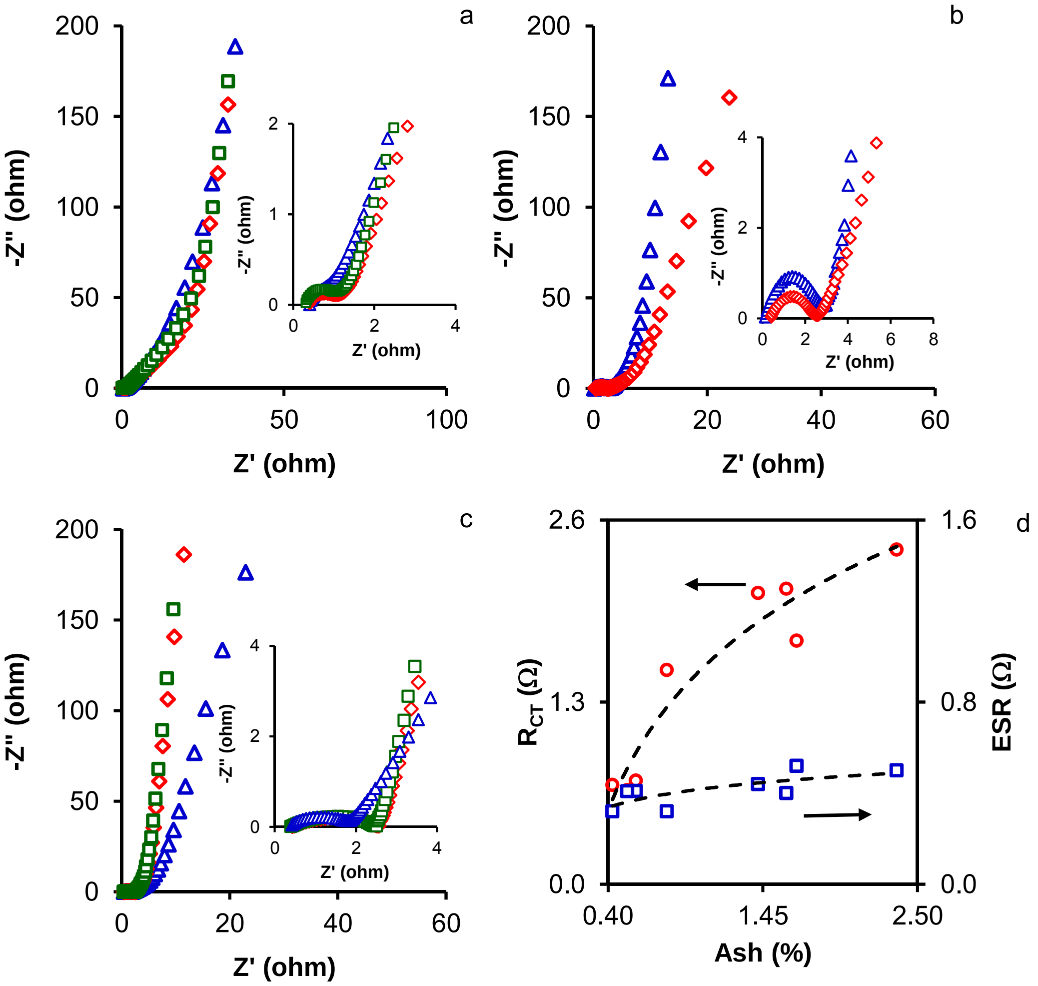

Figure 11. Nyquist plots of samples: (a) MA1 (△) MA2 (◇) and MA3 (□); (b) CMA2 (△) and CMA4 (◇) and (c) HMA100-2 (△), HMA150-2 (◇) and HMA200-2 (□). (d) Relationship between ESR (□) and R_{CT}(○) with ash content of the activated carbons.

In the high-medium frequency region, a semicircle loop was observed in association with charge transfer processes, indicating the presence of pseudocapacitance phenomena, which were also detected in the CVs in 3EC (*vide supra*) due to the N and O functionalities on the AC surfaces [5,23]. The interfacial charge transfer resistance, R_{CT}, caused by EDL capacitance and faradic reactions was estimated from the two intercepts of the semicircle with the real axis (semicircle diameter) [15], and the values obtained are displayed in Table 4. R_{CT} values were lower in ACs from the MA series than from the other two series. The lowest R_{CT} values were found in the most highly activated AC in each series (MA3, CMA4 and HMA200-2) due to their increased surface area and micropore volume, which enhanced the accessibility of ions to the electrode porosity and the charge transfer.

Notably, both ESR and R_{CT} tended to decrease with lower ash content of the ACs (Fig. 11d). This was due to a decrease in interparticle contact resistance, which facilitated electron mobility through the carbon electrode (ESR), and to a widening of the porosity, which increased the accessibility of the electrolyte to the microporosity (R_{CT}) when the ash content was reduced.

In the low frequency region, the imaginary part of the impedance (Z") sharply increased and the plots tended to a vertical line, which is characteristic of capacitive behavior. The maximum capacitance (C_{max}) of the ACs was obtained at the lowest frequency (1 mHz) using equation (2). Results in Table 4 showed that C_{max} was similar or close to the C values yielded by GCD measurements in 2EC. Variations in the imaginary part of the capacitance (C") against the frequency (Figure 12) define the transition frequency between a pure capacitive and a pure resistive behavior. The relaxation time constant (τ) can be obtained from the frequency, f_0, at the maximum of these curves by the equation $\tau = \frac{1}{2}\pi f_0$ [24]. The relaxation time constant is a quantitative measure of the speed with which the device can be discharged [38]. Results in Table 4 show that τ generally decreased with higher activation in each AC series.

The Ragone plots of the ACs are displayed in Figure 13 and reveal the dependence between energy and power densities. The maximum energy density was released at the lowest power density (110 W kg^{-1}), as shown in Table 5. The maximum energy density increased with higher activation in each AC series, attributable to the increase in surface area and micropore volume produced.

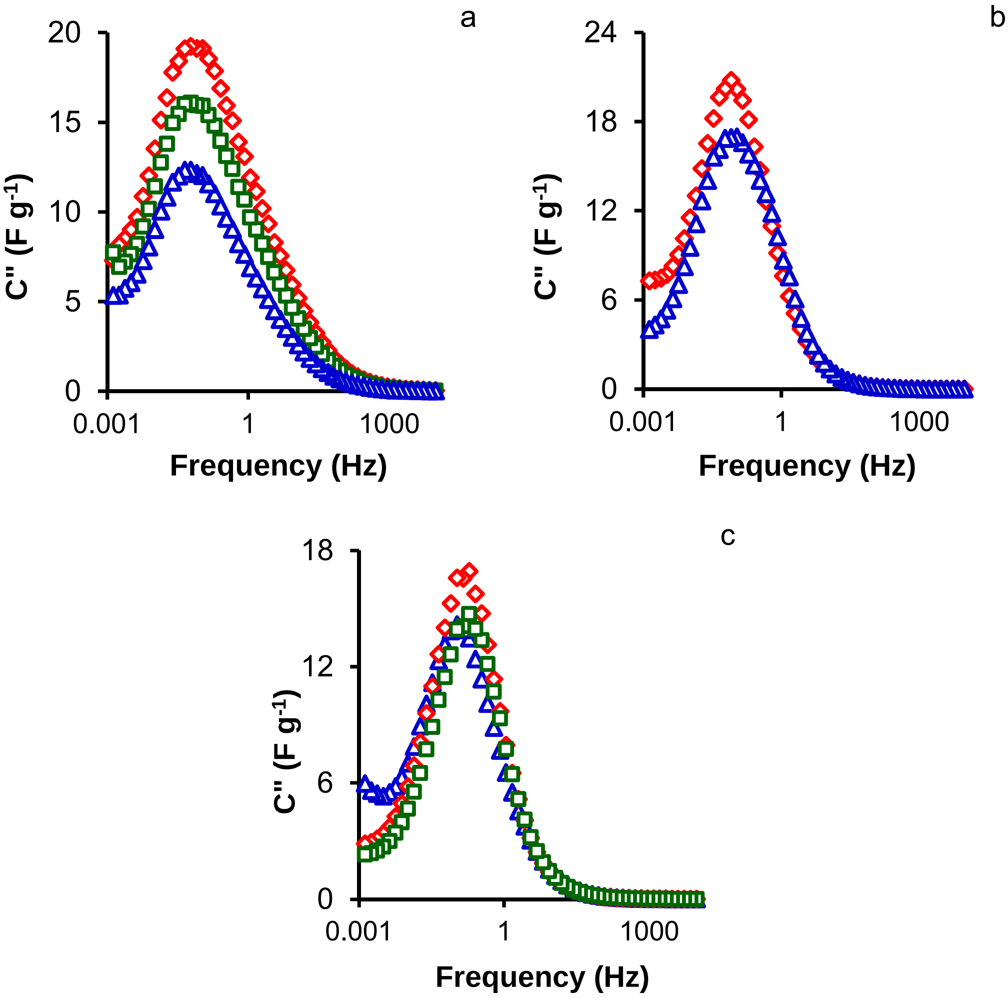

Figure 12. Evolution of imaginary part of capacitance *vs*. frequency. (a) MA1 (△), MA2 (□), and MA3 (◇); (b) CMA2 (△), and CMA4 (◇); and (c) HMA100-2 (△), HMA150-2 (□), and HMA200-2 (◇).

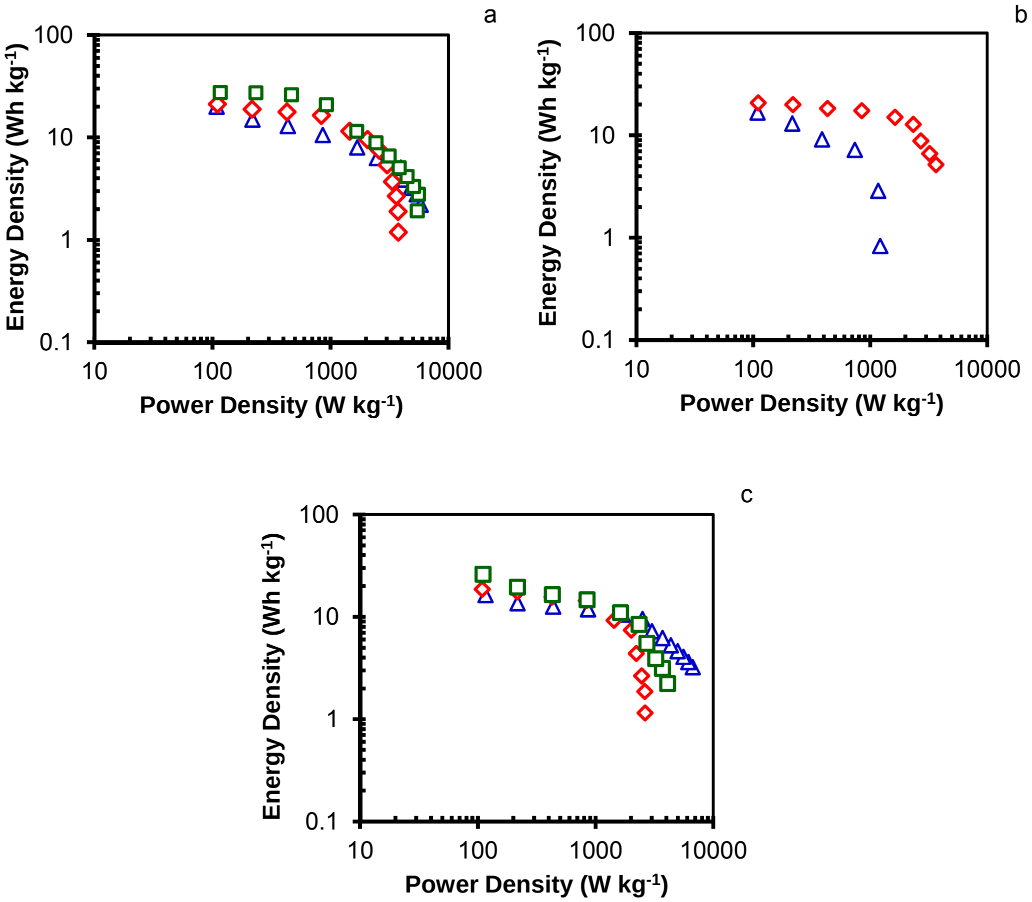

Figure 13. Ragone plots of samples: (a) MA1 (△), MA2 (◇) and MA3 (□) (b) CMA2 (△) and CMA4 (◇) and (c) HMA100-2 (△), HMA150-2 (◇), and HMA200-2 (□).

Table 5. Energy density (Wh Kg^{-1}) at 110 W kg^{-1} from Ragone's plots

Sample	Energy density
MA1	20.0
MA2	21.2
MA3	27.4
CMA2	16.7
CMA4	20.8
HMA100-2	16.3
HMA150-2	18.6
HMA200-2	26.1

The maximum value reached was 27.4 Wh kg^{-1} for sample MA3. Notably, the energy density of the symmetrical capacitor based on MA3 was better than that reported for most of the commercially available supercapacitors (less than 10 Wh kg^{-1}) [42] and most of the recently reported ACs derived from biomass wastes (Table 1). The energy released decreased at higher power density (Figure 13); thus, the energy densities of MA3, CMA4, and HMA200-2 samples were decreased to 2.8, 3.6, and 2.2 Wh kg^{-1} at power densities of ~ 5.6, 3.6, and 4.1 kW kg^{-1}, respectively.

The long-term stability of AC-based symmetric supercapacitors is considered a key factor for their practical application. This stability was evaluated by the voltage-holding or floating test, which was recently established [22,43-45] as a reliable alternative to the traditional method of GCD cycles at constant current density over several thousands of cycles. The floating test was carried out by applying a critical voltage cell (0.85 V), and by occasionally cycling the cell between 0.85 and 0 V at a constant current density of 1 A g^{-1}, determining the respective capacitance and the resistance from the IR voltage drop. During the voltage-holding procedure, three cycles were applied every 10 h [45] and this sequence was repeated 20 times, giving a total floating time of 200 h.

Figure 14 depicts the results of the floating test for samples from the three series that showed the higher capacitance and energy release (MA2, MA3, CMA4 and HMA200-2). The capacitance of MA2 and MA3 (Fig. 6a) did not change during ~ 50 h of voltage-holding and subsequently started to decrease, showing a capacitance decay of 8 % (MA2) and 6 % (MA3) after 200 h of floating time. The resistance was practically constant throughout this time. In CMA4 and HMA200-2 samples (Fig. 6b), the capacitance was constant up to ~ 100 h of voltage-holding, showing a capacitance decay of 1 and 2 %, respectively, after 200 h. In CMA4, the resistance slightly increased after 100 h, indicating a slight degradation of the electrodes. The results for these ACs indicated their good stability as potential supercapacitor electrodes, especially in the case of CMA4.

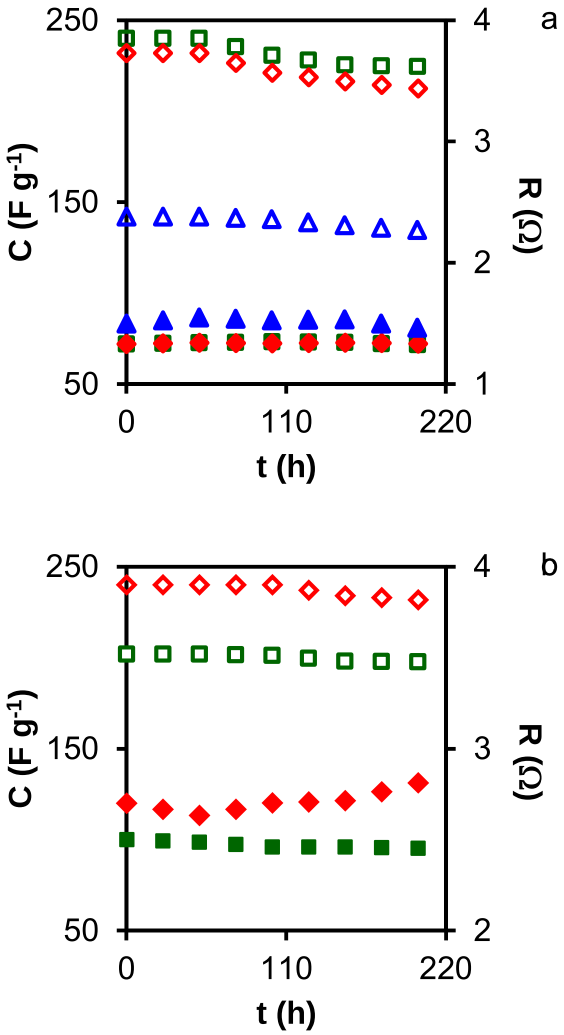

Figure 14. Floating tests of samples: (a) MA2 (△), and MA3 (□); (b) CMA4 (◇), and HCM200-2 (□). Gravimetric capacitance (open symbols) and resistance (closed symbols).

5. CONCLUSIONS

In this study, three series of ACs were prepared by KOH activation of *Melia Azedarach* (MA) stones (MA series), carbonized MA stones (CMA series) and hydrothermally-treated MA stones (HMA series). MA stones had very low ash content, 0.7 %, which is of great importance for AC preparation. ACs from MA series showed the lower ash content (0.43-0.59 %). ACs from the three series contained different amounts of N and O functionalities. The highest surface area obtained was *ca*. 2000 m^2 g^{-1} (CMA4). ACs from HMA series had a lower percentage of microporosity than those from the other two series. The higher gravimetric capacitance was in the 232-240 F g^{-1} range at 1 A g^{-1}, and sample MA2 showed the highest areal capacitance 22.5 μF cm^{-2}. CVs in 3EC and EIS in 2EC showed pseudocapacitance phenomena attributed to the N and O functionalities. Notably, the ESR and R_{CT} tended to decrease when the ash content of the AC electrode decreased, which indicated the importance of controlling the mineral content of the raw material used to prepare ACs for supercapacitor applications. The maximum energy density reached (MA3) was 27.4 Wh kg^{-1} at a power density of 110 W kg^{-1}. Cycling test based on floating were used to investigate the long-term stability and results showed that devices could be charged and discharged without notable degradation. Electrochemical performance of MA stone-derived ACs was compared with that of other ACs described in the recent literature that were prepared from different biomass wastes, mainly of lignocellulosic and algae origin, and results showed that they are among the best ACs for supercapacitor applications.

6. REFERENCES

[1] B.E. Conway, Electrochemical supercapacitors. Scientific fundamentals and technological applications, Kluwer Academic/Plenum, New York, 1999.

[2] L.L. Zhang, X.S. Zhao, Carbon-based materials as supercapacitor electrodes, Chem. Soc. Rev. 38 (2009) 2520-2531.

[3] F. Béguin, V. Presser, A. Balducci, E. Frackowiak, Carbons and electrolytes for advanced supercapacitors, Adv. Mater. 26 (2014) 2219-225.

[4] C. Moreno-Castilla, M. B. Dawidziuk, F. Carrasco-Marín, E. Morallón, Electrochemical performance of carbon gels with variable surface chemistry and physics, Carbon 50 (2012) 3324-3332.

[5] G.A. Ferrero, A.B. Fuertes, M. Sevilla, From soybean residue to advanced supercapacitors, Sci. Rep. 5 (2015) 16618.

[6] A.M. Abioye, F.N. Ani, Recent development in the production of activated carbon electrodes from agricultural waste biomass for supercapacitors: A review, Renew. Sustain. Energy Rev. 52 (2015) 1282-1293.

[7] L. Zhu, Q. Gao, Y. Tan, W. Tian, J. Xu, K. Yang, C. Yang, Nitrogen and oxygen co-doped microporous carbons derived from the leaves of *Euonymus japonicas* as high performance supercapacitor electrode material, Micropor. Mesopor. Mat. 210 (2015) 1-9.

[8] M-b. Wu, R-c. Li, X-j. He, H-b. Zhang, W-b. Sui, M-h. Tan, Microwave-assisted preparation of peanut shell-based activated carbons and their use in electrochemical capacitors, New Carbon Mate. 30 (2015) 86-91.

[9] B. Liu, X. Zhou, H. Chen, Y. Liu, H. Li, Promising porous carbons derived from lotus seedpods with outstanding supercapacitance performance, Electrochim. Acta 208 (2016) 55-63.

[10] B. Liu, H. Chen, Y. Gao, H. Li, Preparation and capacitive performance of porous carbon materials derived from eulaliopsis binata, Electrochim. Acta 189 (2016) 93-100.

[11] P. Wang, Q. Wang, G. Zhang, H. Jiao, X. Deng, L. Liu, Promising activated carbons derived from cabbage leaves and their application in high-performance supercapacitors electrodes. J. Solid State Electrochem. 20 (2016) 319-325.

[12] K. Wang, R. Yan, N. Zhao, X. Tian, X. Li, S. Lei, Y. Song, Q. Guo, L. Liu, Bio-inspired hollow activated carbon microtubes derived from willow catkins for supercapacitors with high volumetric performance, Mater. Lett. 174 (2016) 249-252.

[13] W. Feng, P. He, S. Ding, G. Zhang, M .He, F. Dong, J. Wen, L. Du, M. Liu, Oxygen-doped activated carbons derived from three kinds of biomass: preparation, characterization and performance as electrode materials for supercapacitors, RSC Adv. 6 (2016) 5949-5956.

[14] K. Sun, D. Guo, Nitrogen-doped porous carbon derived from rapeseed residues, Int. J. Electrochem. Sci. 11 (2016) 4743-4754.

[15] Z. Tian, M. Xiang, J. Zhou, L. Hu, J. Cai, Nitrogen and oxygen-doped hierarchical porous carbons from algae biomass: direct carbonization and excellent electrochemical properties, Electrochim. Acta 211 (2016) 225-233.

[16] Y. Huang, L. Peng, Y. Liu, G. Zhao, J.Y. Chen, G. Yu, Biobased nano porous active carbon fibers for high-performance supercapacitors, ACS Appl. Mater. Interfaces 8 (2016) 15205-15215.

[17] D. Wang, S. Liu, G. Fang, G. Geng, J. Ma, From trash to treasure: Direct transformation of onion husks into three-dimensional interconnected porous carbon frameworks for high-performance supercapacitors in organic electrolyte, Electrochim. Acta, 216 (2016) 405-411.

[18] Y. Liu, Y. Wang, G. Zhang, W. Liu, D. Wang, Y. Dong, Preparation of activated carbon from willow leaves and evaluation in electric double-layer capacitors, Mater. Lett. 176 (2016) 60-63.

[19] W. Sun, S.M. Lipka, C. Swartz, D. Williams, F. Yang, Hemp-derived activated carbons for supercapacitors, Carbon 103 (2016) 181-192.

[20] B .Lu, L. Hu, H. Yin, X .Mao, W. Xiao, D. Wang, Preparation and application of capacitive carbon from bamboo shells by one step

molten carbonates carbonization, Int. J. Hydrogen Energy 41 (2016) 18713-18720.

[21] E.Y.L. Teo, L. Muniandy, E.P. Ng, F. Adam, A.R. Mohamed, R. Jose, K.F. Chong, High surface area activated carbon from rice husk as a high performance supercapacitor electrode, Electrochim. Acta 192 (2016) 110-119.

[22] N. Manyala, A. Bello, F. Barzegar, A.A. Khaleed, D.Y. Momodu, J.K. Dangbegnon, Coniferous pine biomass: A novel insight into sustainable carbon materials for supercapacitors electrode, Mater. Chem. Phys. 182 (2016) 139-147.

[23] K. Wang, Y. Song, R. Yan, N. Zhao, X. Tian, X. Li, Q. Guo, Z. Liu, High capacitive performance of hollow activated carbon fibers derived from willow catkins, Appl. Surf. Sci. 394 (2017) 569-577.

[24] Y. Huang, Y. Liu, G. Zhao, J.Y. Chen, Sustainable activated carbon fiber from sawdust by reactivation for high-performance supercapacitors, J. Mater. Sci. 52 (2017) 478-488.

[25] A. Linares-Solano, D. Lozano-Castelló, M.A. Lillo-Ródenas, D. Cazorla-Amorós, Carbon activation by alkaline hydroxides: Preparation and reactions, porosity and performance, in: L.R. Radovic (Ed.), Chemistry and Physics of Carbon, Vol. 30, Ch. 1, CRC Press, Boca Raton, FL, 2008, p. 1.

[26] Y.C. Wang, J.C. Lin, Air quality enhancement zones in Taiwan: A carbon reduction benefit assessment, Forest Policy Econ. 23 (2012) 40-45.

[27] T.E. Rufford, D. Hulicova-Jurcakova, E. Fiset, Z. Zhu, G.Q. Lu, Double-layer capacitance of waste coffee ground activated carbons in an organic electrolyte, Electrochem. Commun. 11 (2009) 974-977.

[28] G.A. Ferrero, A.B. Fuertes, M. Sevilla, N-doped microporous carbon microspheres for high volumetric performance supercapacitors, Electrochim. Acta 168 (2015) 320-329.

[29] T. Liang, C. Chen, X. Li, J. Zhang, Popcorn-derived porous carbon for energy storage and CO_2 capture, Langmuir 32 (2016) 8042-8049.

[30] M.M. Titirici, M. Antonietti, N. Baccile, Hydrothermal carbon from biomass: a comparison of the local structure from poly- to monosaccharides and pentoses/hexoses, Green Chem. 10 (2008) 1204-1212.

[31] M.A. Yahya, Z. Al Qodah, C.W.Z. Ngah, Agricultural bio-waste materials as potential sustainable precursors used for activated carbon production: A review, Renew. Sustain. Energy Rev. 46 (2015) 218-235.

[32] F. Rodríguez-Reinoso, Activated carbon: Structure, characterization, preparation and applications, in: H. Marsh, E.A. Heintz, F. Rodríguez-

Reinoso (Eds), Introduction to Carbon Technologies, Ch. 2, University of Alicante, Spain, 1997.

[33] M. Thommes, K. Kaneko, A.V. Neimark, J.P. Olivier, F. Rodríguez-Reinoso, J. Rouquerol, K.S.W. Sing, Physisorption of gases, with special reference to the evaluation of surface area and pore size distribution (IUPAC technical report), Pure Appl. Chem. 87 (9-10) (2015) 1051-1069.

[34] Z. Zapata-Benabithe, F. Carrasco-Marín, J. de Vicente, C. Moreno-Castilla, Carbon xerogel microspheres and monoliths from resorcinol-formaldehyde mixtures with varying dilution ratios. Preparation, surface characteristics, and electrochemical double-layer capacitances, Langmuir 29 (2013) 6166-6173.

[35] F. Rodríguez-Reinoso, A. Linares-Solano, Microporous structure of activated carbons as revealed by adsorption methods, in: P.A. Thrower (Ed.), Chemistry and Physics of Carbon, Vol. 21, Ch. 1, Marcel Dekker, New York, 1989, p. 1.

[36] D. Cazorla-Amorós, J. Alcañiz-Monge, M.A. De la Casa-Lillo, A. Linares-Solano, CO_2 as an adsorptive to characterize carbon molecular sieves and activated carbons, Langmuir 14 (1998) 4589-4596.

[37] M.D. Stoller, R.S. Ruoff, Best practice methods for determining an electrode material's performance for ultracapacitors, Energy Environ. Sci. 3 (2010) 1294-1301.

[38] E. Raymundo-Piñero, F. Béguin, Application of nanotextured carbons for supercapacitors and hydrogen storage, in: T.J. Bandosz (Ed.), Activated Carbon Surfaces in Environmental Remediation, Elsevier, Oxford, UK, 2006, p 293.

[39] R. Kotz, M. Carlen, Principles and applications of electrochemical capacitors, Electrochim. Acta 45 (2000) 2483-2498.

[40] Y. Zhao, M. Liu, L. Gan, X. Ma, D. Zhu, Z. Xu, L. Chen, Ultramicroporous carbon nanoparticles for the high-performance electrical double-layer capacitor electrode, Energ. Fuel 28 (2013) 1561-1568.

[41] D. Hulicova, M. Kodama, H. Hatori, Electrochemical performance of nitrogen-enriched carbons in aqueous and non-aqueous supercapacitors, Chem. Mater. 18 (2006) 2318-2326.

[42] G. Wang, L. Zhang, J. Zhang, A review of electrode materials for electrochemical supercapacitors, Chem. Soc. Rev. 41 (2012) 797-828.

[43] P.W. Ruch, D. Cericola, A. Foelske-Schmitz, R. Kötz, A. Wokaun, Aging of electrochemical double layer capacitors with acetonitrile-based electrolyte at elevated voltages, Electrochim. Acta 55 (2010) 4412-4420.

[44] D. Weingarth, A. Foelske-Schmitz, R. Kötz, Cycle versus voltage hold – Which is the better stability test for electrochemical double layer capacitors?, J. Power Sources 225 (2013) 84-88.

[45] A. Bello, F. Barzegar, M.J. Madito, D.Y. Momodu, A.A. Khaleed, T.M. Masikhwa, J.K. Dangbegnon, N. Manyala, Stability studies of polypyrole- derived carbon based symmetric supercapacitor via potentiostatic floating test, Electrochim. Acta 213 (2016) 107-114.

CAPÍTULO VII

CHAPTER VII

SURFACE CHARACTERISTICS OF ACTIVATED CARBONS FROM KOH ACTIVATION OF *SCHINUS MOLLE* STONES AND OF THEIR CORRESPONDING HYDROCHARS

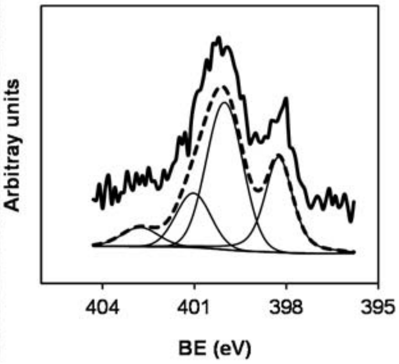

1. ABSTRACT

Activated carbons (ACs) in this work were prepared by KOH activation of *Schinus molle* (SM) stones, SM series, and of their corresponding hydrochars, HSM series. These hydrochars were prepared by hydrothermal carbonization (HTC) of SM stones between 100 and 200 ºC. ACs were characterized to know their surface chemistry, porosity, surface area and capacitance in two-electrode cell. The objective was to know the variations in the surface characteristics of the ACs introduced by the two methods of preparation and the KOH/precursor mass ratio. ACs from the HSM series had lower ash and higher N contents than those from the SM one. All ACs, except the most activated from the HSM series, showed narrow micropores or micropore constrictions at their entrances. The highest surface area and mesopore volume obtained were *ca*. 1500 m^2 g^{-1}, and 0.29 cm^3 g^{-1}, respectively. Results from porosity and surface area of the ACs indicated that the SM stones were more reactive to the KOH activation after their HTC. The higher gravimetric capacitance at 0.5 A g^{-1} was in the 227-235 F g^{-1} range, and it was obtained with ACs from the HSM series, similar to other ACs from different lignocellulosic materials.

Keywords: *Schinus Moll* seed; Biomass benefit; Activated carbons; Nitrogen surfaces groups; Energy storage.

2. INTRODUCTION

The preparation of ACs from lignocellulosic biomass residues for applications in adsorption and catalysis processes has been known since long ago [1-3]. However, there is recently a renewed interest in the preparation of ACs from these raw materials for new applications in energy storage and also in water remediation [4,5]. The classical method to prepare ACs was by physical or chemical activation of the pristine or carbonized raw material, being currently the KOH chemical activation one of the most used [6]. Today, a novel method to produce ACs and other functional carbon materials is by HTC of lignocellulosic biomass and carbohydrates [7-9]. This process is carried out by heating an aqueous solution or dispersion of the raw material in an autoclave at temperatures below 250 ºC. The hydrochar so obtained contains different functionalities but generally has no open porosity, which is one of the main drawbacks of HTC materials produced directly from either carbohydrates or biomass. Therefore for applications in adsorption, catalysis and energy storage they need to be activated [9-11].

Schinus molle is a widely planted ornamental tree in many Mediterranean countries, and in this work we have investigated the potential use of SM stones to prepare ACs. For this purpose, ACs were prepared by KOH activation of the pristine raw material (SM series) and of its hydrochars obtained by HTC between 100 and 200 ºC (series HSM). The surface chemistry, porosity, surface area and capacitance of both series of ACs were determined with the objective to know their variations with the method of preparation and the KOH/precursor mass ratio used.

3. EXPERIMENTAL

3.1. Preparation of activated carbons

SM stones were obtained from the fruits after removing their peels, pulps and stalks. Subsequently, they were dried at 110 ºC and then hydrothermally treated between 100 and 200 ºC for 1h. For this purpose, a mixture of 50 g of SM stones and 100 mL of distilled water were introduced in a 250 mL Teflon-lined autoclave and heated at the desired temperature. The hydrochars will be designated as HSMt, being t the treatment temperature. The hydrochar activation was carried out by impregnation with a concentrated KOH solution to yield a KOH/hydrochar mass ratio of 2 or 4, and subsequent carbonization at 800 ºC for 1 h in a N_2 flow. ACs so obtained were treated with 1M HCl and then washed with distilled water till absence of chloride ions in the washing waters. They will be designated as HSMt-x, being x the digit that indicated the KOH/hydrochar mass ratio.

The direct KOH activation of the dried SM stones was carried out following the same procedure. These activated carbons will be designated as SMx

3.2. Characterization

The morphology of samples was examined by environmental scanning electron microscopy (ESEM) FEI, model Quanta 400, equipment. Ash content was determined by heating the sample at 800 ºC in air until constant weight using a Shimadzu thermobalance (model TGA-50H).

N and O contents were determined by elemental analysis using a Thermo Finnigan (1112 series) equipment, and by XPS using an Escalab 200R system (VG Scientific Co.) equipped with MgK_{α} X-ray source ($h\upsilon$ = 1253.6 eV) and hemispherical electron analyzer. Each spectral region of photoelectron interest was scanned several times to obtain good signal-to-noise ratios. The C_{1s} peak at a binding energy (BE) of 284.6 eV was used as internal standard to obtain the number of components, position of peaks, and peak areas.

N_2 and CO_2 adsorption isotherms were measured at -196 and 0 ºC, respectively, using an Autosorb 1 from Quantachrome after outgassing samples overnight at 10^{-6} mbar and 110 ºC. BET equation was applied to the N_2 adsorption isotherm to obtain the surface area, S_{BET}, and the DR equation was applied to both isotherms to obtain the micropore volume, W, and micropore width, L. The total pore volume, $V_{0.95}$, was obtained from the amount of liquid N_2 adsorbed at $p/p_0 = 0.95$.

3.3. Electrochemical measurements

Electrochemical measurements were investigated at room temperature with 1M H_2SO_4 as electrolyte in both 2EC (Teflon-Swagelok-type) and 3EC. Working electrodes were prepared from a well-mixed slurry of the ACs (90 wt. %) with polytetrafluoroethylene (PTFE) emulsion (10 wt. %) as binder. This slurry was pressed at 3 bar on graphite paper disks (2EC) or graphite foil (3EC) and dried overnight in an oven at 120 ºC. The discs had an area of *ca*. 0.50 cm^2 (ϕ 8 mm) and contained the same amount of active material, *ca*. 4 mg, whereas the graphite foil contained *ca*. 20 mg of active material. Electrodes were immersed in the electrolyte for five days before their assembly in the cells. The 2EC was a symmetric device comprising two electrodes separated by a porous fibrous separator impregnated with the electrolyte solution. The 3ECs comprised the above slurry pasted on graphite paper as working electrode, with reference electrode (Ag/AgCl), and counter electrode (Pt wire).

Cyclic voltammetry (CV) and galvanostatic charge-discharge (GCD) were carried out using a Biologic VMP-300 potentiostat. CVs and GCDs were performed in the 0-0.85 V range, at a scan rate of 2.5 mV s^{-1} for CVs and current densities between 0.14 and 5 A g^{-1} for GCDs.

Gravimetric capacitances, C (F/g), were obtained from the discharge curves of the GCDs by equation (1):

$$C = I_d \Delta t / m \Delta V \qquad (1)$$

where I_d is the discharge current, Δt the discharge time, m the total mass of the AC in the electrodes, and ΔV the voltage interval after the ohmic drop. The coulombic efficiency was calculated from the discharge and charge time, t_d and t_c, respectively, by the formula $(t_d/t_c)\times100$.

For performance comparisons, the gravimetric capacitances in 2EC obtained from the above equation were multiplied by four to obtain the expression per single electrode, which is the 3EC equivalent [12]. However, *per convention,* the gravimetric capacitances obtained from equation (1) in 2EC, C_{2EC}, were used to calculate the energy density in the Ragone plot using the equation $E = C_{2EC}(\Delta V_d)^2/2$, where ΔV_d is the operation voltage taken as $\Delta V_d = V_{max} - IR_{drop}$. Power density was calculated from $P = E/\Delta t$ [13,14].

4. RESULTS AND DISCUSSION

Figure 1 shows micrographs of some selected ACs. Samples HSM150-2 and SM2 had a similar morphology with very large pores and conchoidal cavities caused by brittle fracture of the precursor particles during KOH activation. The more activated samples, HSM150-4 and SM4, showed a greater degree of fracture of the precursor particles during activation, disappearing most of the cavities and larger pores.

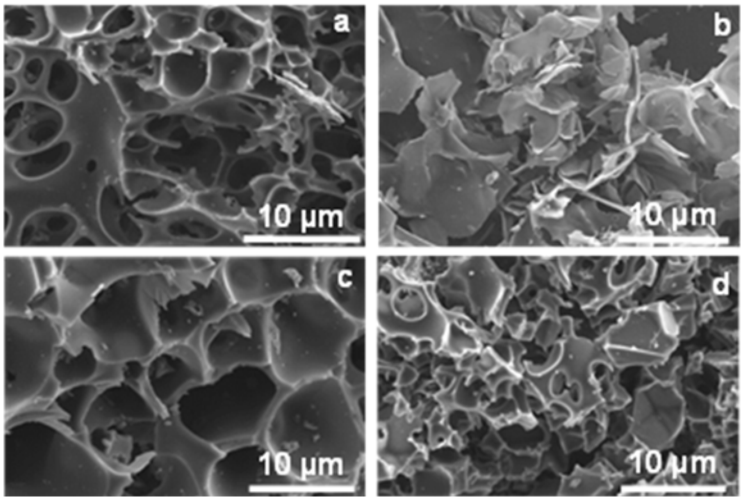

Figure 1. ESEM images of activated carbons: (a) HSM150-2, (b) HSM150-4, (c) SM2 and (d) SM4.

The ash content and elemental analysis of the precursors and ACs together with the N and O contents of ACs from XPS are compiled in Table 1. N and O measured by elemental analysis and XPS can be considered as the total and surface contents, respectively, which give an idea of their distribution in the ACs. The ash content of the SM stones was reduced with the HTC. This reduction was higher when the HTC temperature increased, which was due to the solubilization of the inorganic matter of the precursor. This resulted in ACs from HSM series with lower ash content than those from the SM one. The HTC also affected to the N and O content of the precursor. Thus, the total N content increased whereas the oxygen content decreased with the HTC, being these variations higher when the HTC temperature increased.

Table 1. Ash content (%), elemental analysis (%) in dry-ash-free basis, and nitrogen and oxygen contents (wt.%) from XPS of precursors and activated carbons

Sample	Ash	C	H	N	O*	N_{XPS}	O_{XPS}
SM	6.28	46.95	6.57	0.98	45.50	nd	nd
HSM100	5.90	50.82	6.61	1.23	41.34	nd	nd
HSM150	3.98	57.45	6.12	1.34	35.09	nd	nd
HSM200	2.10	63.92	6.10	1.48	28.50	nd	nd
HSM100-2	5.54	76.85	1.05	0.90	21.20	1.1	12.2
HSM150-2	3.63	71.46	1.06	1.31	26.08	1.3	12.0
HSM200-2	2.00	69.24	1.11	1.40	28.25	1.4	11.7
HSM150-4	3.20	82.56	0.71	0.96	15.77	0.9	6.6
SM2	5.63	77.47	0.56	0.62	21.35	0.7	12.0
SM4	5.30	86.78	0.31	0.77	12.14	0.8	11.8

The increase in the N content was attributable to Maillard-type reactions that occurred during the HTC between the N compounds and the carbohydrates contained in the raw material [10]. Due to this reaction, the N was covalently bonded to the carbon network remaining as a part of the parent carbon upon further temperature treatment during the activation of the hydrochar [10]. This made that the ACs from the HSM series had a higher total N content than those from the SM series. The decrease in the total O content of the hydrochars when the HTC temperature increased was attributed to the increase in the C content of the hydrochars in the same sense.

KOH activation of the hydrochars produced an increase in their C content, which was lower as the HTC temperature increased, and a decrease in their ash and total N and O contents. The increase in the KOH/precursor mass ratio also produced, in both AC series, a decrease of their ash, and total N (except in SM4) and O contents. The N_{XPS} and the total N contents in both AC series were similar. However, the O_{XPS} was in general (except in SM4) lower than the total O content.

The N_{1s} core level spectra of the ACs are depicted in Figure 2 and results from them are compiled in Table 2. All ACs from the HSM series showed three peaks with BE at around 398.4, 400.1, and 401.3 eV. The peak at 398.4 eV can be assigned to pyridines, N-6 functionalities [15]. The second peak at 400.1 eV can be assigned to pyrrolic-N or pyridonic-N, N-5 functionalities [16]. However, the N-5 peak in these ACs were likely due solely to pyridonic-N functionalities because they had sufficient oxygen content (Table 1) to form these functionalities, which would require one N atom per one O atom with a single C-O bond (phenolic functionality). Finally, the third peak at 401.3 eV can be assigned to N within or in a valley position of a graphene layer, i.e., quaternary-N (N-Q functionalities) [16,17]. The most abundant functionalities, from the peak area, were the N-5 (between 47 and 78 %).

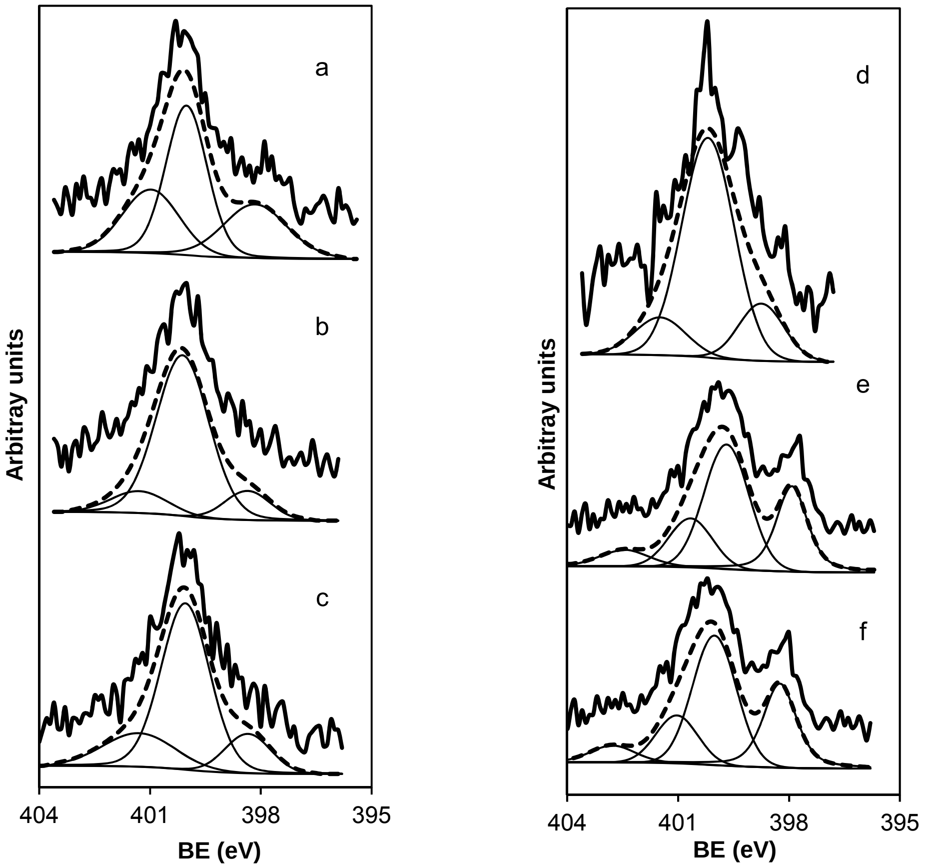

Figure 2. XP spectra of the N_{1s} region of activated carbons: (a) HSM100-2, (b) HSM150-2, (c) HSM200-2, (d) HSM150-4 (e) SM2 and (f) SM4.

Table 2. BE (eV) and area (%) of the N_{1s} and O_{1s} peaks from XPS patterns of activated carbons

Sample	N_{1s} BE (peak area)	O_{1s} BE (peak area)
HSM100-2	398.2(26), 400.0(47), 401.0(26)	531.6(21), 533.0(79)
HSM150-2	398.4(12), 400.1(78), 401.3(11)	531.4(39), 533.0(61)
HSM200-2	398.4(14), 400.0(67), 401.3(19)	531.4(28), 532.9(72)
HSM150-4	398.7(16), 400.2(72), 401.5 12)	531.7(41), 533.1(59)
SM2	398.2(28), 400.1(47), 401.0(18), 402.4(7)	531.6(36), 533.0(64)
SM4	398.2(29), 400.0(48), 401.0(17), 402.8(7)	531.6(36), 533.0(64)

ACs from the SM series showed also the same three peaks and another one at around 402.6 eV that can be assigned to pyridin-N-oxide (N-X functionalities), i.e., pyridinic N bonded to oxygen species [18,19]. These N-X functionalities are formed when pyridine functionalities on the external surface are exposed to atmospheric air [20]. In this case, the most abundant functionalities were also the N-5 (~ 48 %) followed by the N-6 (~ 29 %).

The O_{1s} core level spectrum (not shown) had two components in all samples, the first at BE between 531.0 and 531.6 eV, assigned to double C=O bonds in ketone, quinone, and carboxyl acid groups, and the second at BE between 532.9 and 533.3 eV, assigned to C–O bonds from alcohols, phenols, and ethers [21,22]. These last functionalities were the most abundant in all cases.

N_2 adsorption isotherms of the ACs (Figure 3) were of type I, typical of microporous solids [23], although they contained also some mesopores because the N_2 uptake slightly increased at high relative pressure after micropore filling. This increase was higher in the more activated samples: HSM150-4 and SM4. In addition, the shape of the isotherm in HSM150-4 showed a wide knee as in the case of type I(b) isotherms, indicating a wide micropore size distribution and narrow mesopores (below ~ 3nm). Table 3 exhibits the porosity and surface area of the ACs obtained from the adsorption isotherms. W_{CO_2} was higher than W_{N_2} in all ACs, except in HSM150-4, indicating narrow micropores or constrictions at their entrances that made them less accessible to N_2 molecules at –196 ºC than to CO_2 molecules at 0 ºC [24,25]. When increasing the HTC temperature in the HSM series, and the KOH/precursor mass ratio in both series, the difference between W_{N_2} and W_{CO_2} decreased, and this made the W_{N_2}/W_{CO_2} ratio to increase. This was due to the disappearance of constrictions at the micropore entrances and/or micropore widening. In addition, ACs from HSM series showed higher W_{N_2}/W_{CO_2}ratio than those from the SM series when they are compared at the same KOH/precursor mass ratio.

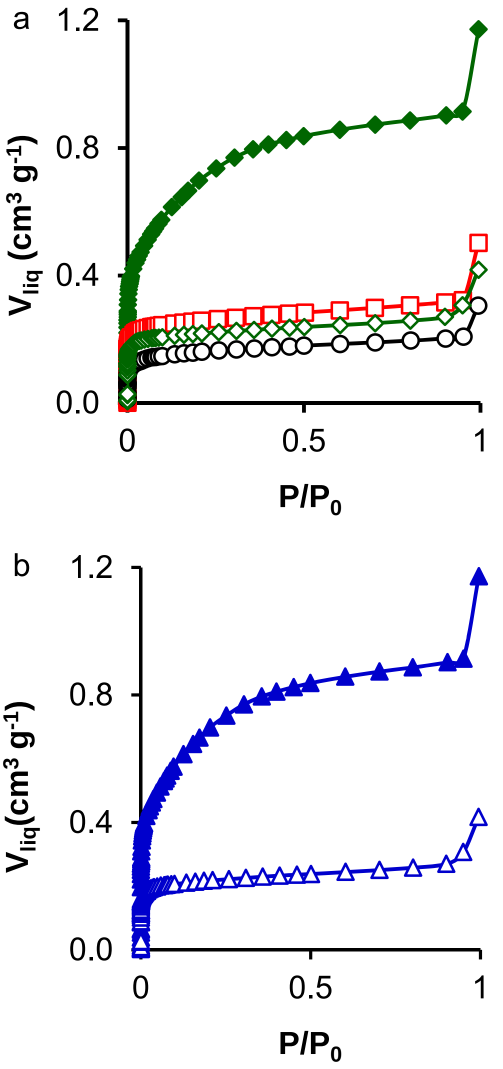

Figure 3. N_2 adsorption isotherms on activated carbons at -196 ºC: a) ○, HSM100-2; ◇, HSM150-2; □, HSM200-2; ◆, HSM150-4. b) △, SM2; ▲, SM4

Table 3. Porosity and surface area of activated carbons

Sample	W_{N_2} cm^3 g^{-1}	W_{CO_2} cm^3 g^{-1}	W_{N_2}/W_{CO_2}	L_{N_2} nm	L_{CO_2} nm	$V_{0.95}$ cm^3 g^{-1}	S_{BET} m^2 g^{-1}
HSM100-2	0.14	0.32	0.44	1.10	0.71	0.22	382
HSM150-2	0.21	0.35	0.60	0.78	0.74	0.31	532
HSM200-2	0.24	0.33	0.73	0.82	0.78	0.35	627
HSM150-4	0.62	0.43	1.44	1.56	0.78	0.91	1464
SM2	0.14	0.32	0.44	1.44	0.70	0.23	378
SM4	0.27	0.37	0.73	1.26	0.79	0.51	661

The $V_{0.95}$ value in all activated carbons, except in those more activated: HSM150-4 and SM4, was lower than the W_{CO_2} value, indicating that even at the high relative pressure of 0.95 not all micropores of these samples were accessible to N_2 molecules at – 196 ºC due to diffusional limitations.

The HSM100, HSM150 and HSM200 hydrochars exhibited a S_{BET} of 23, 26 and 27 m^2 g^{-1}, respectively, and so they needed to be activated to increase their surface area and porosity. ACs from HSM series increased their S_{BET} when the HTC temperature increased, and they showed higher S_{BET} value than those from SM series when they were compared at the same KOH/precursor mass ratio. It is noteworthy the very high surface area of HSM150-4, *ca*. 1500 m^2 g^{-1}, with a mesopore volume of 0.29 cm^3 g^{-1} (from $V_{0.95}$– W_{N_2}) that represented *ca*. 32 % of the total porosity.

Results from porosity and surface area of the ACs indicated that the SM stones were more reactive to the KOH activation after their HTC. This was attributed to: i) the complex chemical reactions of the SM stone carbohydrates during their HTC that led to an incipient carbonization, as shown by the increase in C content of the hydrochars (Table 1); and ii) the lower ash content of HSM hydrochars than SM stones.

CVs at 2.5 mV s^{-1} obtained with 3 and 2EC are depicted in Figure 4. Those obtained with 3EC are very useful for analyzing faradic reactions and voltages at a single surface [26,27]. Thus, they showed quasi-rectangular shape, with clear faradic hump indicating the presence of pseudocapacitance phenomena attributed to the oxygen and nitrogen functionalities [28] that contained all activated carbons used. However, CVs in 2EC showed rectangular shapes without pseudocapacitance effects.

GCDs at 0.5 A g^{-1} (Figure 5) showed a triangular shape with a coulombic efficiency of 100 % in all cases. The gravimetric capacitance increased (Table 4) with higher HTC temperature in the HSM series, and the capacitance decreased with higher KOH/precursor mass ratio in both series. These variations in capacitance can be attributed to changes in surface functionality contents and porosity of the ACs.

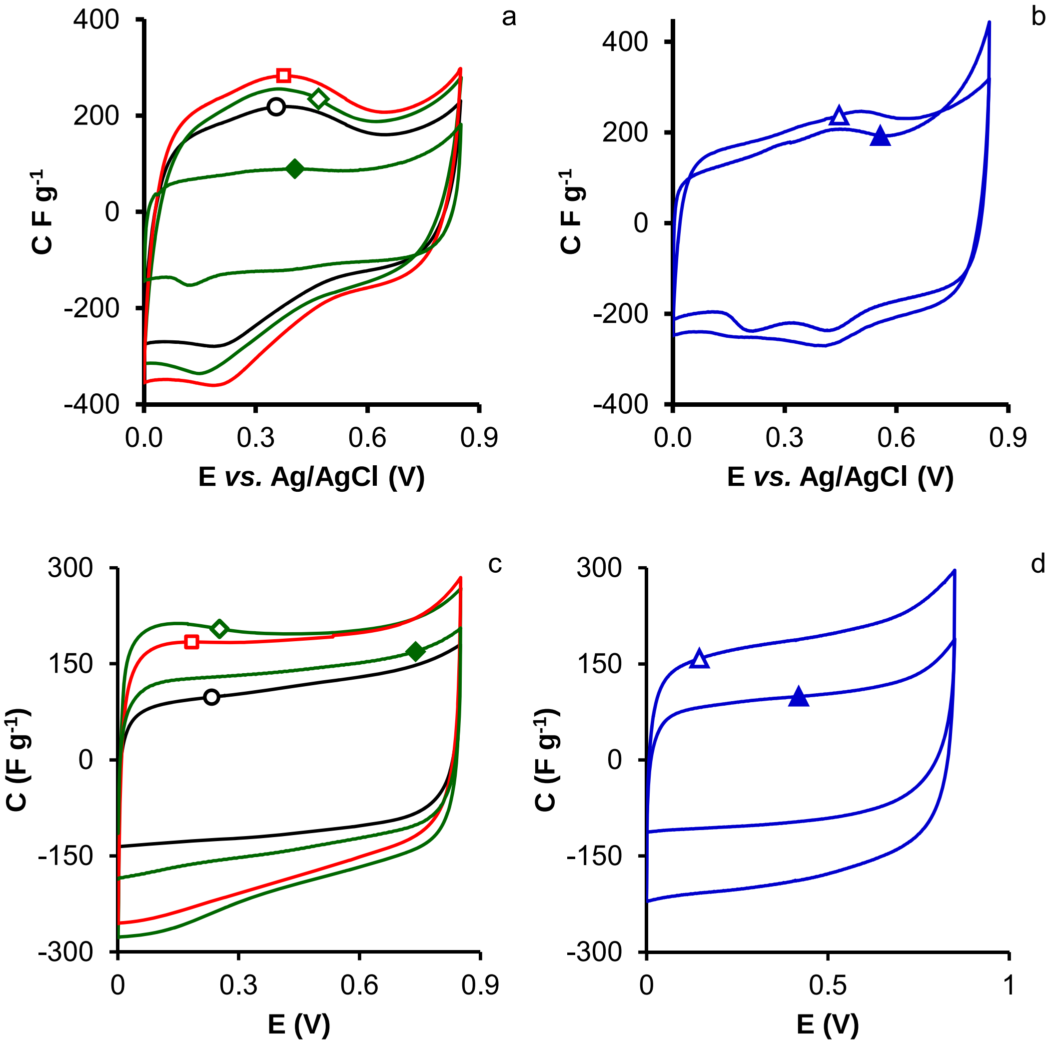

Figure 4. CVs a 2.5 mV s^{-1} in 3EC (a, b) and 2EC (c, d). Samples (a, c): ○, HSM100-2; ◇, HSM150-2; □, HSM200-2; ◆, HSM150-4 and (b, d) △, SM2; ▲, SM4

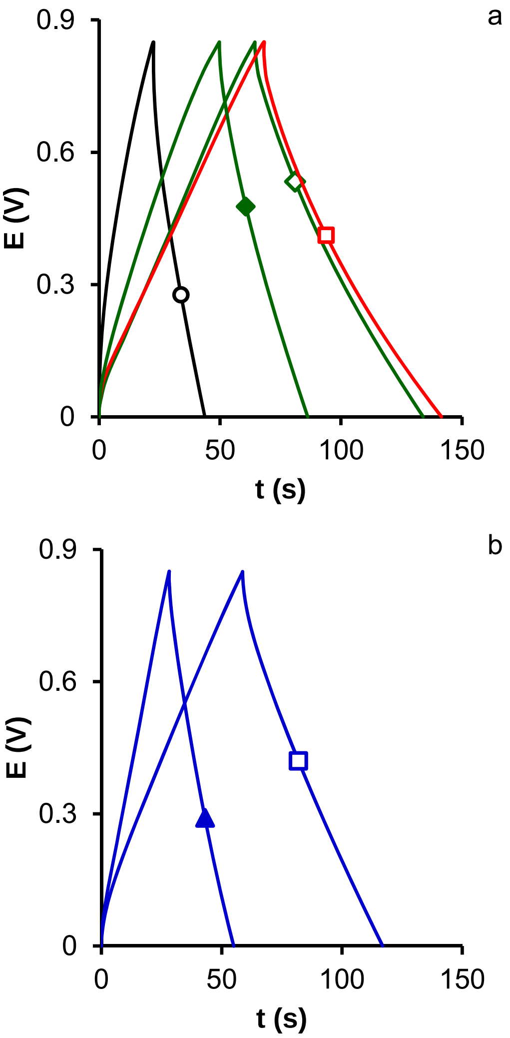

Figure 5. GCDs a 0.5 A g^{-1} en 2EC of samples (a): ○, HSM100-2; ◇, HSM150-2; □, HSM200-2; ◆, HSM150-4 and (b) △, SM2; ▲, SM4

Table 4. Capacitance (F g^{-1}) from GCDs at 0.5 A g^{-1}, and capacitance retention (%) and Coulombic efficiency (%) at 5 A g^{-1}. Energy density (Wh Kg^{-1}) released at 100 W Kg^{-1}, E_{100}, and at 1200 W Kg^{-1}, E_{1200}

Sample	C	Retention	Efficiency	E_{100}	E_{1200}
HSM100-2	171	38	97	4.47	1.37
HSM150-2	227	68	97	6.95	2.12
HSM200-2	235	50	99	11.10	2.54
HSM150-4	125	60	92	3.18	1.26
SM2	183	63	97	4.95	2.52
SM4	90	80	91	1.99	0.55

Thus, in the HSM series the increase in the HTC temperature increased the total N and O contents of the ACs. Most of these functionalities fixed on the micropore walls cannot be detected by XPS, but they would affect to the formation of the double-layer inside the micropores introducing pseudocapacitance effects. This would be possible because the micropores of the HSM samples were accessible to the hydronium ions (0.36-0.42 nm) [29] and to the hydrated bisulfate ions (0.53 nm) [30]. Additionally, the increase in HTC temperature increased the W_{N2}, L_{CO2} and S_{BET} values of the ACs from the HSM series. By the contrary, the increase in the KOH/precursor mass ratio produced a decrease in the capacitance mainly due to the opening of the porosity that made to appear mesopores.

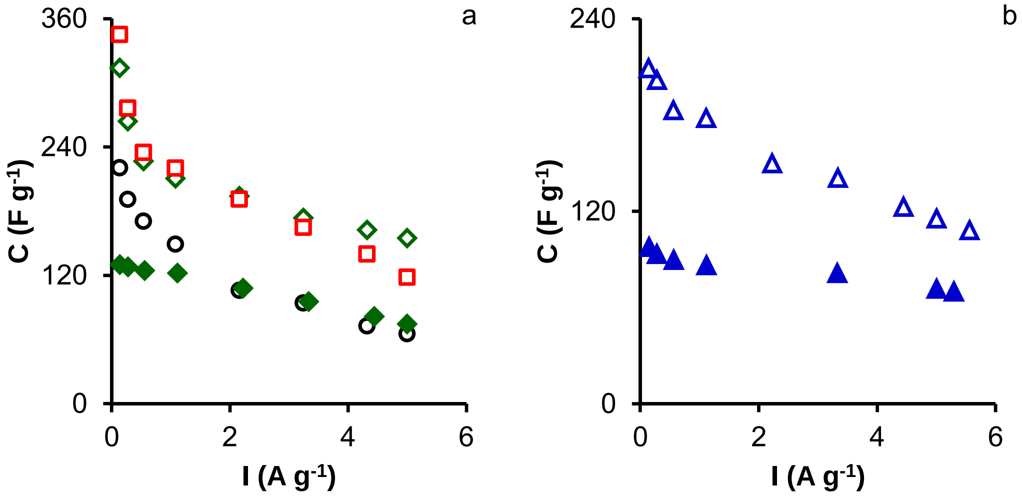

Figure 6. Variation of the gravimetric capacitance with current density of samples (a): ○, HSM100-2; ◇, HSM150-2; □, HSM200-2; ◆, HSM150-4 and (b) △, SM2; ▲, SM4

HSM150-2 and HSM200-2 showed similar C values in the 227-235 F g^{-1}range, which was also similar to that found for ACs from *Melia Azedarach* stones [31] and other lignocellulosic materials reported in the literature [32-37]. Gravimetric capacitance decreased with higher current density (Figure 6) due to cell resistance. The highest capacitance retention at 5 A g^{-1} for samples from HSM series (Table 4) was for HSM150-2, 62 %, and decreased up to 60 % when activation increased (HSM150-4), likely attributed to the large increase in mesoporosity. However, in ACs from SM series the capacitance retention increased with higher activation degree although SM4 showed the lowest capacitance at 0.5 A g^{-1}. Coulombic efficiency at 5 A g^{-1} (Table 4) was lower than that found at 0.5 A g^{-1} and in the HSM series increased with higher HTC temperature and in both series decreased with higher activation degree.

The Ragone plots of the ACs are depicted in Figure 7, revealing the dependence between the energy and power density. The maximum energy density was released at the lowest power density (100 W Kg^{-1}), as shown in Table 4. The maximum energy density increased with higher HTC temperature in the HSM series and decreased with higher activation degree in both series. These results were attributed, as before, to variations in the surface functionality contents and porosity of the ACs.

The energy density decreased at higher power density (Table 4 and Figure 7). HSM200-2 sample showed the highest energy density of all ACs in the power density range studied, but the values of this sample were lower than those found with ACs from *Melia Azedarach* stones [31].

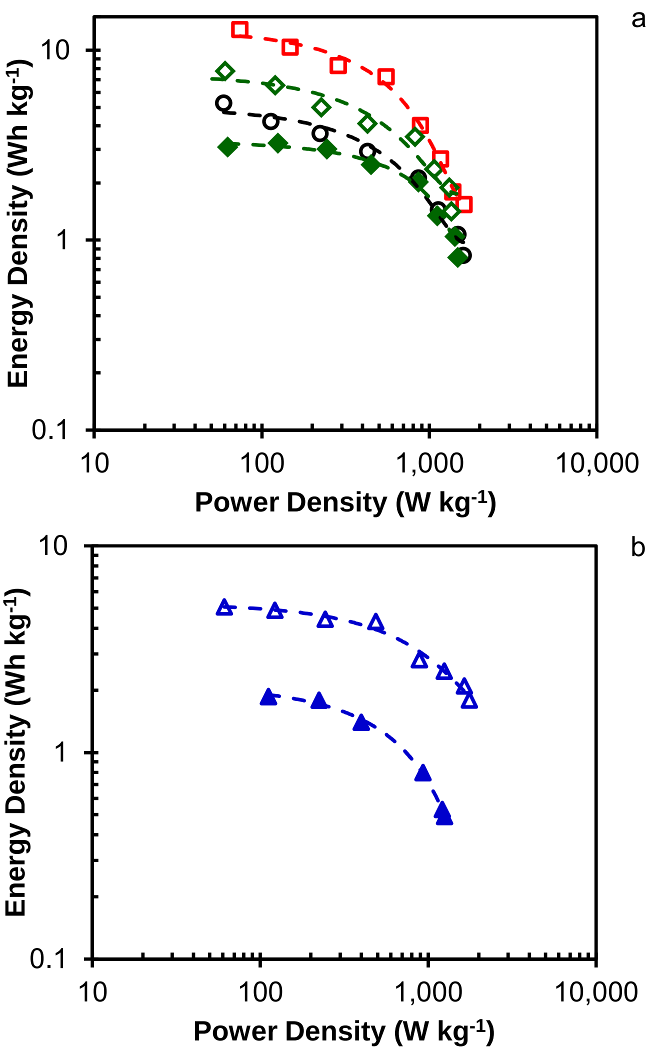

Figure 7. Ragone plots of samples (a): ○, HSM100-2; ◇, HSM150-2; □, HSM200-2; ◆, HSM150-4 and (b) △,SM2; ▲, SM4

5. CONCLUSIONS

Results obtained in this work lead to the following conclusions:

i) ACs from HSM series had lower ash content than those from the SM series due to the solubilization of the inorganic matter of the precursor during HTC.

ii) ACs from HSM series showed higher N content than those from the SM one, attributed to the Maillard-type reactions that occurred during the HTC between the N compounds and the carbohydrates contained in the SM stones.

iii) ACs from both series were microporous and all of them, except HSM150-4, showed narrow micropores or constrictions at their entrances that made them less accessible to N_2 molecules at –196 ºC than to CO_2 molecules at 0 ºC.

iv) It is noteworthy the very high surface area of HSM150-4, *ca*. 1500 m^2 g^{-1}, with a mesopore volume of 0.29 cm^3 g^{-1} (from $V_{0.95}$– W_{N2}) that represented *ca*. 32 % of the total porosity.

v) Results from porosity and surface area of the ACs indicated that the SM stones were more reactive to the KOH activation after their HTC.

vi) The gravimetric capacitance increased with higher HTC temperature in the HSM series, and decreased with higher KOH/precursor mass ratio in both series. These variations can be attributed to changes in surface functionality contents and porosity of the ACs.

vii) HSM150-2 and HSM150-2 showed a gravimetric capacitance in the 227-235 F g^{-1} range at 0.5 A g^{-1}, similar to other ACs from different lignocellulosic materials.

6. REFERENCES

[1] M. Smisek, S. Cerny, Active carbon, manufacture, poroperties and applications, Elsevier (1970).

[2] R.C. Bansal, J.B. Donnet, F. Stoeckli, Active Carbon, Marcel Dekker, New York (1988).

[3] F. Rodríguez-Reinoso, Activated carbon: Structure, characterization, preparation and applications, in: H. Marsh, E.A. Heintz, F. Rodríguez-Reinoso (Eds), Introduction to Carbon Technologies, Ch. 2, University of Alicante, Spain, 1997.

[4] A.M. Abioye, F.N. Ani, Recent development in the production of activated carbon electrodes from agricultural waste biomass for supercapacitors: A review, Renewable and Sustainable Energy Reviews 52 (2015) 1282-1293.

[5] Q. Ma, Y. Yu, M. Sindoro, A.G. Fane, R. Wang, H. Zhang, Carbon-Based Functional Materials Derived from Waste for Water Remediation and Energy Storage, Adv. Mater. 37 (2017) 1605361.

[6] A. Linares-Solano, D. Lozano-Castelló, M.A. Lillo-Ródenas, D. Cazorla-Amorós, Carbon activation by alkali hydroxides: Preparation

and reactions, porosity and performance, in: L.R. Radovic (Ed.), Chemistry and Physics of Carbon, Vol. 30, Ch. 1, CRC Press, New York, 2008, p. 1.

[7] M.M. Titirici, M. Antonietti, Chemistry and materials options of sustainable carbon materials made by hydrothermal carbonization, Chem. Soc. Rev. 39 (2010) 103-116.

[8] L. Wei, M. Sevilla, A.B. Fuertes, R. Mokaya, G. Yushin, Hydrothermal carbonization of abundant renewable natural organic chemicals for high-performance supercapacitor electrodes, Adv. Energy Mater. 1 (2011) 356-361.

[9] C. Falco, J.P. Marco-Lozar, D. Salinas-Torres, E. Morallón, D. Cazorla-Amorós, M.M. Titirici, D. Lozano-Castelló, Tailoring the porosity of chemically activated hydrothermal carbons: Influence of the precursor and hydrothermal carbonization temperature, Carbon 62 (2013) 346-355.

[10] M.M. Titirici, A. Funke, A. Kruse, Hydrothermal carbonization of biomass, in: A. Pandley, T. Bhaskar, M. Stöcker, R.K. Sukumaran (Eds.), Recent Advances in Thermo-Chemical Conversion of Biomass, Ch. 12, Elsevier, Boston, 2015, p. 325-352.

[11] N. Manyala, A. Bello, F. Barzegar, A.A. Khaleed, D.Y. Momodu, J.K. Dangbegnon, Coniferous pine biomass: A novel insight into sustainable carbon materials for supercapacitors electrode, Materials Chemistry and Physics, 182 (2016) 139-147.

[12] T.E. Rufford, D. Hulicova-Jurcakova, E. Fiset, Z. Zhu, G.Q. Lu, Double-layer capacitance of waste coffee ground activated carbons in an organic electrolyte, Electrochem. Commun. 11 (2009) 974-977.

[13] G.A. Ferrero, A.B. Fuertes, M. Sevilla, N-doped microporous carbon microspheres for high volumetric performance supercapacitors, Electrochim. Acta 168 (2015) 320-329.

[14] T. Liang, C. Chen, X. Li, J. Zhang, Popcorn-derived porous carbon for energy storage and CO_2 capture, Langmuir 32 (2016) 8042-8049.

[15] C.D. Wagner, X-Ray Photoelectron Spectroscopy Database. Version 1.0 NIST Standard Reference Database 20. National Institute of Standards and Technology: Gaithersburg, Md, USA, 1989.

[16] J.R. Pels, F. Kapteijn, J.A. Moulijn, Q. Zhu, K.M. Thomas, Evolution of nitrogen functionalities in carbonaceous materials during pyrolysis, Carbon 33(11) (1995) 1641-1653.

[17] M. Pérez-Cadenas, C. Moreno-Castilla, F. Carrasco-Marín, A. F. Pérez-Cadenas, Surface chemistry, porous texture, and morphology of N-doped carbon xerogels, Langmuir 25(1) (2009) 466-470.

[18] D. Wang, M. Chen, C. Wang, J. Bai, J. Zheng, Synthesis of carbon microspheres from urea formaldehyde resin. Mater. Lett. 65(7) (2011) 1069-1072.

[19] M. Wang, J. Fu, J. Zhu, Y. Yan, Q. Xu, Novel N-doped porous carbon microspheres containing oxygen and phosphorus for CO_2 absorbent and metal-free electrocatalysts, RSC Adv. 5(36) (2015) 28080-28084.

[20] K.Y. Kang, B.I. Lee, J.S. Lee, Hydrogen adsorption on nitrogen-doped carbon xerogels, Carbon 47(4) (2009) 1171-1180.

[21] M. Seredych, D. Hulicova-Jurcakova, G.Q. Lu, T.J. Bandosz, Surface functional groups of carbons and the effects of their chemical character, density and accessibility to ions on electrochemical performance, Carbon 46(11) (2008) 1475-1488.

[22] Z.W. He, J. Yang, Q.F. Lü, Q. Lin, Effect of Structure on the Electrochemical Performance of Nitrogen- and Oxygen-Containing Carbon Micro/Nanospheres Prepared from Lignin-Based Composites. ACS Sustainable Chem. Eng. 1(3) (2013) 334-340.

[23] M. Thommes, K. Kaneko, A.V. Neimark, J.P. Olivier, F. Rodríguez-Reinoso, J. Rouquerol, K.S.W. Sing, Physisorption of gases, with special refereence to the evaluation of surface area and pore size distribution (IUPAC technical report), Pure Appl. Chem. 87(9-10) (2015) 1051-1069.

[24] F. Rodríguez-Reinoso, A. Linares-Solano, Microporous structure of activated carbons as revealed by adsorption methods, in: P.A. Thrower (Ed.), Chemistry and Physics of Carbon, Vol. 21, Ch. 1, Marcel Dekker, New York, 1989, p. 1.

[25] D. Cazorla-Amorós, J. Alcañiz-Monge, M.A. De la Casa-Lillo, A. Linares-Solano, CO_2 as an adsorptive to characterize carbon molecular sieves and activated carbons, Langmuir 14 (1998) 4589-4596.

[26] M.D. Stoller, R.S. Ruoff, Best practice methods for determining an electrode material's performance for ultracapacitors, Energy Environ. Sci. 3 (2010) 1294-1301.

[27] E. Raymundo-Piñero, F. Béguin, Application of nanotextured carbons for supercapacitors and hydrogen storage, in: T.J. Bandosz (Ed.), Activated Carbon Surfaces in Environmental Remediation, Elsevier, Oxford, UK, 2006, p 293.

[28] G.A. Ferrero, A.B. Fuertes, M. Sevilla, From soybean residue to advanced supercapacitors, Sci. Rep. 5 (2015) 16618.

[29] D. Hulicova, M. Kodama, H. Hatori, Electrochemical performance of nitrogen-enriched carbons in aqueous and non-aqueous supercapacitors. Chem Mater 18(9) (2006) 2318-26.

[30] C. Moreno-Castilla, M.B. Dawidziuk, F. Carrasco-Marín, E. Morallón, Electrochemical performance of carbon gels with variable surface chemistry and physics. Carbon 50(9) (2012) 3324-3332.

[31] Chapter VI of this thesis.

[32] M-b. Wu, R-c. Li, X-j. He, H-b. Zhang, W-b. Sui, M-h. Tan, Microwave-assisted preparation of peanut shell-based activated carbons and their

use in electrochemical capacitors, New Carbon Mate. 30 (2015) 86-91.

[33] W. Feng, P. He, S. Ding, G. Zhang, M .He, F. Dong, J. Wen, L. Du, M. Liu, Oxygen-doped activated carbons derived from three kinds of biomass: preparation, characterization and performance as electrode materials for supercapacitors, RSC Adv. 6 (2016) 5949-5956.

[34] K. Sun, D. Guo, Nitrogen-doped porous carbon derived from rapeseed residues, Int. J. Electrochem. Sci. 11 (2016) 4743-4754.

[35] Z. Tian, M. Xiang, J. Zhou, L. Hu, J. Cai, Nitrogen and oxygen-doped hierarchical porous carbons from algae biomass: direct carbonization and excellent electrochemical properties, Electrochim. Acta 211 (2016) 225-233.

[36] Y. Huang, L. Peng, Y. Liu, G. Zhao, J.Y. Chen, G. Yu, Biobased nano porous active carbon fibers for high-performance supercapacitors, ACS Appl. Mater. Interfaces 8 (2016) 15205-15215.

[37] Y. Huang, Y. Liu, G. Zhao, J.Y. Chen, Sustainable activated carbon fiber from sawdust by reactivation for high-performance supercapacitors, J. Mater. Sci. 52 (2017) 478-488.

CAPÍTULO VIII

CONCLUSIONES GENERALES

En la presente Tesis Doctoral se sintetizaron materiales de carbón a partir de diferentes precursores como: residuos lignocelulósicos, residuos de la industria oleícola y polímeros orgánicos obtenidos por polimerización de resorcinol, pirocatecol e hidroxipiridina con formaldehído. Estos materiales se prepararon con diferentes geometrías: polvo, monolitos, esferas huecas y sólidas y se analizó su uso como electrodos de supercondensadores.

Los resultados obtenidos en el estudio de las esferas de carbono sintetizadas, mediante reacciones de polimerización de resorcinol, pirocatecol e hidroxipiridina con formaldehído, mostraron que su diámetro, el área superficial y la porosidad dependieron del tipo de precursor fenólico empleado y del método de activación usado. El cambio de resorcinol por pirocatecol como monómero precursor influyó en gran medida en las propiedades de las esferas obtenidas debido a su diferente reactividad en la reacción de polimerización. El empleo de mezclas resorcinol-hidroxipiridina permitió obtener esferas de carbono con funcionalidades de N que modificaron la mojabilidad de las esferas de carbono y su resistencia eléctrica. Tanto la activación química con KOH como la física con ciclos de adsorción-desorción de oxígeno produjeron esferas de carbono activadas con áreas superficiales similares, pero el tratamiento con oxígeno generó microporos más anchos. Para esta última muestra se obtuvo la mayor capacidad de almacenamiento de energía a 1 A g^{-1}, 200 F g^{-1} o 17.3 μF cm^{-2}, lo que se atribuyó a que presentó la microporosidad más ancha (0.80

nm) y un bajo contenido en O_{XPS} (4.4 at.%). La capacidad específica de las esferas dopadas con N fue más elevada que para el resto de las muestras debido a los efectos pseudocapacitivos inducidos por los grupos superficiales nitrogenados.

El estudio de la síntesis de esferas huecas y sólidas a partir de los residuos de la industria oleícola puso de manifiesto que este precursor es útil para la preparación de estos materiales, aunque los resultados obtenidos mostraron una capacidad por unidad de superficie baja. Por lo que deberían activarse adecuadamente las esferas para aumentar su microporosidad.

Los aerogeles monolíticos de carbono son excelentes materiales para el almacenamiento de energía eléctrica. Las capacidades gravimétricas obtenidas incrementaron a medida que el tamaño medio de los microporos y el volumen total de poros aumentó en el rango estudiado (0.61-1.15 nm). La resistencia eléctrica fue mayor en medio básico que en medio ácido e incrementó al aumentar el volumen de macroporos. El aerogel de carbono con el mayor volumen de microporos con tamaño medio de 1.15 nm y un elevado volumen de mesoporos presentó la mayor capacidad gravimétrica a una densidad de corriente de 1 A g^{-1} en H_2SO_4 (152 F g^{-1} y 109 F cm^{-3}) y en KOH (166 F g^{-1} y 120 F cm^{-3}). La retención de capacidad fue de un 75% a 14 A g^{-1} (H_2SO_4) y a 20 A g^{-1} (KOH). El mejor comportamiento se obtuvo en medio ácido con una densidad de energía de

14 Wh kg^{-1} a una densidad de potencia de 50-55 W kg^{-1}. No se produjeron perdidas en la eficiencia de los electrodos después de 2500 ciclos de carga-descarga.

Los huesos de los frutos de *Melia Azedarach* carbonizados y tratados hidrotermalmente son precursores adecuados para la preparación de carbones activados. Estos presentaron muy bajo contenido en cenizas 0.7 %, lo que es de gran interés para la preparación de electrodos de supercondensadores. Los carbones activados obtenidos presentaron diferentes contenidos en funcionalidades de N y O dependiendo del método de preparación. Se pudieron obtener carbones activados con hasta 2000 m^2 g^{-1} y contenidos en cenizas de 0.43-0.59 %. La capacidad gravimétrica varió entre 232-240 F g^{-1} a 1 A g^{-1}. Es importante destacar que los valores de ESR y R_{CT} disminuyeron al disminuir el contenido en cenizas. Este resultado pone de manifiesto la importancia de la materia mineral del precursor para la preparación de carbones activados que vayan a ser usados como electrodos de supercondensadores.

Los huesos de los frutos de *Schinus Molle* poseen un bajo contenido en materia mineral que puede ser reducida mediante tratamientos hidrotermales por la solubilización de ésta durante el tratamiento. Los carbones activados obtenidos por activación de los huesos tratados hidrotermalmente tuvieron un contenido en N mayor que aquellos obtenidos por activación directa del hueso. Esto fue debido a reacciones tipo Maillard que tuvieron lugar entre los compuestos de N y los carbohidratos contenidos en los huesos de Schinus Molle. Todos los carbones activados obtenidos fueron microporosos y a partir de los resultados de porosidad y área superficial se dedujo que los huesos fueron más reactivos a la activación con KOH después de su tratamiento hidrotermal. La capacidad gravimétrica incrementó al aumentar la temperatura del tratamiento hidrotermal, mientras que la capacidad disminuyó al incrementar la relación másica KOH/precursor. Estas variaciones se atribuyeron a cambios en el contenido en funcionalidades superficiales y porosidad de los carbones activados.

En conclusión, los carbones activados obtenidos a partir de los huesos de *Melia Azedarach* y *Schinus Molle*, cuando se usaron como electrodos de supercondensadores, presentaron una capacidad y energía almacenada como los mejores carbones activados que se encuentran en la bibliografía preparados a partir de diferentes residuos lignocelulósicos.